UNIVERSITY OF CALIFORNIA

Santa Barbara

Targeted delivery of siRNA to human cancer and human embryonic stem cells with cell level resolution

A Dissertation submitted in partial satisfaction of the

requirements for the degree Doctor of Philosophy

in Chemistry

by

Xiao Huang

Committee in charge:

Professor Norbert O. Reich, Chair

Professor Cyrus R. Safinya

Professor Craig J. Hawker

Professor Stanley M. Parsons

June 2016

The dissertation of Xiao Huang is approved.

_____

Cyrus R. Safinya

_____

Craig J. Hawker

_____

Stanley M. Parsons

_____

Norbert. O. Reich (Chair)

May 2016

Targeted delivery of siRNA to human cancer and human embryonic stem cells with cell level resolution

by

Xiao Huang

ACKNOWLEDGMENTS

This research project would not have been possible without the support of many people. The author wishes to express his gratitude to his research supervisor, Prof. Norbert Reich, and additional mentors Professor Joseph Zasadzinski and Professor Dennis O. Clegg, who were both thoroughly supportive. I am lucky for the chance to study and research abroad in the US, being in the right place for such a great combination of academic communication and collaboration. Norbert offered invaluable assistance and insights, open-door support and guidance, while providing me the freedom to pursue my interests and collaborate with communities of different discipline. Joseph propelled the nanoengineering science side of things, and Dennis enlightened me with stem cell biology and concepts. Deepest gratitude is also due to the members of the supervisory committee, Prof. Cyrus R. Safinya, Prof. Stanley M. Parsons and Prof. Craig J. Hawker.

I would also like to convey thanks to California Institute of Regenerative Medicine (CIRM), National Institute of Health (NIH) and Chinese Scholarship Council (CSC) for grant funding and living support. Special thanks also to my post doc friends Gary Braun, Alessia Pallaoro and Qirui Hu. As the starting of the doctoral program, I received a lot of helps from Gary and Alessia, from the technical details of nanoparticle synthesis and mammalian cell culture, to research designs and data presentation. During the collaboration with Qirui Hu on the stem cell project, I got many guidance and instructions from him on the biological

concepts and techniques like stem cell culture, immunocytochemistry, RT-PCR, etc. That experience came in handy for nearly every project after. Thanks should also be given to Renwei Chen and Jia Niu for technical consultants and insightful discussions; Yifan Lai and Kevin Cheung as undergraduate research assistants. I also want to acknowledge Mary Raven, Sherry Hikita, Cassidy Hinman for helps on microscope and cell culture facilities.

I am grateful to my close colleague and friend Dean Morales, who experienced both exciting and depressed moments together with me during the past five years. I am also grateful to the members of the Reich lab for questions, answers, knowledge, jokes, outdoor exercises, foods and so much more; those I would like to thank in particular include: Adam Pollak, Clayton Woodcock, Erin Morgan, Brigitte Naughton, Isaac Chavez and many others.

Of course my parents have supported my endeavors throughout. They were the key to instilling my curiosity about the world and growing my courage to difficulties of all aspects. I cannot thank them enough for their patience and support, sacrificing large and small to help me out. Similar gratitude to my older brothers Ye Zhang, and my close friends Haisha Gu, Di Kang and Lu Wang.

VITA OF XIAO HUANG

April 2016

EDUCATION

Bachelor of Science in Biotechnology, National Life Science and Technology Talent Training Base, Department of Life Sciences, Nanjing Agricultural University, China, June 2008

Master of Science in Biochemical Engineering, State Key Laboratory of Bioreactor Engineering, Department of Biological Engineering, East China University of Science and Technology, China, June 2011

Doctor of Philosophy in Chemistry, Department of Chemistry and Biochemistry, University of California Santa Barbara, USA, June 2016 (expected)

PROFESSIONAL EMPLOYMENT

2008-11: Graduate Student Researcher, Prof. Jie Bao's group, State Key Laboratory of Bioreactor Engineering, East China University of Science and Technology, China.

2011-16: Graduate Student Researcher, Norbert Reich's group, Department of Chemistry and Biochemistry, UC Santa Barbara, USA

2015-2016: Teaching Assistant, Department of Chemistry and Biochemistry, UC Santa Barbara, USA

AWARDS

- Honored Students Award (2004-05, 2006-07)
- Scientific and Technological Innovation Award (2007-08)
- National Life Science and Technology Talent Training Base Award (2007-2008)
- Excellent Graduate of Nanjing Agricultural University (2008)
- Research Assistantship in East China University of Science and Technology (2008-11)
- Excellent Master Thesis Award (2011)
- Chinese Scholarship Council Scholarship (2011-15)
- California Institute for Regenerative Medicine (CIRM) Research Training Fellowship (2012-15)

POSTER PRESENTATIONS

- "Lipid production by *Trichosporon cutaneum* using corn stover hydrolysate", World Bioenergy Symposium, Suzhou, China (May 2010)
- "Spatio-temporal control of gene regulation using laser-activated hollow gold nanoshell-siRNA conjugates", CIRM Grantee Meeting, San Francisco, USA (Mar 2013)
- "Modular plasmonic nanocarriers for efficient and targeted delivery of siRNA", RNA Silencing, Seattle, USA (Jan 2014)
- "Efficient light-controlled delivery of siRNA to human embryonic stem cells", Tissue Repair & Regeneration, New London, USA (Jun 2015)

PATENT

"Intracellular Delivery System and Methods"; Joseph Zasadzinski, Norbert O. Reich, Gary B. Braun, Demosthenes P. Morales, Xiao Huang. 2015, U.S. Patent Pub. No.: US 2015/0343090 A1.

PUBLICATIONS

1. "Biological removal of inhibitors leads to the improved lipid production in the lipid fermentation of corn stover hydrolysate by Trichosporon cutaneum"; Xiao Huang, Yumei Wang, Wei Liu, Jie Bao. ***Bioresource Technology,*** 2011, 102 (20): 9705-9709.

2. "Modular plasmonic nanocarriers for efficient and targeted delivery of cancer-therapeutic siRNA"; Xiao Huang, Alessia Pallaoro, Gary B. Braun, Demosthenes P. Morales, Maria O. Ogunyankin, Joseph Zasadzinski, and Norbert O. Reich. ***Nano Letters***, 2014, 14 (4): 2046-2051.

3. "Targeted intracellular delivery of proteins with spatial and temporal control"; Demosthenes P. Morales, Gary B. Braun, Alessia Pallaoro, Renwei Chen, Xiao Huang, Joseph Zasadzinski, and Norbert O. Reich. ***Mol. Pharmaceutics***, 2015, 12 (2): 600-609.

4. "Light-activated RNA interference in human embryonic stem cells"; Xiao Huang, Qirui Hu, Gary B. Braun, Alessia Pallaoro, Demosthenes P. Morales, Joseph A. Zasadzinski, Dennis O. Clegg, Norbert O. Reich. ***Biomaterials***, 2015, 63: 70-79.

5. "Light-patterned cell-resolution RNA interference of 3D-cultured human embryonic stem cells"; Xiao Huang, Qirui Hu, Yifan Lai, Demosthenes P. Morales, Dennis O. Clegg, Norbert O. Reich. *Under review.*

6. "Modular surface functionalization of gold nanocarriers for TAT-mediated delivery of short oligonucleotides"; Xiao Huang, Yifan Lai, Gary B. Braun, Norbert O. Reich. *Submitted.*

7. "*Intracellular delivery of therapeutic peptides with light-mediated spatio-temporal control*"; Demosthenes P. Morales, William Wonderly, Amanda Chron, Xiao Huang, Norbert O. Reich. *Submitted.*

ABSTRACT

Targeted delivery of siRNA to human cancer and human embryonic stem cells with cell level resolution

by

Xiao Huang

RNA interference (RNAi), a process that can silence specific genes, has been recognized for its potential in applications from basic research, cancer therapy to tissue engineering. However, the routine use of RNAi for disease treatment or prevention still calls for novel and efficient methods of delivery with targeting control. We recently developed an approach using hollow gold nanoshells (HGNs) and near-infrared (NIR) light: siRNAs loaded on HGNs via gold-thiol bonds are internalized in cells through targeting peptide-mediated pathways; laser illumination at a wavelength resonant with the nanoparticle plasmon (~800nm) triggers the release of siRNAs from gold surface to cytosol without any cell damage. A cancer-therapeutic siRNA (under phase I/II clinical trial) targeting Polo-like kinase (*plk1*) gene is delivered via this strategy to specifically target human prostate cancer cells. We demonstrated that this method has no off-target toxicity to non-cancerous prostate cells, and requires 10-fold less material than standard transfection methods.

Human embryonic stem cells (hESC) hold immense promise in tissue engineering due to their ability to differentiation into all types of cells, and RNAi

can serve as a powerful tool to attain this. We developed our HGN-based construct for effective cell penetration and optimized the protocol to accommodate delivery into hESCs. The effectiveness and biocompatibility of this light-activated RNAi approach were demonstrated by targeting *GFP* and *Oct4* genes in hESCs, and no adverse effects to differentiation were detected.

The *in vitro* generation of tissues and organs for transplantation therapy and disease models for drug screening demand proficient control over the three-dimensional (3D) patterning of gene regulation. The exquisite activation of siRNA activity by tissue penetrable NIR light irradiation in our technique is well suited for this purpose. We used a two-photon microscope to discriminate targeted cell(s) from neighboring cell(s) by simply focusing NIR light at selected x, y and z position to activate the siRNA. The ability to induce light-mediated gene knockdown persists for at least two days, offering a time window for temporal control.

Furthermore, we developed a universal surface module for the maximized delivery of short functional nucleic acids in versatile mammalian cell lines. A modular biotin-modified thiol-RNA is designed as the scaffold for streptavidin and biotin-TAT attaching, sharing the surface with thiolated functional RNA. We found interesting surface chemistries with direct impact on cellular delivery outcomes. This should provide an important basis for various cell engineering applications.

TABLE OF CONTENTS

I. Introduction

A. RNA interference

RNA interference (RNAi) is a process of sequence specific post-transcriptional gene silencing initiated by double-stranded RNA (dsRNA, ~20-25bp). It was first described in *Caenorhabditis elegans* in 1998 [1], where long dsRNA injected into adult animals silenced the expression of genes with sequence homology to the dsRNA [2, 3]. Subsequently, similar phenomena were described in *Drosophila melanogaster,* plants and undifferentiated mammalian cells [2, 4, 5]. As dsRNA is introduced into the cytoplasm, it is processed by an RNase III enzyme, Dicer, into 21-nucleotide (nt) dsRNAs with 2-nt 3' overhangs, termed small interfering RNA (siRNA) [6, 7]. SiRNAs are assembled into the RNA-induced silencing complex (RISC), which mediates the degradation of complementary mRNAs, silencing certain gene expression [3, 8]. Initially, people believed that nonspecific activation of the antiviral response by dsRNA longer than 30nt would deter the use of RNAi as a therapeutic tool in mammals [4, 9, 10]. However, Tushl and Caplen *et al.* [9, 10] reported the delivery of siRNAs to the cytoplasm of mammalian cells that efficiently mediated gene down-regulation. Importantly, introduction of synthetic RNA duplex with perfect homology to the target gene predominantly results in its degradation, thus siRNA emerged as a new tool for regulating specific gene expression [11]. It is being used to investigate the properties of known or suspected factors that play a role in oncogenesis, to discover

the new modulators of this process and is considered as an option for the therapy of diseases and cancers [11]. As a therapeutic approach, RNAi provides solutions to the major drawbacks of traditional pharmaceutical drugs that all targets, including "non-druggable" targets, can be rapidly identified and optimized [12]. For example, TKM-PLK1 targeting *polo-like kinase 1 (plk1)* gene is used to treat patients (phase I/II) suffering from advanced gastrointestinal neuroendocrine tumors and adrenocortical carcinoma by Tekmira (www.sitestage.co/pipeline/tkm-plk1.php). ALN-VSP02 targeting kinesin spindle protein (KSP) and vascular endothelial growth factor (VEGF) for the treatment of tumors and ALN-PCS02 targeting proprotein convertase subtilisin/kexin type 9 (PCSK9) for hypercholesterolemia therapy, have shown success in clinical trials and are ready to reach the market [13].

Meanwhile, the strategy is equally useful in terms of stem cell differentiation and regenerative medicine. Ever since the discovery of stem cells, scientists have pondered over the same question of the best way to direct stem cells to differentiate into desired cell types. The addition of biochemical cocktails of inductive factors is most commonly implemented and is a safe and convenient approach [14-21]. However, most of these approaches typically require an induction period of at least 2 weeks, hindering research progress and clinical applications [22]. Moreover, the bulk of these cocktails contain ligands or growth factors acting through cell surface receptors to induce cascades of cellular reactions that relies on many proteins to specify a lineage for differentiation [23]. In contrast, RNAi only selectively knocks down a few pivotal genes, providing a much more delicate

control of gene expression [22]. Many examples have shown the siRNA-mediated stem cell differentiation: p53 stable knockdown specifically directed embryonic stem cell differentiation into muscle cells under retinoic acid induction at the expense of a neuronal fate [24]; Stau1 knockdown directed C2C12 myoblast cells into a musculoskeletal lineage [25]; BCL2L2 knockdown directed human mesenchymal stem cells into bone cells [26].

B. Problems and current status of the therapeutic use

Small-molecule pharmaceutical drugs need to adhere to the "Lipinski Rules" including high lipophilicity and a molecular weight less than 500. However, in sharp contrast, siRNAs naturally lack these drug-like properties due to their large size (two turns of a nucleic acid double helix), high molecular weight (over 13 kDa) and nearly 40 anionic charges due to the phosphodiester backbone [12]. siRNAs are extremely hydrophilic and heavily hydrated when their sugar-phosphate backbone are exposed to water. The biggest obstacle to the therapeutic use of siRNA is the need for *in vivo* delivery [27]. When administered intravenously, unmodified RNA can be cleaved by serum endonucleases and cause activation of innate immunity through the Toll-like receptor pathway [12, 13]. Both nuclease susceptibility and immunogenicity can be prevented by modifying the chemical structure of the siRNA strands, for example, replacement of the 2' OH group of ribose with 2'-O-methyl or 2' fluoro groups, incorporation of locked or unlocked nucleic acids and substitution of phosphorothioate linkages in place of phosphodiester bonds [28-31].

Another approach to shield siRNA from degradation and immune recognition is to encapsulate it inside nanoparticles. Delivering siRNAs selectively into diseased cells while sparing normal cells has been challenging. All these obstacles have resulted in limited enthusiasm from pharmaceutical companies for investing in RNAi therapeutics [13].

In the past few years, nanotechnology researchers have developed many novel and efficient nanovehicles for siRNA and miRNA delivery [13]. There is a large growth in the usage of nanomaterials for RNAi delivery from 2009 to 2015, and the global delivery market grows to nearly $24 billion by 2015 at a 5 year compound annual growth rate of 27.9% [13]. In addition, the IC50 value for RNAi delivery using nanodevice systems has been reduced by 99% in only the past 5 years [13]. These include lipidoids [32], stable nucleic acid lipid particles (SNALP), and ionizable cationic liquid 1,2-dilinoleyloxy-3-dimethylaminopropane (DLinDMA) [13]. siRNA delivered with DLinDMA, produced by Alnylam Pharmaceuticals, has *in vivo* activity at siRNA doses as low as 0.01 mg/kg in rodents and 0.1 mg/kg in nonhuman primates [33]. Roche's Tekmira liposomal delivery technology shows unprecedented efficiency in animal challenge models for Ebola. More recently, Alnylam Pharmaceuticals began the development of a sugar molecule, 'GalNAc', as the targeting moiety for siRNA delivery in hepatocytes. Combination products enabling smart delivery of RNAi, together with existing potent chemotherapeutic drugs, may present the next revolution in cancer therapy [13].

C. siRNA delivery methods

Viral vectors have been used as an effective way for systemic delivery of nucleic acids in clinical trials, but they have several limitations including carcinogenesis, immunogenicity, broad tropism and difficulty of vector production [34-37]. Non-viral delivery has the potential to address many of these limitations, particular with respect to safety [38, 39]. However, few of these vectors have so far been developed clinically owing to their low delivery efficiency relative to viral vectors [40]. Owing to the developments in material sciences and nanotechnology, this drawback is about to change [41]. Many different kinds of nanomaterials have been designed and applied to the delivery of RNAi, including polymers, liposomes, hydrogels, gold nanopartilces, iron oxide nanopartilces and mesoporous silica nanoparticles [42]. Tumors are targeted passively, taking advantage of their leaky vasculature and poor lymphatic drainage as enhanced permeability and retention (EPR) effects, whereby the endothelial cells of the blood vessel walls possess large gaps between cells as compared to normal healthy tissue with tight junctions [43]. Cellular uptake of siRNA-loaded nanoparticles most often occurs through endocytosis [44]. Ligands including PEG-folic acid, peptides, antibodies and sugars that bind specifically to receptors on target cells to trigger receptor-mediated endocytosis are incorporated into the delivery system to enhance the cell entry.

The first class of nanoparticles vehicles is liposomes, which consist of a phospholipid bilayer wherein the amphiphilic building blocks align in a way that the hydrophilic heads face the interior and exterior of the supra-molecular

superstructure, while the hydrophobic tails form the interior of the membrane [45]. This dual nature gives a liposome the ability to envelop siRNAs in its interior and other hydrophobic molecules in its membrane. Unilamellar liposomes are approximately 100-200 nm in diameter, and the coating of biocompatible polymers like polyethylene glycol (PEG) on the surface increases the blood circulation half-life [42]. The two types of lipid-based siRNA vectors under clinical evaluation include the stable nucleic acid-lipid particle (SNALP) and the lipid-based nanoparticles (LNPs) [33, 46, 47]. Most SNALP formulations can effectively deliver nucleic acids into hepatocytes, and all of the SNALP-targeted genes in clinical trials are disease-relevant targets in the liver [41]. LNP-based siRNA delivery is assessed in patients with hepatocellular carcinoma: TKM-080301 (Tekmira Pharmaceuticals) [41].

Nanogels are a second class of polymer-based delivery carriers. They consist of hydrophilic cross-linked or self-assembled polymer networks, which have high loading capacities (30% wt.), good stability, and can be triggered to release a payload through physical expansion in response to environmental changes in pH, ionic strength, or temperature. Depending on the constitution of the network, and the degree of cross-linking, nanogels range in size form 20-200 nm. Payloads can be encapsulated in nanogels through different means, such as physical entrapment, covalent conjugation to either the interior or exterior of the nanoparticle, and controlled self-assembly through electrostatic or van der Walls interactions [42]. Cyclodextrin polymer (CDP)-based nanoparticles are the first targeted nanoparticle

siRNA delivery system to enter clinical trials for cancer [48]. The clinical potential was established in a Phase I clinical trial, in which the ribonucleotide reductase M2 mRNA was targeted in patients with solid cancers [49].

Solid and hollow gold nanoparticles are another very promising vehicle for drug delivery. SiRNA molecules are typically tethered to the gold surface through Au-thiol bonds. Controlled fabrication of various sized particles (1-150 nm) with limited size dispersity has been established. Using ligand place-exchange reactions, multifunctional monolayers can be fabricated. The core is non-toxic, biocompatible, and inert [42]. Spherical gold nanoparticles at a size of 10 nm possess an intrinsic surface plasmonic absorption at ~520 nm [50], and by changing the size and shape of the particle like shells or rods, the absorption can be increased to the near-infrared (NIR) region. This shift is advantageous for the purpose of photothermal therapy or light-stimulated targeting, because of the ability of NIR light to penetrate deep through tissues up to 10 cm [51, 52].

A common problem for these non-viral delivery systems is that the cellular internalization via ligand-receptor interactions can be hindered by serum proteins absorbed on the surface of the delivery vehicle [53]. Endocytosed materials are entrapped in membrane-bound endocytic vesicles, which fuse with early endosomes and become increasingly acidic as they mature into late endosomes. For many delivery systems, the precise mechanism of endosomal release is poorly understood [41]. The exact intracellular trafficking pathways that affect delivery are so unclear. A recent report showed that for a leading lipid delivery system, ~70% of the siRNA

taken up by cells underwent endocytic recycling and expcytosis [54]. An improved understanding intracellular trafficking, and a better mechanism of endosomal release may facilitate the efficiency of delivery system [41].

D. NIR light-controlled delivery of siRNA using hollow gold nanoshells

Herein, we present a new platform technology based on highly monodisperse, hollow gold nanoshells (HGN) that can be functionalized with thiol-linked siRNA cargo and cell penetration peptide for efficient cellular uptake [55-57]. HGNs with ~40 nm diameter are synthesized through a galvanic replacement reaction of Ag seed with gold in citrate buffer. Thiolated sense strands of siRNA are assembled onto the citrate-passivated HGN surface using a low pH-induced self-assembly method, wherein negatively charged phosphate backbones are neutralized and the RNA assembly can be maximized. After the hybridization of the anti-sense strand, siRNA duplexes are loaded densely on HGNs, and are well protected from enzymatic attack. Cell penetration peptides including RPARPAR or trans-activating transcriptional activator (TAT) are then coated on top of the siRNA layer, through direct conjugation or streptavidin-mediated assembly for cancer cell targeting or generic wide-spectrum cell type penetration (Figure I-1A).

Figure I-1. Schematic of NIR light-activated siRNA delivery. (A) siRNA cargo attached to the HGN by thiol linkers is rapidly endocytosed (B) into endosomes. (C) Pulsed NIR light causes thiol bond cleavage and cargo release (D) Followed by nanobubble-induced endosome rupture. (E) Cargo is released from the endosome to cytosol.

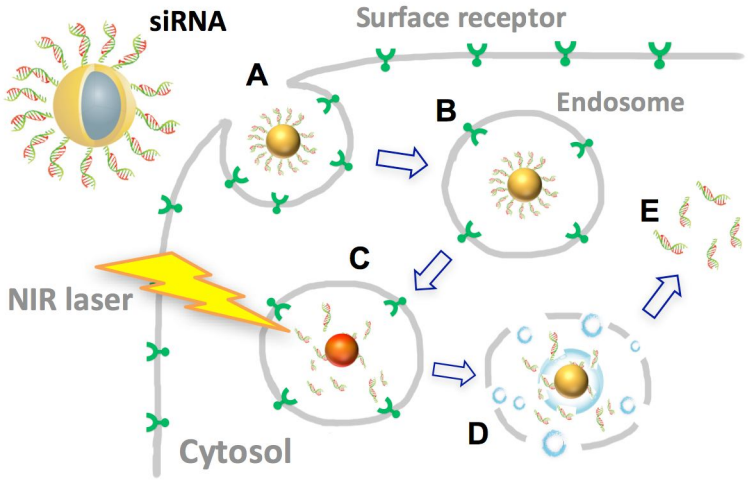

Following endocytosis (Figure I-1B), the plasmon-resonant HGN is activated by picosecond NIR light pulses; the light energy is converted within picoseconds into "hot electrons" that cleave the thiol bonds linking the HGN to the siRNA cargo [58] (Figure I-1C). In the following nanoseconds, the HGN dissipates its heat by vaporizing a minute amount of water surrounding the HGN, forming vapor nanobubbles that insulate both the cell and cargo from significant temperature changes [59-64]. The nanobubbles rapidly expand and collapse, similar to cavitation bubbles in ultrasound, leaving no toxic chemical residue [61, 65] (Figure I-1D). Mechanical forces generated by the bubbles rupture the endosomes providing a unique method of endosome escape and fast, efficient and spatio-

temporally controlled protein or siRNA delivery to the cytoplasm [59, 60] (Figure I-1E), overcoming the ineffective endosomal escape that plagues other nanoparticle methods [39, 66, 67].

E. References

1. Fire, A., et al., *Potent and specific genetic interference by double-stranded RNA in Caenorhabditis elegans.* Nature, 1998. **391**(6669): p. 806-11.
2. Mello, C.C. and D. Conte, Jr., *Revealing the world of RNA interference.* Nature, 2004. **431**(7006): p. 338-42.
3. Marques, J.T. and B.R.G. Williams, *Activation of the mammalian immune system by siRNAs.* Nature Biotechnology, 2005. **23**(11): p. 1399-1405.
4. Yang, S., et al., *Specific double-stranded RNA interference in undifferentiated mouse embryonic stem cells.* Mol Cell Biol, 2001. **21**(22): p. 7807-16.
5. Baulcombe, D., *RNA silencing in plants.* Nature, 2004. **431**(7006): p. 356-63.
6. Meister, G. and T. Tuschl, *Mechanisms of gene silencing by double-stranded RNA.* Nature, 2004. **431**(7006): p. 343-9.
7. Elbashir, S.M., W. Lendeckel, and T. Tuschl, *RNA interference is mediated by 21-and 22-nucleotide RNAs.* Genes & Development, 2001. **15**(2): p. 188-200.
8. Tomari, Y. and P.D. Zamore, *Perspective: machines for RNAi.* Genes & Development, 2005. **19**(5): p. 517-529.
9. Elbashir, S.M., et al., *Duplexes of 21-nucleotide RNAs mediate RNA interference in cultured mammalian cells.* Nature, 2001. **411**(6836): p. 494-498.
10. Caplen, N.J., et al., *Specific inhibition of gene expression by small double-stranded RNAs in invertebrate and vertebrate systems.* Proceedings of the National Academy of Sciences of the United States of America, 2001. **98**(17): p. 9742-9747.
11. Gartel, A.L. and E.S. Kandel, *RNA interference in cancer.* Biomolecular Engineering, 2006. **23**(1): p. 17-34.
12. Bumcrot, D., et al., *RNAi therapeutics: a potential new class of pharmaceutical drugs.* Nature Chemical Biology, 2006. **2**(12): p. 711-719.
13. Conde, J. and N. Artzi, *Are RNAi and miRNA therapeutics truly dead?* Trends in Biotechnology, 2015. **33**(3): p. 141-144.
14. Xu, Z., et al., *The orphan nuclear receptor chicken ovalbumin upstream promoter-transcription factor II is a critical regulator of adipogenesis (vol 105, pg 2421, 2008).* Proceedings of the National Academy of Sciences of the United States of America, 2008. **105**(23): p. 8161-8161.
15. Ling, H.Y., et al., *MicroRNA-375 promotes 3T3-L1 adipocyte differentiation through modulation of extracellular signal-regulated kinase signalling.* Clinical and Experimental Pharmacology and Physiology, 2011. **38**(4): p. 239-246.

16. Kwong, F.N.K., S.M. Richardson, and C.H. Evans, *Chordin knockdown enhances the osteogenic differentiation of human mesenchymal stem cells.* Arthritis Research & Therapy, 2008. **10**(3).
17. Kim, Y.J., et al., *miR-196a Regulates Proliferation and Osteogenic Differentiation in Mesenchymal Stem Cells Derived From Human Adipose Tissue.* Journal of Bone and Mineral Research, 2009. **24**(5): p. 816-825.
18. Tay, Y.M.S., et al., *MicroRNA-134 modulates the differentiation of mouse embryonic stem cells, where it causes post-transcriptional attenuation of Nanog and LRH1.* Stem Cells, 2008. **26**(1): p. 17-29.
19. Brett, J.O., et al., *The MicroRNA Cluster miR-106b similar to 25 Regulates Adult Neural Stem/Progenitor Cell Proliferation and Neuronal Differentiation.* Aging-Us, 2011. **3**(2): p. 108-124.
20. Wegmuller, D., et al., *A cassette system to study embryonic stem cell differentiation by inducible RNA interference.* Stem Cells, 2007. **25**(5): p. 1178-1185.
21. Wilson, K.D., et al., *Dynamic MicroRNA Expression Programs During Cardiac Differentiation of Human Embryonic Stem Cells Role for miR-499.* Circulation-Cardiovascular Genetics, 2010. **3**(5): p. 426-U97.
22. Yau, W.W.Y., et al., *Directing stem cell fate by controlled RNA interference.* Biomaterials, 2012. **33**(9): p. 2608-2628.
23. Hwang, K.C., et al., *Chemicals that modulate stem cell differentiation.* Proceedings of the National Academy of Sciences of the United States of America, 2008. **105**(21): p. 7467-7471.
24. Aranha, M.M., et al., *Apoptosis-associated microRNAs are modulated in mouse, rat and human neural differentiation.* Bmc Genomics, 2010. **11**.
25. Yamaguchi, Y., et al., *Stau1 negatively regulates myogenic differentiation in C2C12 cells.* Genes to Cells, 2008. **13**(6): p. 583-592.
26. Andersen, M.O., et al., *siRNA Nanoparticle Functionalization of Nanostructured Scaffolds Enables Controlled Multilineage Differentiation of Stem Cells.* Molecular Therapy, 2010. **18**(11): p. 2018-2027.
27. Soutschek, J., et al., *Therapeutic silencing of an endogenous gene by systemic administration of modified siRNAs.* Nature, 2004. **432**(7014): p. 173-178.
28. Li, B.J., et al., *Using siRNA in prophylactic and therapeutic regimens against SARS coronavirus in rhesus macaque.* Nature Medicine, 2005. **11**(9): p. 944-951.
29. Choung, S., et al., *Chemical modification of siRNAs to improve serum stability without loss of efficacy.* Biochemical and Biophysical Research Communications, 2006. **342**(3): p. 919-927.
30. Allerson, C.R., et al., *Fully 2 '-modified oligonucleotide duplexes with improved in vitro potency and stability compared to unmodified small interfering RNA.* Journal of Medicinal Chemistry, 2005. **48**(4): p. 901-904.

31. Prakash, T.P., et al., *Positional effect of chemical modifications on short interference RNA activity in mammalian cells.* Journal of Medicinal Chemistry, 2005. **48**(13): p. 4247-4253.
32. Love, K.T., et al., *Lipid-like materials for low-dose, in vivo gene silencing.* Proceedings of the National Academy of Sciences of the United States of America, 2010. **107**(5): p. 1864-1869.
33. Semple, S.C., et al., *Rational design of cationic lipids for siRNA delivery.* Nature Biotechnology, 2010. **28**(2): p. 172-U18.
34. Baum, C., et al., *Mutagenesis and oncogenesis by chromosomal insertion of gene transfer vectors.* Human Gene Therapy, 2006. **17**(3): p. 253-263.
35. Bessis, N., F.J. GarciaCozar, and M.C. Boissier, *Immune responses to gene therapy vectors: influence on vector function and effector mechanisms.* Gene Therapy, 2004. **11**: p. S10-S17.
36. Waehler, R., S.J. Russell, and D.T. Curiel, *Engineering targeted viral vectors for gene therapy.* Nature Reviews Genetics, 2007. **8**(8): p. 573-587.
37. Bouard, D., N. Alazard-Dany, and F.L. Cosset, *Viral vectors: from virology to transgene expression.* British Journal of Pharmacology, 2009. **157**(2): p. 153-165.
38. Pack, D.W., et al., *Design and development of polymers for gene delivery.* Nature Reviews Drug Discovery, 2005. **4**(7): p. 581-593.
39. Mintzer, M.A. and E.E. Simanek, *Nonviral Vectors for Gene Delivery.* Chemical Reviews, 2009. **109**(2): p. 259-302.
40. Putnam, D., *Polymers for gene delivery across length scales.* Nature Materials, 2006. **5**(6): p. 439-451.
41. Yin, H., et al., *Non-viral vectors for gene-based therapy.* Nature Reviews Genetics, 2014. **15**(8): p. 541-555.
42. Li, Z.X., et al., *Mesoporous silica nanoparticles in biomedical applications.* Chemical Society Reviews, 2012. **41**(7): p. 2590-2605.
43. Maeda, H., T. Sawa, and T. Konno, *Mechanism of tumor-targeted delivery of macromolecular drugs, including the EPR effect in solid tumor and clinical overview of the prototype polymeric drug SMANCS.* Journal of Controlled Release, 2001. **74**(1-3): p. 47-61.
44. Yu, B., et al., *Targeted Delivery Systems for Oligonucleotide Therapeutics.* Aaps Journal, 2009. **11**(1): p. 195-203.
45. Zhang, L., et al., *Nanoparticles in medicine: Therapeutic applications and developments.* Clinical Pharmacology & Therapeutics, 2008. **83**(5): p. 761-769.
46. Geisbert, T.W., et al., *Postexposure protection of non-human primates against a lethal Ebola virus challenge with RNA interference: a proof-of-concept study.* Lancet, 2010. **375**(9729): p. 1896-1905.
47. Zimmermann, T.S., et al., *RNAi-mediated gene silencing in non-human primates.* Nature, 2006. **441**(7089): p. 111-114.

48. Davis, M.E., *The First Targeted Delivery of siRNA in Humans via a Self-Assembling, Cyclodextrin Polymer-Based Nanoparticle: From Concept to Clinic.* Molecular Pharmaceutics, 2009. **6**(3): p. 659-668.
49. Davis, M.E., et al., *Evidence of RNAi in humans from systemically administered siRNA via targeted nanoparticles.* Nature, 2010. **464**(7291): p. 1067-U140.
50. Cole, A.J., V.C. Yang, and A.E. David, *Cancer theranostics: the rise of targeted magnetic nanoparticles.* Trends in Biotechnology, 2011. **29**(7): p. 323-332.
51. Weissleder, R., *A clearer vision for in vivo imaging.* Nat Biotechnol, 2001. **19**(4): p. 316-7.
52. Timko, B.P. and D.S. Kohane, *Prospects for near-infrared technology in remotely triggered drug delivery.* Expert Opinion on Drug Delivery, 2014. **11**(11): p. 1681-1685.
53. Salvati, A., et al., *Transferrin-functionalized nanoparticles lose their targeting capabilities when a biomolecule corona adsorbs on the surface.* Nature Nanotechnology, 2013. **8**(2): p. 137-143.
54. Sahay, G., et al., *Efficiency of siRNA delivery by lipid nanoparticles is limited by endocytic recycling.* Nature Biotechnology, 2013. **31**(7): p. 653-U119.
55. Braun, G.B., et al., *Laser-Activated Gene Silencing via Gold Nanoshell-siRNA Conjugates.* ACS Nano, 2009. **3**(7): p. 2007-15.
56. Huang, X., et al., *Modular Plasmonic Nanocarriers for Efficient and Targeted Delivery of Cancer-Therapeutic siRNA.* Nano Lett, 2014. **14**(4): p. 2046-51.
57. Huang, X., et al., *Light-activated RNA interference in human embryonic stem cells.* Biomaterials, 2015. **63**: p. 70-79.
58. Jain, P.K., W. Qian, and M.A. El-Sayed, *Ultrafast cooling of photoexcited electrons in gold nanoparticle-thiolated DNA conjugates involves the dissociation of the gold-thiol bond.* Journal of the American Chemical Society, 2006. **128**(7): p. 2426-2433.
59. Wu, G.H., et al., *Remotely triggered liposome release by near-infrared light absorption via hollow gold nanoshells.* Journal of the American Chemical Society, 2008. **130**(26): p. 8175-+.
60. Wu, G.H., et al., *Synthesis, Characterization, and Optical Response of Gold Nanoshells Used to Trigger Release from Liposomes.* Methods in Enzymology; Liposomes, Pt F, 2009. **464**: p. 279-+.
61. Lukianova-Hleb, E.Y., A.N. Volkov, and D.O. Lapotko, *Laser Pulse Duration Is Critical For the Generation of Plasmonic Nanobubbles.* Langmuir, 2014. **30**(25): p. 7425-7434.
62. Lukianova-Hleb, E.Y., et al., *Plasmonic Nanobubbles Enhance Efficacy and Selectivity of Chemotherapy Against Drug-Resistant Cancer Cells.* Advanced Materials, 2012. **24**(28): p. 3831-3837.

63. Lukianova-Hleb, E.Y., et al., *On-demand intracellular amplification of chemoradiation with cancer-specific plasmonic nanobubbles.* Nature Medicine, 2014. **20**(7): p. 778-784.
64. Lukianova-Hleb, E.Y., et al., *Plasmonic nanobubble theranostics for intra-operative and preventive treatment of head and neck squamous cell carcinoma.* Photonic Therapeutics and Diagnostics X, 2014. **8926**.
65. Lukianova-Hleb, E.Y. and D.O. Lapotko, *Experimental techniques for imaging and measuring transient vapor nanobubbles.* Applied Physics Letters, 2012. **101**(26).
66. Gu, Z., et al., *Tailoring nanocarriers for intracellular protein delivery.* Chemical Society Reviews, 2011. **40**(7): p. 3638-3655.
67. Zuris, J.A., et al., *Cationic lipid-mediated delivery of proteins enables efficient protein-based genome editing in vitro and in vivo.* Nature Biotechnology, 2015. **33**(1): p. 73-80.

II. Efficient and targeted delivery of cancer-therapeutic siRNA

A. Abstract

We have combined a versatile and powerful route to deliver nucleic acids with peptide-based cell-specific targeting. siRNA targeting the polo-like kinase gene is in clinical trials for cancer treatment, and here we deliver this RNA selectively to cancer cells displaying the neuropilin-1 epitope using gold nanoshells. Release of the siRNA from the nanoparticles results from irradiation with a pulsed near-infrared laser, which also provides efficient endosomal escape within the cell. As a result, our approach requires ten-fold less material than standard nucleic acid transduction materials, and is significantly more efficient than other particle based methods. We also describe a particle-nucleic acid design that does not rely on modified RNA, thereby making the preparation of these materials more efficient and much less expensive. These improvements, when combined with control over when and where the siRNA is released, could provide a powerful means of targeted drug delivery.

B. Introduction

Here we delivered therapeutic siRNA specifically to cancer cells through the use of a cancer-cell specific targeting peptide. Peptides provide advantages over other targeting approaches (e.g., antibodies) due to their small size, synthetic versatility, and cell and tissue specificity [1-3]. We employed a peptide following the C-end rule (CendR), RPARPAR (RP) [4], that binds specifically to the

neuropilin-1 (NRP-1) receptor over-expressed by certain types of cancer cells. We targeted the polo-like kinase (PLK1) expressed by the *plk1* gene in prostate cancer cells, critical to centrosome maturation during mitosis, to induce a pro-apoptotic pathway [5]. RNAi-based *plk1* gene down-regulation forms the basis of Phase I/II clinical trials for the treatment of solid tumors [6].

C. Assembly and characterization of the delivery vehicle

Figure II-1. HGN-siRNA-RPARPAR (RP) architecture with original or modular design and schematic of nanoparticle uptake, laser-activated siRNA delivery pathway in PPC-1 cells. A) TEM image of HGNs. B) Schematic of the original HGN-SD-RP architecture and second-generation architecture for modular HGN-LD-RP to achieve versatile siRNA assembly. C) Schematic of nanoparticle uptake and laser-activated siRNA delivery pathway.

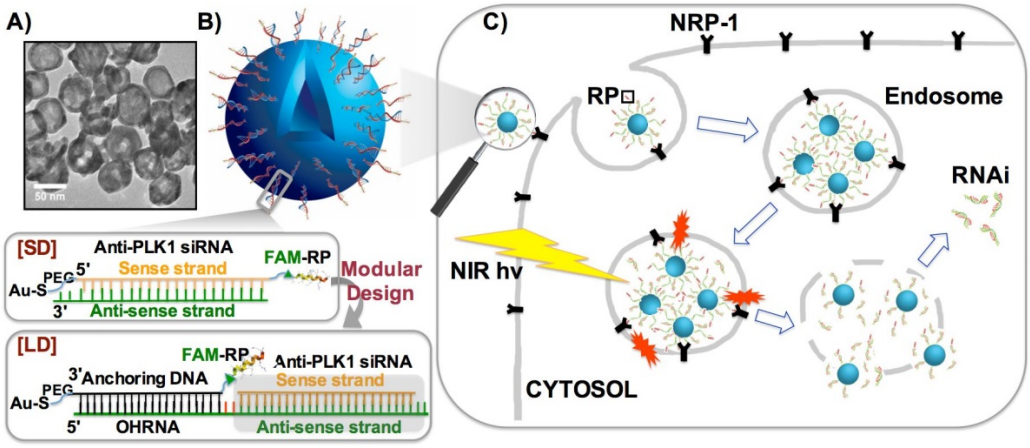

We designed a scheme for attaching peptides to the outside of a thiolated nucleic acid monolayer that can be expanded to include a variety of RNA cargo (Figure II-1A,B). Multiple copies of siRNA against plk1 were conjugated to the

surface of the ~50 nm HGN either directly or supported by a single strand DNA linker through aquasi-covalent (Au-S) bond, simultaneously maximizing drug content, stability, and linkers for multivalent presentation of peptides (Figure II-1B). The siRNA and RP coated HGNs internalize into endosomes through the induction of Neuropiline-1 receptor mediated endocytosis (Figure II-1C). Upon pulsed NIR laser irradiation, the Au-S bond linking the siRNA to the HGN surface is ablated while the conversion of light energy to heat produces a transient vapor bubble that ruptures the endosome, without damaging the siRNA or the cell, releasing the cargo into the cytosol (Figure II-1C). This combination of steps results in highly efficient transfer of siRNA with specificity from the both the targeting peptide and the laser irradiation to ensure RNAi function occurs only in the doubly targeted cells (see below).

To prepare the siRNA functionalized nanoparticles (HGN-SD-RP, Figure II-1B) for gene knockdown, siRNA sense strands containing 5' thiol modifications were assembled onto the citrate passivated HGN surface using a low pH-induced self-assembly method [7]. RNA strands were added to HGNs in low pH (3.0) sodium citrate buffer to neutralize the negatively charged phosphate backbone and maximize the assembly rate. Anti-sense RNA strands were then hybridized to the sense RNA strands to form siRNA duplexes. The residual HGN surface was then passivated with thiol-polyethylene glycol (PEG)-amine (3 kDa) and 6-mercapto-1-hexanol (MCH). The RP peptide, carrying a fluorescein dye (FAM) for tracking and characterization as well as a cysteine for conjugation, was incorporated to the

Figure II-2. HGN-SD-RP synthesis and characterization. A) Schematic of the HGN-SD-RP synthesis steps. B) Size distribution of nanoparticles for the steps during coating. HGN-citrate has a Z-average diameter of 56 nm; HGN-ssRNA 66 nm; hybridized HGN-dsRNA 73 nm; final construct HGN-dsRNA-RP 89 nm. C) Absorption spectrum of HGN broadens and red-shifts along with the increase of particle size at each coating step.

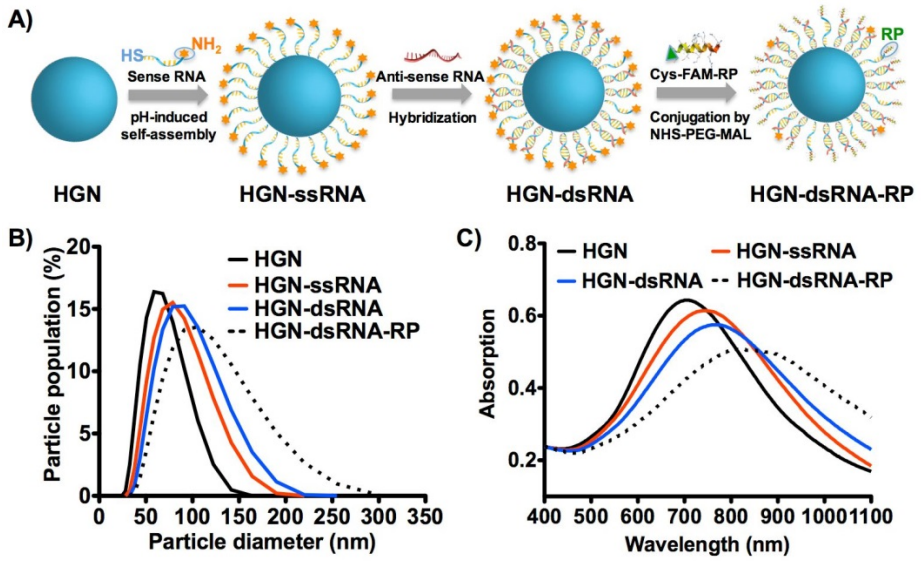

HGN-siRNA via short PEG linkers to bridge the amine on the 3' sense strand and the thiol (cysteine) on the peptide to enable cancer cell-specific targeting (Figure II-2). Initially the citrate HGN showed a resonance at ~710 nm, which red-shifted to ~810 nm as the layers were assembled (Figure II-2C). This assembly method resulted in highly efficient loading of siRNA duplexes (~2300±600 per particle) (Figure II-3).

Figure II-3. Native-PAGE and densitometry analysis of chemically released siRNA (SD) from HGN. A) Native-PAGE gel of siRNA KCN-released from HGN (lanes 1-4, replicates from the same sample), and calibration siRNA concentration gradient (lanes 5-9). B) Calibration curve correlating known siRNA concentration and band intensity from densitometry measurement.

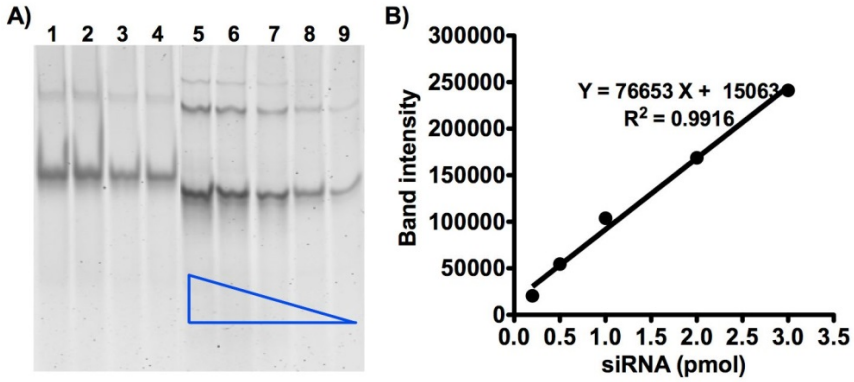

Irradiation of the final product HGN-SD-RP with pulsed laser light (1 KHz repetition rate, ~120 fs pulse length) at 800 nm at a laser power density of 2.4 W/cm^2 for 10 s released ~85% of total siRNA (Figure II-4A, 100% release achieved by HGN dissolution using KCN). The absorbed energy caused the Au-S bonds to be cleaved by hot electrons and the subsequent heating of the Au lattice [8, 9]. Importantly, the siRNA remained hybridized and biochemically active after the laser release (Figure II-4B).

Figure II-4. NIR laser-dependent release of siRNA from HGN. A) Laser release efficiency of HGN-SD-RP with 10 s pulsed laser treatment (1.3, 2.4, 4.0 W/cm^2) compared to KCN chemical release (taken to be 100%). B) Native PAGE analysis of released RNA. Lanes 1 and 2 show dsRNA released with laser treatment at 4.0 W/cm^2 for 10 s. The lack of ssRNA (23 nucleotide length) upon laser treatment suggests the duplex RNA remains hybridized.

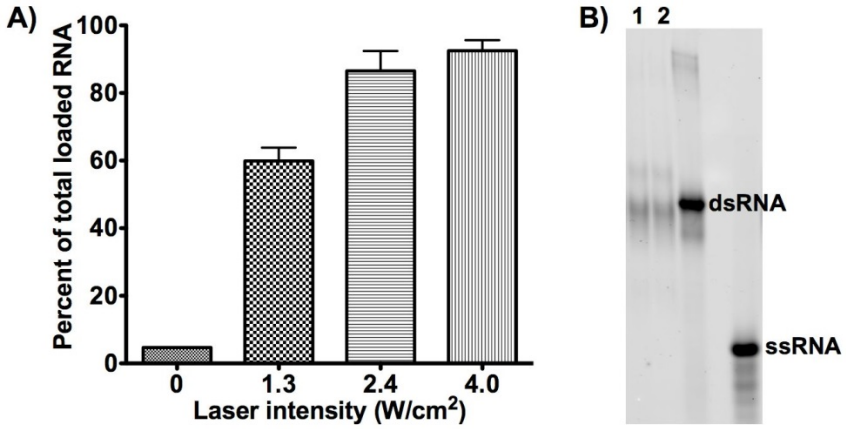

D. Endosomal escape of siRNA

The down-regulation effect of *plk1*-siRNA released from HGNs was tested using the epithelial prostate cancer cell line PPC-1, which overexpresses the NRP-1 receptor targeted by the RP peptide. Western blot and cell viability assays were used to assess and quantify down-regulation of *plk1* (Figure II-5). Irradiation with the femtosecond pulsed NIR laser (2.4 W/cm^2 for 10 s) of cells exposed to HGN-SD-RP led to 70% loss of cell viability at 72 h (Figure II-5A, sample H), similar to the effect of unconjugated siRNA transfected using commercial Lipofectamine RNAiMAX(Lipo). The Lipo treatment required ~13 fold more siRNA (0.37 nM

Figure II-5. Functional *plk1*-siRNA released from HGN-SD-RP by NIR-laser (2.4 W/cm^2 for 10 s) leads to loss of PPC-1 cell viability and down-regulation of PLK1 protein levels. A) NIR-laser treatment of PPC-1 cells having internalized HGN-SD-RP (H) causes a significant decrease of cell viability similar to the effect of lipofectamine (G). A series of controls (defined in the text) are shown in the table underneath the growth curve. ***: $p < 0.001$; ns: not significant. B) Western blot analysis showing knockdown of *plk1* gene expression in PPC-1 cells. Red boxes highlight the down-regulated expression of *plk1* in cells with laser-released siRNA from HGN-SD-RP. The column graph underneath shows the band intensity ratio of PLK1 to β-actin in Western blot image.

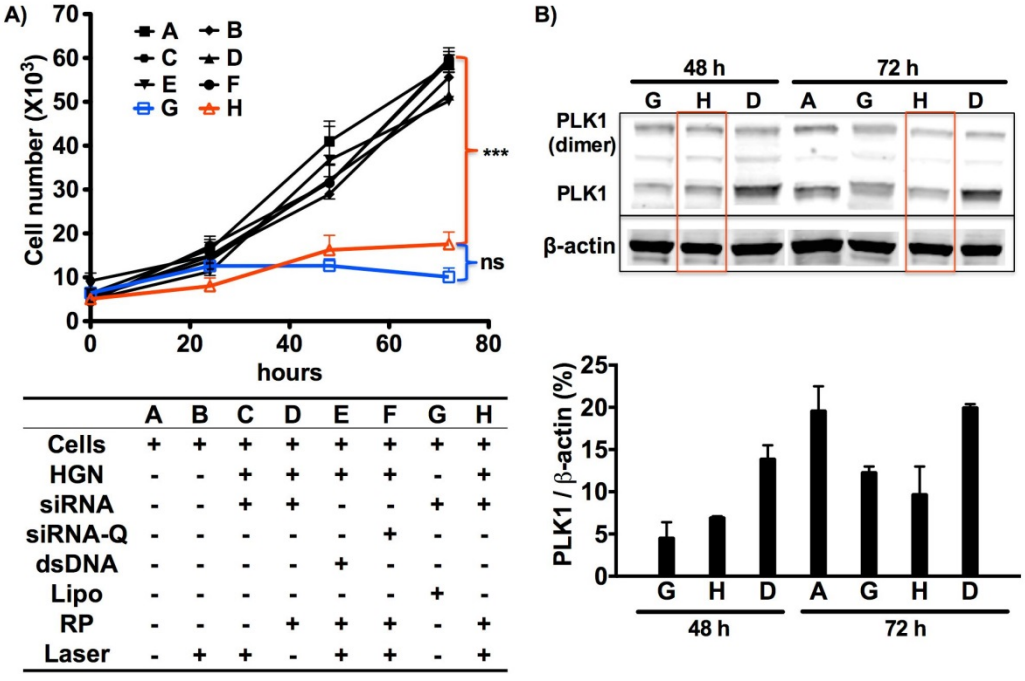

	A	B	C	D	E	F	G	H
Cells	+	+	+	+	+	+	+	+
HGN	-	-	+	+	+	+	-	+
siRNA	-	-	+	+	-	-	+	+
siRNA-Q	-	-	-	-	-	+	-	-
dsDNA	-	-	-	-	+	-	-	-
Lipo	-	-	-	-	-	-	+	-
RP	-	-	-	+	+	+	-	+
Laser	-	+	+	-	+	+	-	+

Figure II-6. Q modification on 5' end of anti-sense strand in PLK1-siRNA blocks the siRNA knockdown activity, as indicated by cell viability. A) Different siRNA structures with or without Q at different sites on the strands. B) Cell viability assay 72 h after Lipofectamine transfection of different siRNA options. Second generation of siRNA architecture shows similar knockdown efficiency as original short duplex structure. Q modification on 5' end of siRNA anti-sense strand blocks the siRNA knockdown activity (C, D and F).

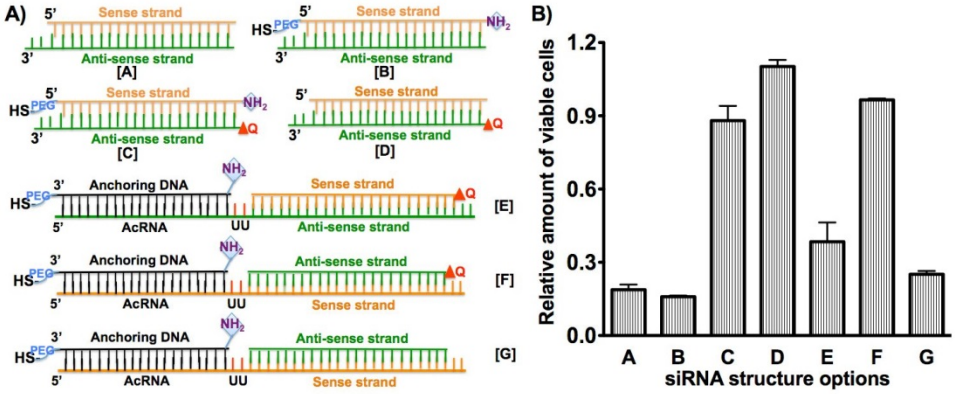

siRNA compared with 5 nM siRNA for 5000 cells) (Figure II-5A, sample G). Like other nanoparticle approaches that also require considerably more siRNA, Lipo lacks an efficient escape mechanism fromendosomes. Cells exposed to the same laser conditions in the absence of HGN-SD-RP showed no loss of viability (Figure II-5A, sample B). HGN-siRNA-Q-RP (where Q indicates Quasar570 dye, placed here on 5' anti-sense RNA, which blocked siRNA activity against *plk1*, Figure II-6) and HGN-dsDNA25bp-RP (loaded non-functional dsDNA in place of the siRNA) were employed as negative controls and were also used to test whether the local heating caused by NIR laser irradiation in the presence of HGNs, induced cellular

Figure II-7. NIR laser power optimization for effective siRNA release from HGN surface with minimum cell damage caused by particle local heating. PPC-1 cells incubated with either HGN-SD-RP or HGN-dsDNA-RP are exposed to different laser power intensity and irradiation duration combinations.

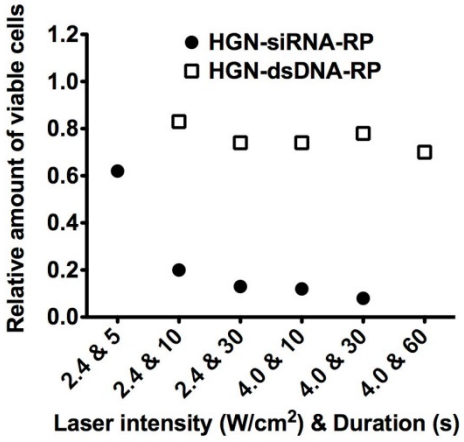

damage (Figure II-5A, samples E-F). The targeting peptide was necessary for the internalization of nanoparticles into PPC-1 cells, as laser treatment of cells exposed to HGN-siRNA without RP did not show any knockdown or cell death (Figure II-5A, sample C). Figure II-5A shows that the HGN-SD-RP was the only construct to cause significant loss of cell viability upon laser exposure. Cells exposed to HGN-SD-RP, but not to the NIR laser showed no effect, demonstrating that laser irradiation was required to activate the biological response in the cells, providing for both spatial and temporal control of knockdown [8]. The minimum laser exposure power and time for effective siRNA release in cells was 2.4 W/cm^2 for 10 s (Figure II-7). Western blot analysis confirmed the down-regulated plk1 expression level in PPC-1 cells treated with HGN-SD-RP and NIR laser after 48 h and 72 h.

Figure II-8. NIR laser-activated release of siRNA from HGN-SD-RP in PPC-1 cells demonstrated by confocal fluorescence microscopy and flow cytometry. A) Fluorescence microscopy (FAM channel) of HGN-SD-RP taken up by PPC-1 cells. B) The same area of the cell monolayer showed in A) after NIR pulsed laser irradiation efficiently releases HGN cargo. C) Difference map of A) and B). Scale bar is 50 µm. D) Fluorescence intensity ratios of B) to A) for pixels in the selected four red regions. E) PPC-1 cells were incubated with HGN-SD-RP then cell fluorescence intensity was assessed by flow cytometry before (red) and after (blue) pulsed NIR-laser treatment compared to fully untreated (no HGN-SD-RP, no laser) PPC-1 (black). Bars indicate the percentage of cells with the fluorescence signal above the brightest 1% of the unlabeled control cells.

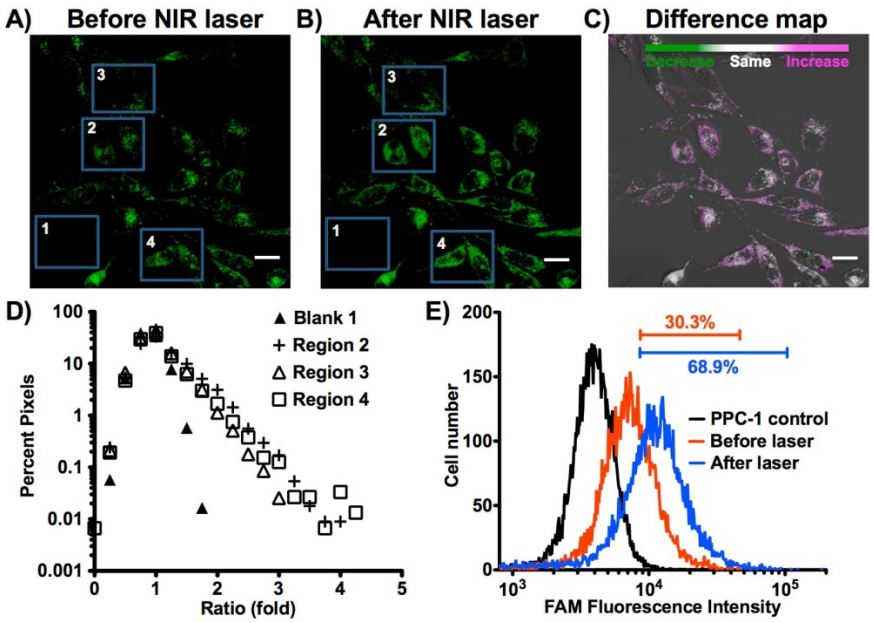

We observed a ~60-70% decrease of the PLK1/β-actin band intensity in Figure II-5B, for lanes G and H, compared to untreated cells (lane A) and to cells carrying HGN-SD-RP, but not irradiated by the laser (lane D). This result likely underestimated the knockdown, as only live cells were used for the Western analysis.

FAM-labeled HGN-SD-RP was readily internalized into PPC-1 cells (Figure II-8A). The siRNA release was assessed using both fluorescence confocal microscopy and flow cytometry. The FAM label on the HGN-SD-RP is ~50% quenched at distances of ~10 nm or less from the gold; when the SD-RP is released by the laser, the fluorescence roughly doubles in intensity [10]. Femtosecond pulsed laser irradiation caused both a significant increase and expansion of FAM fluorescence (from individual puncta to more uniform, diffuse) in the cytosol of each cell, indicative of the release of siRNA-RP in individual cells as shown by confocal microscopy (Figure II-8A-C). Regions of interest were selected, enclosing either single cells (Regions 2, 3, and 4 in Figure II-8A-B) or the glass slide background (Region Blank 1) to conduct pixel intensity analysis (Figure II-8D). 40-60% of the pixels in cells showed greater than 1-fold increase in intensity, whereas almost 100% of the pixels in the Blank 1 region showed no fluorescence increase (Ratio ~1) following laser treatment. Flow cytometry showed an increase in average intensity (Figure II-8E). We noted that ~30% of the PPC-1 cell population after HGN-SD-RP internalization showed a significant fluorescence signal, defined by being above the brightest 1% of the unlabeled control cells. The percentage

increased to ~70% after laser irradiation (Figure II-8E), due to a 2.5-fold increase in mean cell intensity that was consistent with maximal release of the SD-RP from the HGN. This also suggests that at least 70% of the cells efficiently internalized HGN-SD-RP.

Figure II-9. HGN-siRNA-RP dosage titration for effective siRNA knockdown in PPC-1 cells. Various concentrations of HGN-siRNA-RP were incubated with PPC-1 cells, treated with laser, and then plated to 96-well plate to assay cell viability after 72 h.

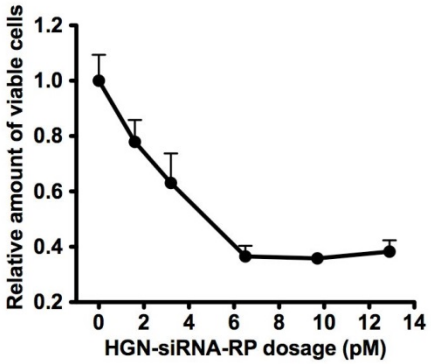

The minimum HGN-SD-RP dosage used for efficient siRNA knockdown and cell death (Figure II-9) was 6.5 pM nanoparticles carrying 15 nM siRNA for 2×10^5 cells (~4000 nanoparticles per cell). The reported concentration represented the amount of HGN-SD-RP available per cell; the amount internalized was likely lower. Even so, the concentration was orders of magnitude less than other nanoparticle approaches that required 10^6-10^7 nanoparticles or more per cell to get effective knockdown of the respective genes [11-13]. Meanwhile, the *plk1*-siRNA dosage needed for maximum cell viability loss by this method was ~10 times less

than other reported *plk1*-siRNA delivery methods [5, 14-18]. Lower particle and siRNA concentrations likely resulted from the combination of efficient particle internalization due to peptide targeting and endocytosis, and efficient siRNA escape from the endosomes via vapor bubble formation and endosome rupture.

E. Prostate cancer cell-specific targeting

Figure II-10. Targeted delivery of HGN-SD-RP. A) HGN-SD-RP are internalized into PPC-1 cells but not in RWPE-1. Upper right inset: bright field; scale bars: 50 µm. B) Flow cytometry assessment of PPC-1 and RWPE-1 cells fluorescence. C) siRNA delivered to RWPE-1 cells by Lipo induces decreased viability, indicating susceptibility to *plk1* knockdown.

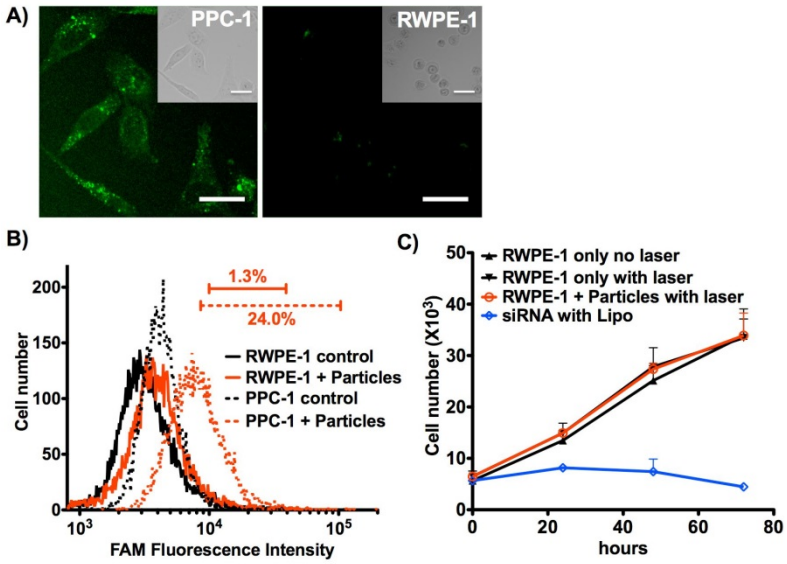

Normal human prostate epithelial RWPE-1 cells lack the NRP-1 receptor on the cell surface, resulting in negligible HGN-SD-RP internalization (Figure II-10A).

By flow cytometry only ~1% RWPE-1 cells were above threshold fluorescence intensity, compared to 30% of PPC-1, which express NRP-1 (Figure II-10B). As expected, there was no down-regulation of plk1 or loss of cell viability on laser treatment of RWPE-1 cells (Figure II-10C). However, RWPE-1 cells were sensitive to *plk1*-siRNA, as shown using the non-selective Lipo transfection of the siRNA construct.

F. Modular RNA assembly

The HGN-SD-RP (Figure II-1B) relies on a thiolated RNA to attach to the SD-RP to the HGN, similar to other nanoparticle-based approaches [8],[11-13]. After validating the release efficiency, the targeting peptide specificity, and the siRNA function in knocking down *plk1* expression, we created a new tethering molecule that could integrate all the above functionalities into a versatile modular architecture with greater flexibility toward delivering a generic siRNA cargo (HGN-LD-RP, Figure II-1B), with the possibility of other peptide targeting sequences. Our goal was to develop a universal HGN-DNA assembly requiring only the addition of non-modified (less expensive and more readily available) RNA. An anchoring thiol-DNA-amine strand was assembled on the HGN and later conjugated to the targeting peptide, as a replacement for the anchoring by thiol-RNA-amine. This core module was hybridized to a siRNA precursor designed with an overhang on its anti-sense strand complimentary to the anchor sequence (OHRNA) (Figure II-1B). We tested a variety of siRNA orientations and dye labels and positions keeping a constant OHRNA sequence (Figure II-6A, structures E-G).

Figure II-11. Comparison of siRNA coating density between SD and LD on HGN. A) Fluorescence intensity of KCN-released SD siRNA was measured and the contribution per HGN calculated. B) Native-PAGE of KCN-released siRNA from HGN. Lane 1: KCN-released SD; lane 2: KCN-released LD.

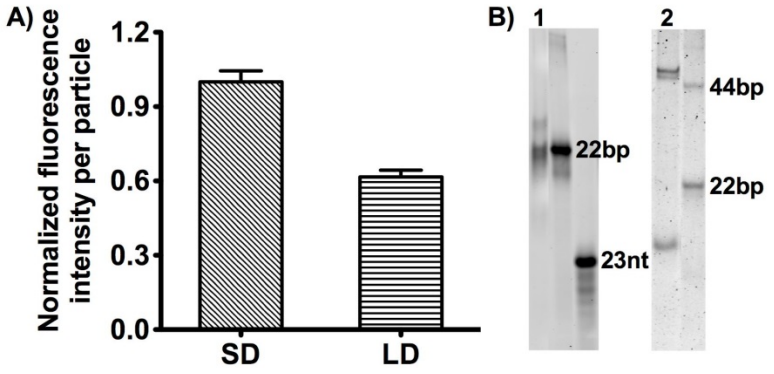

We compared the gene knockdown activity of the various combinations to conventional lipofectamine transfections. The 50 bp DNA-RNA 'long' duplex (LD) was nearly as effective as the short siRNA (Figure II-6B). Fluorescence-based quantification after KCN release of HGN-LD-RP showed that the number of larger LD strands per particle was ~60% of the number of the smaller HGN-SD-RP strands (Figure II-11). The down-regulation activity of the HGN-LD-RP was assessed on PPC-1 cells as with the HGN-SD-RP siRNA system. The down-regulation activity of the HGN-LD-RP was assessed on PPC-1 cells as with the HGN-SD-RP siRNA system. Cell exposure to the laser at 2.4 W/cm2 for 10 s resulted in 46% reduction of cell viability at 72 h, in comparison with 70% from the HGN-SD-RP, and from the same LD construct transfected by Lipo (Figure II-12B). Cell uptake efficiency and cargo release were also evaluated by flow cytometry.

Approximately 19% of the PPC-1 cells incubated with HGN-LD-RP show fluorescence intensity above threshold before laser irradiation. The percentage increased to ~34% after laser treatment (Figure II-12A). This suggests that although the LD construct retains the cell targeting ability, improvements may be necessary to increase the efficiency of cell uptake by modifying the peptide conjugation strategy, optimizing the overhang sequence, or tuning the hybridization conditions to increase the cargo density.

Figure II-12. Cell uptake and knockdown efficiency assessment of the nanocarrier with new modular design (HGN-LD-RP). A) HGN-LD-RP internalization detected by flow cytometry analysis of PPC-1 cells after incubation with HGN-LD-RP and laser treatment. B) PPC-1 cell viability assay 72 h after laser treatment (2.4 W/cm^2 for 10 s) indicates siRNA release and RNAi from modular HGN-LD-RP.

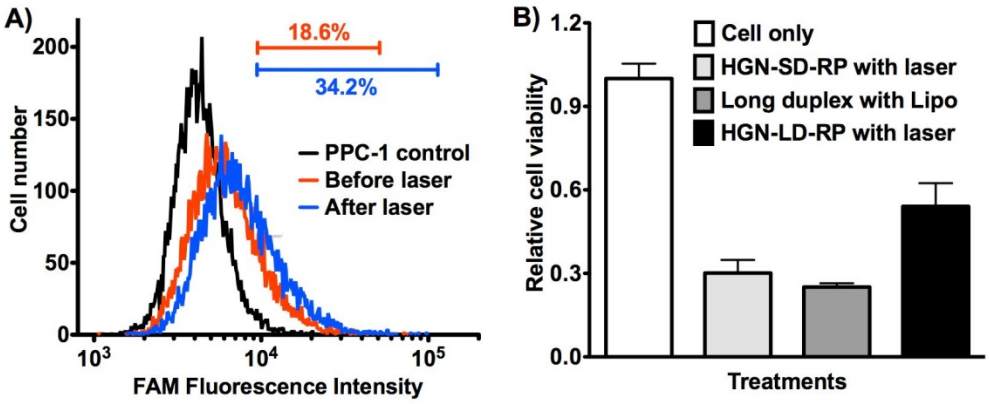

G. Summary

We have successfully developed two modular plasmonic siRNA nanocarriers coupled to hollow gold nanoshells for RNAi-mediated gene knockdown. The construct is engineered to specifically target cancer cells using the RPARPAR ligand against over-expressed NRP-1 receptor on the PPC-1 prostate cancer cell surface to promote cell internalization via endocytosis. The siRNA is released from the HGN and the endosome by femtosecond pulses of near infrared light at 800 nm; the light energy is converted into heat, which thermalizes the thiol bonds holding the siRNA to the HGN, followed by vapor bubble formation that ruptures the endosomes, without damaging the siRNA or the cell. This combination can provide cargo delivery with cellular level resolution at the desired time [8], with ten times less siRNA than techniques with comparable transfection efficiency. Our results show minimum off-target toxicity as evidenced by the lack of cell viability changes with RWPE-1, which does not express NRP-1. Control of laser irradiation provides an additional targeting effect, as PPC-1 cells were also unaffected in the absence of laser treatment. Our approach shows high selectivity and RNAi delivery with high efficiency, versatility and reduced cost. In particular, the modular design we introduce here provides a basis for future applications requiring only the annealing of unmodified siRNA precursor to previously prepared and generic HGN-DNA carriers. The combination of NIR laser-based release and endosomal escape, targeting peptide induced cell-specific internalization, and a versatile siRNA loading strategy substantially improves on our ability to use nanoparticles to

target RNAi to specific cell types and even individual cells and furthers the possibility of using modular constructs for RNAi screening assays and for *in vivo* cancer therapy.

H. Materials and methods

1. Hollow gold nanoshell synthesis

Hollow gold nanoshells were synthesized as described previously. Silver seed particles were prepared by reducing a stirred solution of 500 mL of 0.2 mM $AgNO_3$ with 0.5 mL of 1.0 M $NaBH_4$ in the presence of 0.5 mM sodium citrate in deionized water. The solution was stirred for two hours at 60°C to allow $NaBH_4$ to fully hydrolyze. Larger silver nanoparticles to be used as sacrificial templates for HGN were grown from the silver seed solution by adding 0.75 mL of 2 M NH_2OH HCl and 1.75 mL of 0.1 M $AgNO_3$ and stirring overnight. The galvanic replacement of the silver template particles with gold was optimized to have an absorbance peak at around 800 nm by quickly mixing 3.2 mL of 25 mM $HAuCl_4$ at 60°C. The solution was cooled to room temperature (RT) and kept in dark for at least several days to allow the excess Ag^+ that formed AgCl to settle to the bottom. HGN was then placed in a 3500 MWCO Slide-A-Lyzer (Thermo) in 3500 mL of 500 μM citrate buffer at pH 5.5. 0.1% of diethylpyrocarbonate (DEPC, Sigma) was added to neutralize any RNase activity, and stirring for 2 days at RT allows the DEPC to decompose. TEM imaging was performed using a FEI Tecnai G2 Sphera microscope (200 kV). Size distribution analysis was done by dynamic light

scattering (DLS) with a Malvern Nano ZS with autotitrator instrument. Optical characterization was performed by UV-VIS spectrophotometry with a UV-1700, PharmaSpec instrument. Particle concentration was estimated using the nanoparticle-tracking analysis system Nanosight LM10HS (Nanosight, Amesbury, UK).

2. HGNs concentration determination

Particle concentration was estimated using the nanoparticle-tracking analysis system Nanosight LM10HS (Nanosight, Amesbury, UK), equipped with a sample chamber NanoSight LM14 with a 638 nm laser and a Viton Fluoroelastomer O-ring. The samples are injected in the sample chamber at room temperature with sterile syringes (Kendall Monoject, Mansfield, MA) until the liquid reached the tip of the nozzle. The software used for capturing and analyzing the data is the NTA 2.3 Build 0025. The samples are measured for 60 s with manual camera level adjustments. The Nanosight system shows excellent accuracy by calibrating with monodisperse 50 nm and 60 nm diameter solid gold nanoparticles with known concentrations (Ted Pella Inc, CA). HGN with maximum absorption at 2.0 optical density (1.0 cm path length) was determined by Nanosight to contain 3.9×10^{9} particles per milliliter. A linear correlation is observed when measuring the maximum absorption of HGN with a serial of dilutions, suggesting that HGN follows the Beer-Lambert Law. Particle concentration was estimated to have an extinction coefficient of 3.1×10^{10} M^{-1} cm^{-1} at the NIR plasmon peak maximum absorbance.

3. Thiolated DNA or RNA preparation and assembly on HGNs

Modified sense RNA strand RNA-1, control DNA strand DNA-1 and anchoring DNA strand for modular design DNA-4 (Table II-1) were purchased from Biosearch Technologies. The RNA strand was dissolved in water (RNase-free) to a concentration of 100 μM and aliquoted at 200 μL volume per tube (1.5 mL RNase-free Eppendorf) followed by vacuum evaporation. The dried RNA was treated with 100 μL of 100% ethanol and stored at -80^{o}C. On thawing, RNA disulfide protection was removed by first vacuum-evaporating the ethanol and then adding 200 μL of water and 5 μL Tris(2-carboxyethyl)phosphine HCl at pH 7.0 (TCEP, 0.5 M, #646547-10 X 1mL, Sigma). After 10 min, $CHCl_3$ (800 μL) was mixed to extract and remove the mercaptohexanol, carefully discarding the organic phase, and repeating for a total of four extractions. The aqueous layer was transferred to a new tube and used immediately.

Freshly prepared thiol- sense RNA or DNA strands were assembled onto the HGN using a fast pH-induced self-assembly method. ~0.1 nM HGN were combined with 9 μM freshly reduced thiol-modified DNA or RNA (100 μM in 12.5 mM TCEP pH7.0) and 10 mM sodium citrate-HCl (Na_3Cit-HCl, 500 mM, pH 3.0, RNase free), sonicated, and incubated at RT for 20 minutes. Thereafter the solution was pH-neutralized by adding 130 mM HEPES buffer (1 M, RNase free, pH 7.5, Ambion), then salted to 1 M Na^+ in steps, using 3.0 M NaCl, 0.3 M Na_3Cit pH 7.0 (20X SSC, RNase free, Promega), in ~300 mM Na^+ increase per step, waiting 5 minutes between each step. 1 mM $MgCl_2$ (1 M, RNase free, TEKNOVA) and

0.01% Tween-20 (RNase free, Promega) were added and incubated overnight at RT to increase DNA or RNA density on the HGN. The next day HGN-Anchoring DNA or RNA were washed by centrifuging twice at ~7000×g for 10 min, each time keeping the pellet and redispersing with washing buffer (1 mM $MgCl_2$, 0.01% Tween-20, 300 mM NaCl, 30 mM Na_3Cit pH 7.0).

4. DNA or RNA hybridization on HGNs

Anti-sense strand RNA-2 or RNA-4 (all RNA, Biosearch) (Table II-1), complementary DNA strands for control DNA-2 (all DNA, Biosearch) or complementary RNA strands for modular design RNA-3 and RNA-5 (all RNA, Biosearch) were added at 3 μM to a washed stock of 1 mL HGN-anchoring DNA or RNA (0.1 nM) and incubated at 70˚C for 2 minutes followed by 45˚C for 30 minutes. Excess DNA or RNA was removed with conjugation washing buffer (100 mM HEPES pH 7.5, 1mM $MgCl_2$, 0.01% Tween-20). Thiol-PEG-amine (3 kDa, Rapp Polymere GmbH) in ethanol was added at 100 μM to backfill any large exposed surface sites. After 1 h, excess thiol-PEG-amine was removed by centrifugation at ~7000×g for 10 minutes and pellet was resuspended in conjugation wash buffer. 6-mercapto-1-hexanol (MCH, Sigma) in ethanol was added at 5 μM to further passivate HGN surface sites. After 3 h, HGN-dsDNA or HGN-siRNA were centrifuged (at ~7000×g for 10 minutes) and washed with conjugation wash buffer to remove excess MCH.

5. RPARPAR peptide conjugation

A large excess (~1 mg/mL) of MAL-dPEG$_4$-NHS linker (Quanta Biodesign, CAS# 756525-99-2) for conjugation of the HGN-dsDNA or siRNA and the targeting peptide was added to functionalize the 3' end of anchoring the DNA or RNA. The solution was sonicated briefly and incubated for 15 minutes at RT, followed by centrifugation at ~7000×g for 10 minutes at 4˚C and pellet resuspension with conjugation wash buffer twice to remove excess linker. 20 μM of FAM-Cys-X-RPARPAR-OH peptide (RP) (LifeTein LLC, X is aminohexanoic linker, FAM is fluorescein attached to the N-terminus, C-terminus is free carboxyl) was then added, the solution was briefly sonicated and incubated at RT for 1 h. The dsDNA or siRNA-RP coated HGN were centrifuged twice at ~7000×g, the pellet redispersed in conjugation wash buffer to remove any unreacted peptide, and sterile-filtered through a 0.22 μm syringe filter (Millpore). The solution was then concentrated ~5 fold (10 nM HGN) by centrifugation at ~7000×g for 10 minutes with resuspension of the pellet in conjugation wash buffer. Product was stored at 4˚C before adding to cells.

6. Cell culture

The human prostate cancer cells (PPC-1) were a generous gift from Erkki Ruoslahti (Sanford-Burnham Medical Research Institute, La Jolla, San Diego, CA). They were grown in DMEM/high glucose medium with phenol red (Hyclone), supplemented with 10% FBS (Hyclone). Noncancerous prostate epithelial cells

(RWPE-1) (ATCC) were grown in keratinocyte serum free medium (Invitrogen) supplemented with bovine pituitary extract (0.05 ng/mL) and recombinant EGF (5 ng/mL). Both cell lines were maintained at 37 ^{o}C in 5% CO_2 atmosphere and grown in 6-well or 96-well plates (BD Falcon) for experiments.

7. siRNA transfection using Lipofectamine RNAiMAX

For the typical control transfection experiment with non-HGN conjugated siRNA duplex, cells were plated in 96-well plates at a concentration of 3000 cells per well. The following day the reagents were prepared for transfection according to the manufacturer's protocol, with the following quantities intended per well in a 96-well plate format: 0.1 μL of Lipofectamine RNAiMAX and 0.1 μL of 5 μM siRNA were each diluted in 10 μL of OPTI-MEM reduced serum medium (Invitrogen), then combined and incubated at RT for 15 minutes. The transfection mix was then added to the wells containing the plated cells and complete growth medium. The following day the medium was replaced and cells imaged, scored for viability or allowed to grow up to 48 h or 72 h after transfection.

8. HGN transfection and femtosecond laser irradiation

Cells were plated in 6-well plates (24 hours before experiment) and harvested by incubation with 500 μL of non-enzymatic cell dissociation buffer (CDB, Invitrogen) at 37˚C in 5% CO_2 atmosphere for 10-15 minutes, after one wash in calcium and magnesium free Dulbecco's phosphate buffered saline (D-PBS, Invitrogen). Complete growth medium was added and cells centrifuged at

1000×g to remove the CDB. The cell pellet was diluted in the appropriate amount of medium to obtain a concentration of 1×10^6 cells/mL. 6.5 pM of coated HGN were added to 200 μL of cell suspension and incubated in 1.5 mL Eppendorf tubes at room temperature (RT) for 2h on a rotator. 1.2 mL of cold Hank's balanced saline solution (HBSS, with Ca^{2+} and Mg^{2+}, pH 6.7-7.8, Invitrogen) was added and the tube was centrifuged at 55×g for 8 minutes at 4˚C. The supernatant containing free particles was removed and 45 μL HBSS were added and mixed with the cell pellet. Tubes were irradiated with 2.4 W/cm^2 pulsed NIR laser for 10 s by the output of femtosecond (fs) Ti:sapphire regenerative amplifier (Spectraphysics Spitfire) running with 1 KHz repetition rate. The laser beam with ~4 mm diameter was directed onto the sample by a system of mirrors without any focusing optics. The pulsed duration was monitored by a home-built single-shot optical autocorrelator and was kept at about 130 fs. The spectral range of laser irradiation was ~12 nm centered around 800 nm, and the energy of the optical pulse was controlled by Schott neutral density glass filters. A thermopile power meter (Newport Inc., Irvine, CA) was used to measure the incident optical power. Cells were then either collected for fluorescence intensity measurement by flow cytometry, or plated in 96-well plates for cell viability assay and in 6-well plates for Western blot.

9. Cell fluorescence intensity measurements

Cells with internalized particles in HBSS buffer with or without femtosecond laser treatment were collected and injected into a BD Accuri C6 flow

cytometer with a flow rate of 14 μL/min. The gate was based on the lineage area of forward and side scatter plots, and 10,000 events were collected for each sample. The increase in fluorescence intensity after particle internalization or laser treatment was assessed by the population of the cells having intensity higher than 99% of the control cells.

10. Confocal microscope imaging

Cells were plated on a 8-well chamber glass slide (Lab-Tek II), and incubated with 6.5 pM coated HGN at 37˚C in 5% CO_2 atmosphere for 2 h followed by two washes with HBSS to remove any excess HGN. An Olympus Fluoview 1000 MPE Microscope with a 25x water immersion objective (NA 1.05) was used for live cell imaging. The microscope is equipped with a mode-locked titanium-sapphire femtosecond tunable pulsed laser (MaiTai HP, Newport-Spectra Physics), that was used to irradiate the sample to induce cargo release from the HGN, a 473 nm blue laser diode, used to image the FAM signal from the peptide, and a 559 nm green laser diode and a 633 nm HeNe laser that were not used. Images were collected at 12 bit with 512 X 512 pixels. The MaiTai laser was tuned to 800 nm and used to irradiate the sample area with a scan speed of 125 KHz for up to 35 repetitions. The specimen was imaged in a single-photon confocal mode with the blue laser diode at a scan speed of 80k Hz before and after the exposure to the MaiTai fs laser to compare the cell fluorescence intensity difference caused by the laser treatment.

11. Cell viability assay of prostate cancer cells

The PrestoBlue (Invitrogen) assay was used to determine the effect of transfection on cell proliferation for both laser treatment and controls with Lipofectamine RNAiMAX. For laser experiments, cells, with or without particles and treated or untreated with the laser, were plated in 96-well plates at a density of 5000 cells per well. 100 μL of complete medium were added per well and cells were incubated for 0 h, 24 h, 48 h and 72 h, before determining cell viability. For Lipofectamine control experiments cells were tested for viability 24 h, 48 h, or 72 h after transfection. The PrestoBlue assay was used according to the manufacturer's instructions: 10 μL of reagent were added to cells with 90 μL of fresh complete medium; the plate was incubated at 37˚C, 5% CO_2 atmosphere for 2 h; the fluorescence signal was recorded in a Tecan Infinite 200 Pro reader in bottom-read mode. Excitation and emission wavelengths were set at 560 nm (9 nm bandwidth) and 600 nm (20 nm bandwidth) respectively. 4 replicates for each treatment were averaged and analyzed based on a calibration curve to determine then number of cells in each sample. All treatments were repeated at least 3 times and reported as mean ± standard deviation (SD). One-way ANOVA analysis was performed to determine the statistical significance of changes in cell viability for each treatment; $p<0.001$ was considered statistically significant.

12. Western blot

Cells, with or without particles and treated or untreated with laser, were plated in 6-well plates with 2×10^5 cells per well in 2 mL medium and cultured for

48 h and 72 h. Cells were harvested with trypsin/EDTA (0.25%, Sigma) and about 1×10^6 cells were lysed in 100 μL of RIPA lysis buffer (50 mM Tris, 150 mM NaCl, 1% Triton, 0.5% deoxycholate, and 2 mM EDTA) supplemented with protease inhibitor cocktail (Promega) on ice for 30 minutes. The cell lysate was centrifuged at ~12400×g, at 4˚C for 20 minutes. The supernatant was collected and combined with loading buffer (6X, 300 mM Tris-HCl, 0.01% w/v bromophenol blue, 15% v/v glycerol, 6% w/v SDS and 1% v/v beta-mercaptoethanol) and kept at 95˚C for 10 minutes. 40 μL of this solution and 10 μL of pre-stained molecular weight standard (BioLabs) were loaded and separated by electrophoresis through Precast 10% SDS-PAGE gel (Bio-rad). Proteins were electro-transferred onto a nitrocellulose membrane (Bio-rad). The membrane was blocked with 5% bovine serum albumin (BSA, Sigma) in PBST (PBS, Fisher; 0.1% Tween-20) at RT for 30 minutes, then incubated overnight at 4˚C with primary antibodies diluted in 5% BSA-PBST buffer: mouse anti-PLK1 (monoclonal, 1:500 dilution, EMD) and rabbit anti-β-actin (monoclonal, 1:1000 dilution, Abcam). The membrane was subsequently washed thrice for 15 minutes using PBST and then incubated for 3 h in 5% BSA-PBST with secondary antibodies including Alexa Fluor 488 labeled goat anti-mouse IgG (1:10,000 dilution, Invitrogen) and Alexa Fluor 647 labeled goat anti-rabbit IgG (1:10,000 dilution, Invitrogen), followed by wash thrice for 15 minutes using PBST. Images were acquired using a GE Healthcare Typhoon 9400 scanner system and the bands were analyzed using the scanner control software.

I. Appendix

Table II-1. Oligonucleotides attached on HGNs.

Oligos	5'	Sequence (5'→3')	3'	Use
RNA-1	Thiol-PEG18	GGGCGGCUUUGCCAAGUGCUU	NH_2	Short RNA anchor (sense)
RNA-2	-	AAGCACUUGGCAAAGCCGCCCUU	-	Knockdown control (anti-sense)
RNA-3	-	GGGCGGCUUUGCCAAGUGCUU	-	Knockdown control (sense)
RNA-4	Quasar 570	AAGCACUUGGCAAAGCCGCCCUU	-	Knockdown control/ Quantification/Imaging
RNA-5	-	UGGGACUUCAAGUAGACGUGGUGGCUU AAGCACUUGGCAAAGCCGCCCUU	-	Modular design test
RNA-6	-	UGGGACUUCAAGUAGACGUGGUGGCUU AAGGGCGGCUUUGCCAAGUGUUU	-	Modular design test
RNA-7	Quasar 570	GGGCGGCUUUGCCAAGUGCUU	-	Modular design quantification/knockdown
RNA-8	Quasar 570	GCACUUGGCAAAGCCGCCCUU	-	Modular design quantification/knockdown
DNA-1	Thiol-PEG18	ACCCTGAAGTTCATCTGCACCACCG	NH_2	Short DNA anchor
DNA-2	FAM	CGGTGGTGCAGATGAACTTCAGGGT	-	Knockdown control/ Quantification
DNA-3	Thiol-PEG18	ACCCTGAAGTTCATCTGCACCACCG	Quasar 570	Anchoring quantification
DNA-4	NH_2	GCCACCACGTCTACTTGAACTCCCA	Thiol-PEG18	Modular design anchor

J. References

1. Ruoslahti, E., Peptides as Targeting Elements and Tissue Penetration Devices for Nanoparticles. Advanced materials, 2012. 24(28): p. 3747-3756.
2. Sugahara, K.N., et al., Coadministration of a Tumor-Penetrating Peptide Enhances the Efficacy of Cancer Drugs. Science, 2010. 328(5981): p. 1031-1035.
3. Sugahara, K.N., et al., Tissue-Penetrating Delivery of Compounds and Nanoparticles into Tumors. Cancer Cell, 2009. 16(6): p. 510-520.
4. Teesalu, T., et al., C-end rule peptides mediate neuropilin-1-dependent cell, vascular, and tissue penetration. Proceedings of the National Academy of Sciences of the United States of America, 2009. 106(38): p. 16157-16162.
5. Dassie, J.P., et al., Systemic administration of optimized aptamer-siRNA chimeras promotes regression of PSMA-expressing tumors. Nature biotechnology, 2009. 27(9): p. 839-49.
6. Wang, Z., et al., RNA Interference and Cancer Therapy. Pharmaceutical Research, 2011. 28(12): p. 2983-2995.
7. Zhang, X., M.R. Servos, and J.W. Liu, Instantaneous and Quantitative Functionalization of Gold Nanoparticles with Thiolated DNA Using a pH-Assisted and Surfactant-Free Route. Journal of the American Chemical Society, 2012. 134(17): p. 7266-7269.
8. Braun, G.B., et al., Laser-Activated Gene Silencing via Gold Nanoshell-siRNA Conjugates. Acs Nano, 2009. 3(7): p. 2007-2015.
9. Huang, X.H., et al., Cancer cell imaging and photothermal therapy in the near-infrared region by using gold nanorods. Journal of the American Chemical Society, 2006. 128(6): p. 2115-2120.
10. Acuna, G.P., et al., Distance Dependence of Single-Fluorophore Quenching by Gold Nanoparticles Studied on DNA Origami. Acs Nano, 2012. 6(4): p. 3189-3195.
11. Zheng, D., et al., Topical delivery of siRNA-based spherical nucleic acid nanoparticle conjugates for gene regulation. Proceedings of the National Academy of Sciences of the United States of America, 2012. 109(30): p. 11975-80.
12. Zhang, K., et al., Antibody-Linked Spherical Nucleic Acids for Cellular Targeting. Journal of the American Chemical Society, 2012. 134(40): p. 16488-16491.
13. Lu, W., et al., Tumor site-specific silencing of NF-kappaB p65 by targeted hollow gold nanosphere-mediated photothermal transfection. Cancer Research, 2010. 70(8): p. 3177-88.
14. Yang, X.Z., et al., Single-Step Assembly of Cationic Lipid-Polymer Hybrid Nanoparticles for Systemic Delivery of siRNA. ACS Nano, 2012. 6(6): p. 4955-4965.
15. Zhou, J., et al., Octa-functional PLGA nanoparticles for targeted and efficient siRNA delivery to tumors. Biomaterials, 2012. 33(2): p. 583-591.

16. Gu, W.Y., et al., Polymer Nanocarrier System for Endosome Escape and Timed Release of siRNA with Complete Gene Silencing and Cell Death in Cancer Cells. Biomacromolecules, 2013. 14(10): p. 3386-3389.
17. Yang, X.Z., et al., Systemic delivery of siRNA with cationic lipid assisted PEG-PLA nanoparticles for cancer therapy. Journal of Controlled Release, 2011. 156(2): p. 203-211.
18. Xiang, B., et al., PSA-responsive and PSMA-mediated multifunctional liposomes for targeted therapy of prostate cancer. Biomaterials, 2013. 34(28): p. 6976-6991.

III. Light-activated RNAi in human embryonic stem cells

A. Abstract

We describe a NIR light-activated gene silencing method in undifferentiated human embryonic stem cell (hESC) using HGN as the siRNA carrier. Our modular biotin-streptavidin coupling strategy enables positively charged TAT-peptide to coat oligonucleotides-saturated nanoparticles as a stable colloid formation. TAT-peptide coated nanoparticles with dense siRNA loading show efficient penetration into a wide variety of hESC cell lines. The siRNA is freed from the nanoparticles and delivered to the cytosol by femtosecond pulses of NIR light with potentially exquisite spatial and temporal control. The effectiveness of this approach is shown by targeting *GFP* and *Oct4* genes in undifferentiated hESC (H9). The accelerated expression of differentiation markers for all three germ layers resulting from *Oct4* knockdown confirms that this method has no detectable adverse effects that limit the range of differentiation. This biocompatible and NIR laser-activated patterning method makes possible single cell resolution of siRNA delivery for diverse studies in stem cell biology, tissue engineering and regenerative medicine.

B. Introduction

The capability of human embryonic stem cells (hESC) differentiation into all types of cells in the body holds immense promise in tissue engineering and regenerative medicine [1-3], and is of interest for generating disease models for drug screening. RNA interference (RNAi) has been a powerful tool to dissect

genetic pathways and manipulate cellular phenotypes [4-9]. However, the routine use of RNAi in stem cells requires efficient and biocompatible delivery methods [10-12], and while the commonly used viral-based RNAi methods are efficient [13, 14], these can be time-consuming and pose substantial biosafety problems, such as risk of secondary infection and immunogenic response [15-17]. Commercially available transfection reagents such as Lipofectamine have had some success in hESC transfection [9, 18, 19]. However, lipofectamine use could result in unacceptable levels of cytotoxicity and nonspecific changes in gene expression [11, 19-21].

Alternative chemical transient transfection methods using nanocarriers of cationic lipids, polymers, and functionalized gold nanoparticles have also had variable success with hESC derivatives including embryoid bodies, human mesenchymal stem cells and neural stem cells [8, 10, 11, 22-27], but transfection of undifferentiated hESC remains a challenge for synthetic vectors. Importantly, specific targeting within populations of similar cells is not possible using current methods.

To address these needs, we have developed an efficient, biocompatible and broadly applicable method to introduce siRNA into hESC by near infrared light-controlled endosome rupture. This delivery method provides i) efficient endosome escape, ii) control over the timing of siRNA delivery to the cytosol, iii) individual cell-level resolution, and iv) minimal toxicity. Applications include self-renewal studies of undifferentiated stem cells and tissue engineering – an area with pressing

need for new technologies for efficient and cell-specific RNAi delivery [28, 29]. For example, this light-responsive RNAi release strategy has the ability to load different types of RNAi on the nanocarriers with distinct absorption spectrum [30] and activate specific RNAi in required regions of cells by corresponding light irradiation, which can cause the directed differentiation of stem cells to different cell types in a spatially organized pattern during early embryogenesis such as optic cup formation for ocular development [31, 32], Rathke's pouch formation for pituitary tissue development [33] and tooth-germ structure for tooth growth [34].

To create the light-activated hESC silencing system, siRNA molecules were first densely assembled onto plasmonic hollow gold nanoshells (HGN) via thiol bond formation, then were overcoated with a protective protein layer with handles for attaching cell penetrating peptides [35, 36]. Upon irradiation with biocompatible near infrared (NIR) light (~800 nm), the siRNAs are released from the gold surface and endosomes [37]. In this work, we explored the ability of HIV-derived cell penetrating peptide (CPP) TAT (YGRKKRRQRRR) to facilitate the internalization of the HGNs into hESC. However, direct conjugation of TAT-peptide and siRNA-conjugated HGNs resulted in aggregation, presumably due to colloidal surface charge neutralization and bridging between the cationic TAT and the anionic siRNA [38, 39]. We devised an alternative surface coating strategy by positioning TAT on the siRNA via coupling with the tetravalent protein streptavidin, which sterically prevents the siRNA from electrostatic contacts and thus inhibits particle aggregation. The resulting construct was capable of releasing siRNA payloads upon

NIR laser irradiation and could efficiently internalize into a variety of hESC cell lines.

We optimized the knockdown and viability of hESC through a series of protocol variations including cellular dissociation, NIR laser intensity modulation, and ROCK inhibition. To demonstrate the general feasibility of this approach and light-dependent knockdown control, we silenced *GFP* in engineered H9 cells, and *Oct4* in the original H9 cells. Based on the work described here and our prior work, we anticipate spatio-temporal control with siRNA to provide a powerful new avenue for basic research in stem cells and tissue engineering.

C. Construction and characterization of TAT-peptide coated HGN-siRNA

Efficient delivery of siRNA to hESC is known to be difficult for synthetic vectors [19]. To overcome this limitation, we designed a multi-functional nanoparticle carrier by attaching the generic cell penetrating peptide TAT (biotin-YGRKKRRQRRR) onto hollow gold nanoshells (HGNs) functionalized with multivalent siRNA (Figure III-1A). Multiple copies of functional siRNA molecules were conjugated to the surface of the ~50 nm diameter HGN through a quasi-covalent Au-S bond, whereas uptake of the construct by hESC was mediated by the TAT-peptide coating on the particle surface. Upon pulsed NIR laser irradiation, the HGNs strongly absorb pulsed NIR laser light, which is rapidly (nanosecond) converted to heat, ablating the Au-S bond holding the siRNA on HGN surface and

Figure III-1. Nanoparticle architecture and characterization of siRNA on HGN, and schematic of RNAi-mediated differentiation in hESC. A) Schematic of the HGN-siRNA-TAT architecture, NIR laser-activated siRNA delivery and RNAi-mediated differentiation in hESC. Q: Quasar570. B) Size distribution and absorption spectra of nanoparticles during the coating steps. Upper right of the left panel: TEM image of the final construct. Scale bar: 50 nm.

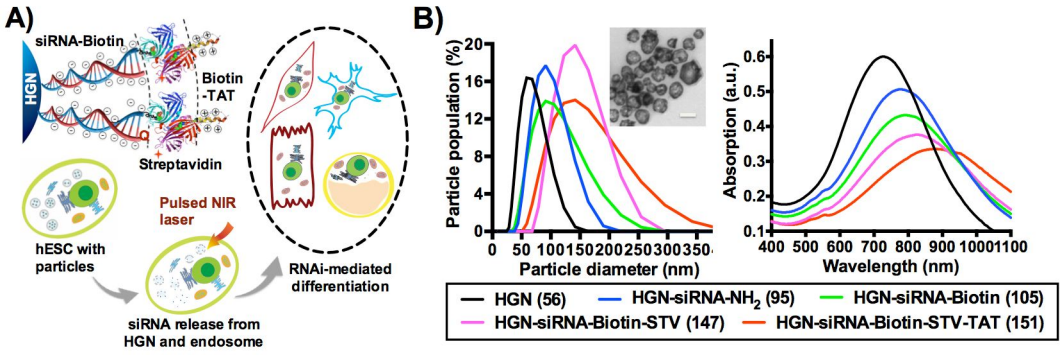

producing transientvapor bubbles that ruptures the endosome without damaging the siRNA [36] or the hESC (Figure III-1A). This strategy results in the successful intracellular transfer of negatively charged siRNA to the cytosol of hESC, thereby initiating RNAi-mediated gene knockdown and stem cell differentiation.

A high number of siRNA duplexes were conjugated to the surface of each HGN through low pH-induced self-assembly of thiolated RNA sense strand followed by the hybridization of the anti-sense strand as described previously [36]. In our prior work (siRNA delivery to a mouse endothelial cell line), we modified TAT peptide with a lipid to form a lipid bilayer around the HGN-siRNA, insulating against nanoparticle-nanoparticle electrostatic coupling [35]. Adopting that strategy here generated TAT-coated HGN in a stable colloidal formulation (with an

Figure III-2. Characterization of HGN-siRNA coated with TAT peptide using different strategies. A) Absorption spectra of TAT peptide-coated HGN-siRNA. Particles form a stable colloidal solution with all three methods of coating: lipid-TAT to form a lipid bilayer blocker (Lipid); siRNA backfilling on thiol-PEG5k-TAT pre-conjugated HGN (PEG); and streptavidin-biotin based insulator (STV). B) Total loading capacity and pulsed NIR laser (2.4 W/cm^2 for 15 s) releasable population of siRNA on HGN for the different coating strategies.

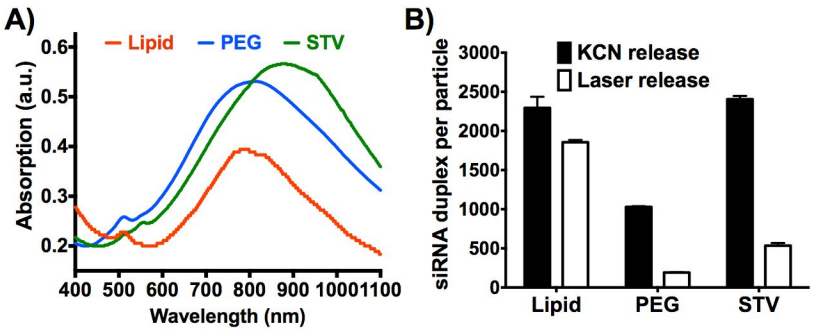

absorption peak at ~800 nm) and efficient siRNA loading (Figure III-2), however, their internalization in hESC was not sufficient to cause effective gene silencing upon laser treatment (Figure III-3). Due to the synthetic constraints this strategy was not amenable to testing peptide sequences or other structural variations. We then pursued an assembly strategy wherein the thiolated siRNA molecules were backfilled onto thiol-PEG5k-TAT coated HGN. The nanoparticles did not aggregate after siRNA backfilling (Figure III-2A), and had strong internalization into hESC (Figure III-3A), but this approach showed inefficient laser knockdown of GFP in

Figure III-3. Comparison of internalization and pulsed laser-induced GFP knockdown in H9-GFP cells between particles from different coating strategies. A) Flow cytometry quantification of particle internalization in H9-GFP cells. Particle internalization is underestimated due to optical limitations of the flow cytometer; however, greater histogram shift indicates that PEG and STV coating strategies have better penetration efficiency than that of the lipid-based strategy. B) Mean fluorescence intensity of cells with nanoparticle (with *GFP*-siRNA and TAT peptide coating) and laser treatment. Cells are assayed by flow cytometry 3 days after laser treatment.

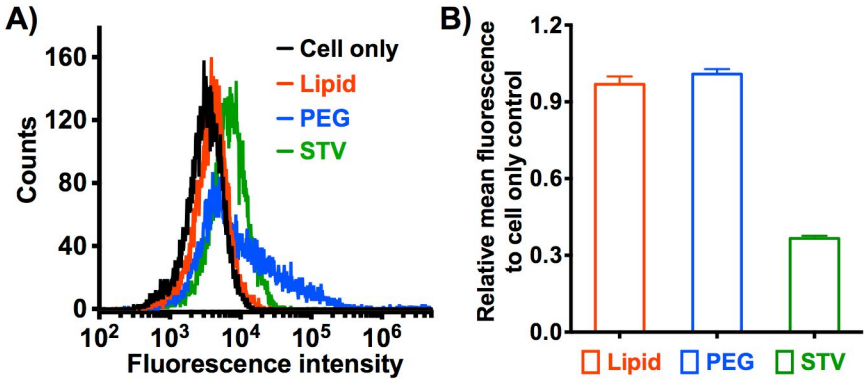

cells, possibly due to the insufficient amount of siRNA release by laser (Figure III-2B, Figure III-3B).

Our optimized design places a ~5 nm streptavidin bridging element between a biotinylated RNA layer and a biotinylated TAT-peptide (Figure III-1A). The average hydrodynamic diameter of the final construct HGN-siRNA-Biotin-STV-TAT (HRT) increased from 56 for bare HGN (citrate stabilized) to 151 nm (Figure III-1B), which can be attributed to the sum of RNA length, protein/peptide coating,

Figure III-4. Release of siRNA from HGN-siRNA-TAT with pulsed laser treatment at different powers (2.4 and 4.0 W/cm^2 for 10, 15 or 20 s) compared to KCN chemical release (100%).

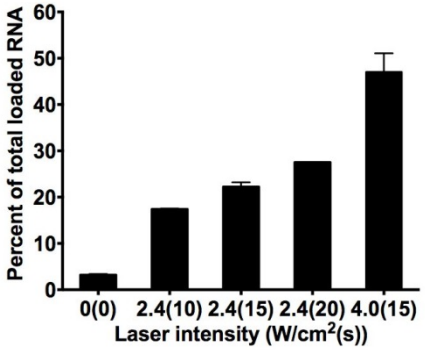

and slight aggregation [40]. The plasmon resonance of the nanoparticles red-shifted from ~710 nm for bare HGN to ~880 nm after the final coating step (Figure III-1B). By tracing the dye label on the siRNA [36], we found that irradiation of HRT by our pulsed NIR laser at 800 nm wavelength caused the release of ~530 siRNA duplexes per particle (~23% of capacity), at a power density of 2.4 W/cm^2 for 15 s (Figure III-4) with 1 kHz pulse repetition rate, ~120 fs pulse duration. This streptavidin-TAT coating strategy was sufficient to cause the desired biological effect. However, future optimization could improve the HGN monodispersity that dictates the sharpness of the absorption resonance peak, and more closely match nanoparticle absorption to the wavelength of the exciting laser.

D. Protocol optimization and GFP knockdown in transduced hESC

The compact clusters of hESC reduce accessibility to transfection; thus, protocols often rely on enzymatic digestion to generate single cells that leads to significant loss of cell viability [19]. We instead used a non-enzymatic method for

Figure III-5. H9-GFP cells dissociated by PBS treatment show better uptake efficiency of nanoparticles than those dissociated using commercial CDB treatment. The fluorescence intensity of cells incubated with nanoparticles is assayed by flow cytometry as an evaluation of particle internalization.

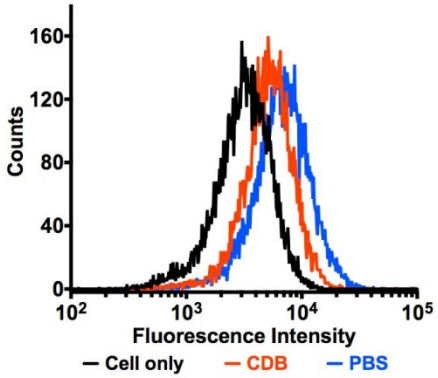

the dissociation of the hESC that generated single cells and small cell aggregates (5-10 cells) while ensuring minimum cell damage, and membrane accessibility to nanoparticles. Notably, we found that a 10 minutes incubation of attached hESC with Ca^{2+} and Mg^{2+} free PBS (37 ˚C) followed by manual dissection was sufficient for cell dissociation. Cells generated by this mild treatment appeared to take up more nanoparticles than cells obtained using commercial non-enzymatic cell dissociation buffer treatment (CDB, Invitrogen) (Figure III-5). Crucially, addition of ROCK inhibitor within the first 24 hours after single cell seeding significantly increased the cell viability (Figure III-6). The optimized HGN transfection protocol (Figure III-7) that we developed here enables both efficient cellular uptake and robust cell viability.

Figure III-6. Addition of ROCK inhibitor after single H9 cell seeding significantly enhances the stem cell viability. A) ROCK inhibitor treatment after seeding for 24 h significantly preserves cell number. Under phase contrast light microscopy, cells are observed to elongate with the ROCK inhibitor addition and shorten back when removed. B) Crystal violet staining of colonies after 6 days affirms the robustness of ROCK inhibitor treatment.

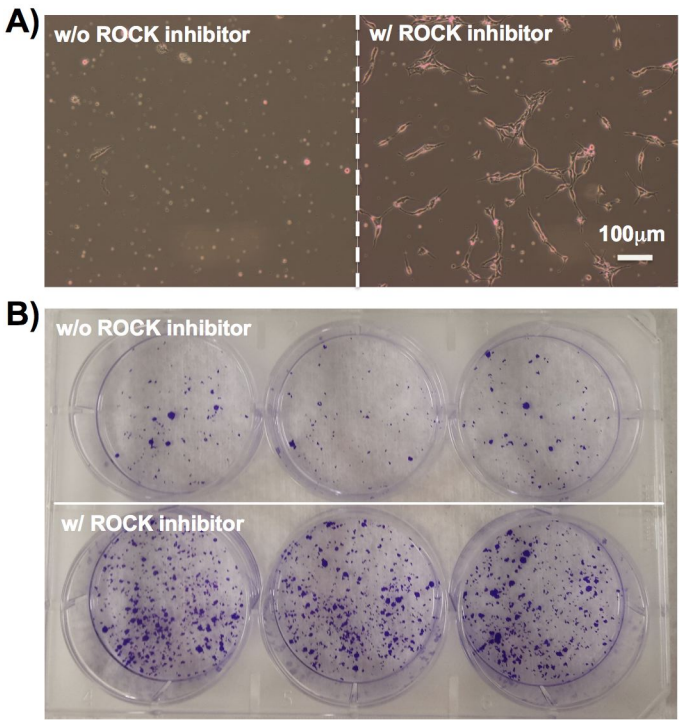

Figure III-7. Flow chart describing the transfection protocol of hESCs with siRNA-carrying particles and subsequent NIR laser treatment. Warm PBS dissociation of H9 cells and ROCK inhibitor addition before cell seeding are essential to preserve stem cell viability.

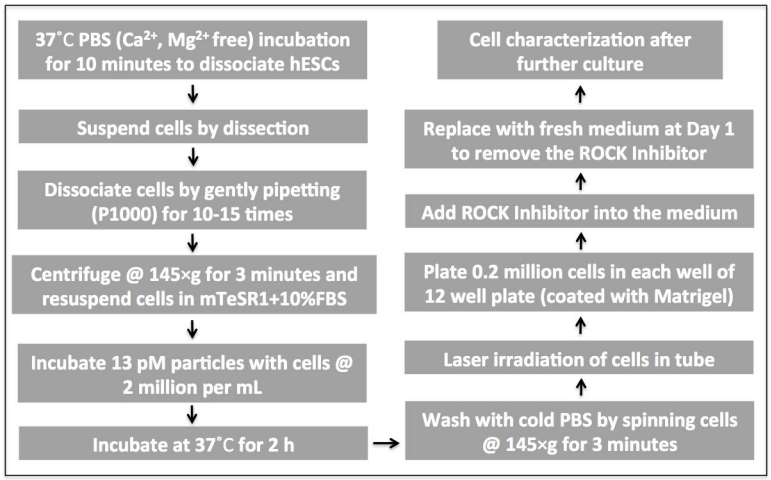

To demonstrate the NIR laser-dependent siRNA activation in hESC, as well as to optimize siRNA delivery efficiency, HGN particles carrying GFP-siRNA were incubated with GFP-expressing hESC (H9-GFP), followed by NIR laser irradiation. Nanoparticles with 6 pmol siRNA were used for 4×10^5 cells (~4000 nanoparticles per cell). A set of different laser powers was tested, and 2.4 W/cm^2 for 15 s was found to have the maximum GFP silencing effect (Figure III-8A) and was selected for later studies. Fluorescence imaging of H9-GFP cells 3 days post treatment showed that GFP expression in cells decreased significantly only when cells carrying particles were irradiated with laser (Figure III-8B).

Flow cytometry quantification of GFP fluorescence in H9-GFP cells at day 3 showed that the mean fluorescence of the whole cell population after particle

Figure III-8. GFP knockdown in H9-GFP cells via HGN-mediated GFP-siRNA delivery and NIR-laser excitation (2.4 W/cm^2 for 15 s). A) Laser power and irradiation duration optimization for effective GFP knockdown in H9-GFP cells. Cells are assayed by flow cytometry 3 days after laser treatment. B) Fluorescence imaging of H9-GFP cells 3 days after HRT (coated with GFP-siRNA) internalization and laser treatment. C) Mean fluorescence intensity of cells with and without HRT and HDT (dsDNA control) and laser treatment. Cells are assayed by flow cytometry 3 days after laser treatment. Lipo: Lipofectamine RNAiMAX siRNA transfection. Data sets are analyzed by one-way ANOVA. **, p < 0.01; ***, p < 0.001; NS, not significant.

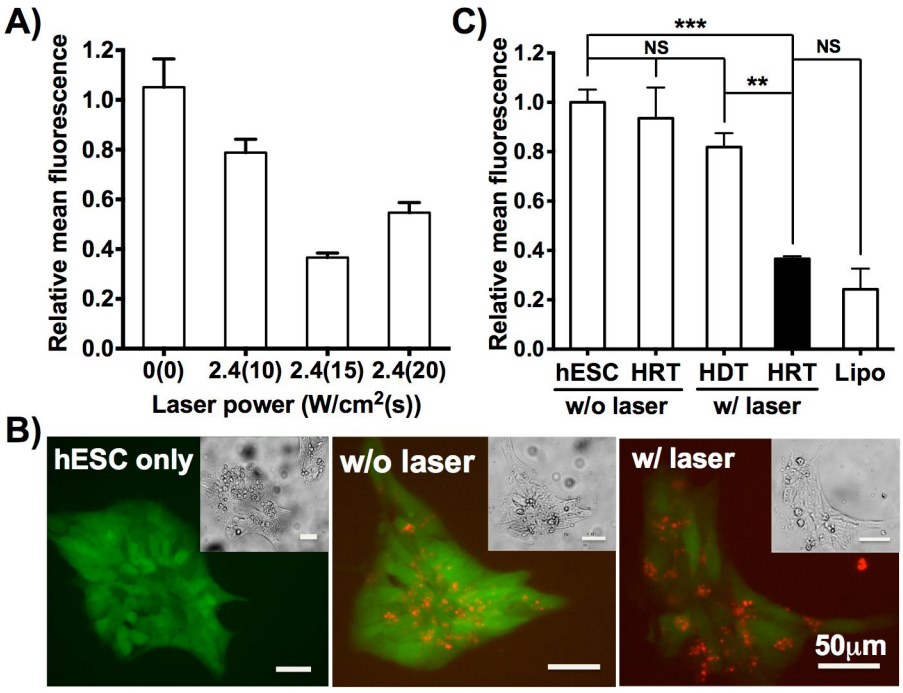

internalization and laser treatment decreased by ~60% compared to cells without particle and laser treatment (Figure III-8C), consistent with the decrease (~66%) of

Figure III-9. GFP knockdown in H9-GFP cells via HGN-mediated GFP-siRNA delivery and NIR-laser excitation (2.4 W/cm^2 for 15 s). Flow cytometry shows the population of high GFP expression (within the bar range) decreased by 66% after knockdown.

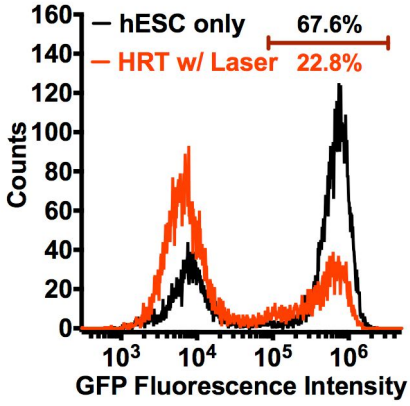

the cell population with high GFP expression (Figure III-9). This down-regulation efficiency is similar to the best data using commercially available transfection reagents including Lipofectamine 2000, jetPRIME, and Lipofectamine RNAiMAX (with 15 pmol siRNA for 1×10^5 cells) (Figure III-8C and Figure III-10), but our method requires ~ten-fold less siRNA. The knockdown efficiency of our method can be further increased by optimizing particles to release more of the siRNA load upon laser treatment, and by modifying the laser irradiation protocol to illuminate the entire cell population. GFP expression remained unchanged in the controls, including cells incubated with GFP-siRNA-carrying HRT without laser irradiation, cells incubated with non-sense dsDNA-carrying HDT and with laser irradiation, and cells without nanoparticles or laser treatment (Figure III-8C). Collectively,

Figure III-10. Fluorescence microscopy imaging of H9-GFP cells 72 h after siRNA transfection using the commercial transfection reagents Lipofectamine 2000 (Lipo2000), jetPRIME (JetPrime), and Lipofectamine RNAiMAX (LipoMAX) with siRNA concentration at 15 nM. LipoMAX shows the best siRNA transfection efficiency.

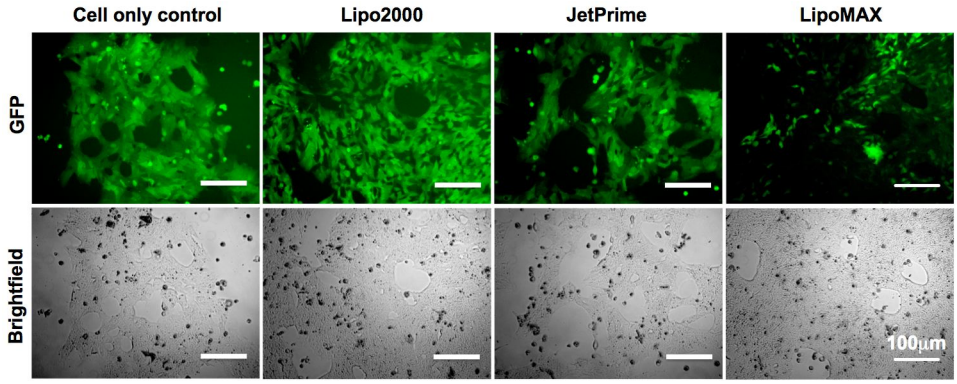

these findings strongly suggest that down-regulation of GFP results from siRNA being released from HRT nanoparticles, and that NIR laser irradiation is necessary for such siRNA activation in the cells.

E. HGN internalization in un-engineered hESC and cytotoxicity assay

The HRT nanoparticle was then tested for the penetration into un-engineered hESC with our optimized transfection protocol (Figure III-7). We labeled siRNA with Quasar570 to track the internalization of HRT into hESC H9 cells over a 2 h incubation at 37 ˚C. Dark-field microscopy of cells after nanoparticle incubation showed orange-red puncta, due to the light scattering of HGN, surrounding the cell nucleus and this co-localized with the red fluorescence puncta from Quasar570 (Figure III-11A). Confocal fluorescence microscopy 3D

Figure III-11. Cellular uptake of HRT in un-engineered hESC. A) Microscopic visualization of particles internalized by hESC H9 cells. Left: Dark-field imaging of cells shows gold punctate dots (yellow), which are co-localized with red fluorescent puncta (from Quasar570) surrounding the nucleus (blue, middle). Right: 3D image of a single cell by confocal fluorescence microscopy shows nanoparticles (red puncta from Quasar570) around the nucleus. B) Flow cytometry quantification of particle internalization and laser release in H9 cells. HRT(Lipid): HGN-siRNA-TAT by lipid coating strategy. Top right: mean fluorescence of each peak indicates the release of fluorescent payload. C) HRT is efficient (>97%) in penetrating a series of different hESC cell lines including H1, H7, H9 and H14. The bar is defined as being above the brightest 1% of the unlabeled control cells.

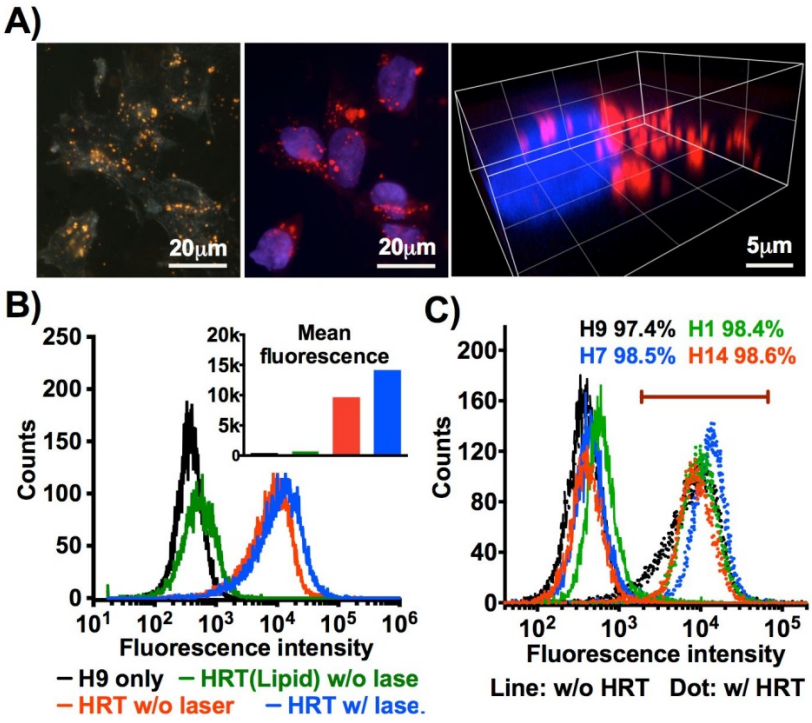

images of selected single cells confirmed the intracellular distribution of the siRNA (likely inside endosomes) near the nucleus (Figure III-11A). We quantified the cellular internalization by flow cytometry using the Quasar570 fluorescence intensity and the fluorescence change after pulsed NIR laser irradiation (Figure III-11B). Approximately 97% of the H9 cell population showed significant fluorescence due to HRT uptake, defined as being brighter than the brightest 1% of the unlabeled control cells. We observed that the mean fluorescence of the cells was increased by 44% after laser irradiation, consistent with RNA payload release (since Quasar570 is partially quenched when near the gold surface [41]). Importantly, HRT showed similar high internalization efficiency (>97%) across a series of hESC cell lines including H1, H7 and H14 (Figure III-11C).

To assess any effect from particles and laser treatment to cell viability, H9 cells containing HRT with double-stranded RNA (non-sense to H9 cells) were exposed to NIR laser of different powers, and cultured on Matrigel-coated plates for 5 days. Live cells growing on the plate were stained with crystal violet, while dead cells that had lost the ability to attach were washed during fresh medium exchange every other day [42, 43]. Figure III-12 shows that the laser irradiation with power and time at or below 2.4 W/cm^2 for 15 s had no significant impairment on cell viability, compared to untreated control cells. Cell stemness was also not affected, judging by cell morphology 7 days after particle and laser treatment (2.4 W/cm^2 for 15 s), since it was normal for untreated cells to have large nuclei and be tightly

Figure III-12. Cell viability assessment of H9 cells after internalization of HRT (with dsRNA coating non-sense to H9 cells) and treatment with different laser powers. Top panel: cell colonies stained by crystal violet 5 days post laser treatment.

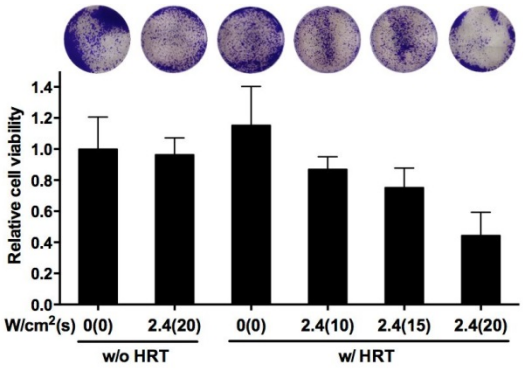

Figure III-13. Morphology of H9 cells 7 days after treating with HRT (with dsRNA coating non-sense to H9 cells) and NIR laser (2.4 W/cm^2 for 15 s). Cells internalized with nanoparticles with or without laser treatment show the same cell morphology as cell only control: cells have large nuclei and are tightly packed to form colonies with smooth edges.

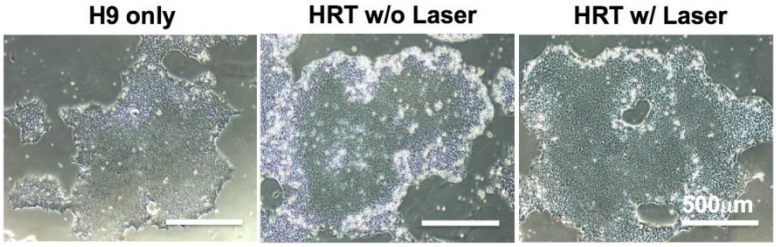

packed to form colonies with smooth edges (Figure III-13) [44]. Importantly, since the expression levels across a panel of stem cell biomarkers was not changed after laser irradiation of cells loaded with HDT, which carries a control double-strand DNA (non-sense to H9), we conclude that specific stemness changes can only be

related to the RNA activity, not the effects of the laser, gold, streptavidin, or peptide.

F. Light-activated Oct4 knockdown accelerates hESC differentiation

Inspired by the success of HGN-siRNA delivery in H9-GFP cells described above, we next set out to deliver siRNA to the original un-engineered H9 cells to down-regulate a gene with biological activity and investigate the biological outcomes. We chose to target the expression of the Oct4 gene, which is an essential transcription factor for embryonic stem cell self-renewal and pluripotency [45]. The down-regulation of this protein was reported to initiate and accelerate differentiation [45]. We first tested the siRNA knockdown of the Oct4 gene in H9 cells using a lentiviral transfection method with the plasmid LL-OCT4-1/2 (Addgene) (Figure III-14). The down-regulation of Oct4 expression in hESC H9 cells by this means initiated the differentiation process in the mTeSR1 medium (control was only barely differentiated) (Figure III-14B) and accelerated this process in the differentiation medium (control was slower) (Figure III-14C). The cells stained positive for all three germ layer markers after extended culture in the differentiation medium (Figure III-14C). In parallel, we incubated H9 cells with our HRT construct HGN-siRNA(Oct4)-TAT and treated them with the NIR pulsed laser at 2.4 W/cm2 for 15 s optimized from H9-GFP knockdown experiment and cell viability test, followed by cell assays after 5 days culture in mTeSR1 medium to get enough cells (Figure III-15A). These conditions stimulated Oct4-siRNA function, as demonstrated by a significant decrease of OCT4 protein expression level at day 5

Figure III-14. *Oct4* gene knockdown in hESC H9 cells by lentiviral transfection results in stem cell differentiation into all three germ layers after the knockdown in mTeSR1 medium. A) Western blot analysis showing the knockdown of *Oct4* gene expression in H9 cells 6 days after lentiviral transfection. The bar graph beneath summarizes densitometric intensity ratio of OCT4 to β-actin. B) Flow cytometry of H9 cells immunostained with stem cell markers TRA-1-60 and SSEA4 11 days post lentiviral transfection in mTeSR1 medium. C) Immunocytochemistry of βIII-tubulin (TUBB3, ectoderm marker), α-smooth muscle actin (α-SMA, mesoderm marker) and α-fetoprotein (AFP, endoderm marker) on H9 cells 22 days after lentiviral transfection (12 days in mTeSR1 followed by 10 days in the differentiation medium) showing differentiation into all three germ layers.

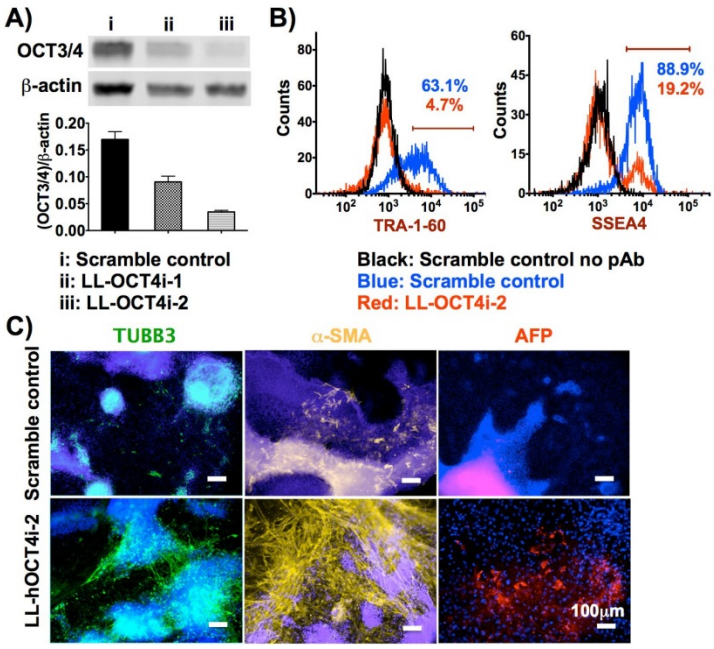

Figure III-15. Release of *Oct4*-siRNA from HRT in H9 hESC cells by NIR laser (2.4 W/cm^2 for 15 s) down-regulates OCT4 protein levels and leads to stem cell differentiation in the mTeSR1 medium. A) Time schedule of the whole protocol and assays of particle and laser treatment to cells. B) ICC staining of H9 5 days after particle internalization and laser treatment. C) Flow cytometry of H9 cells stained with stem cell markers 5 days post particle and laser treatment in mTeSR1 medium, compared to the undifferentiated cells in controls (hESC only, HRT without laser and HDT with laser). D) Western blot analysis of OCT4 protein level in H9 cells. The bar graph underneath shows the band intensity ratio of OCT4 to β-actin in the Western blot image. E) Morphology of cells 5 days post HRT or HDT and laser treatment (cultured in the mTeSR1 medium).

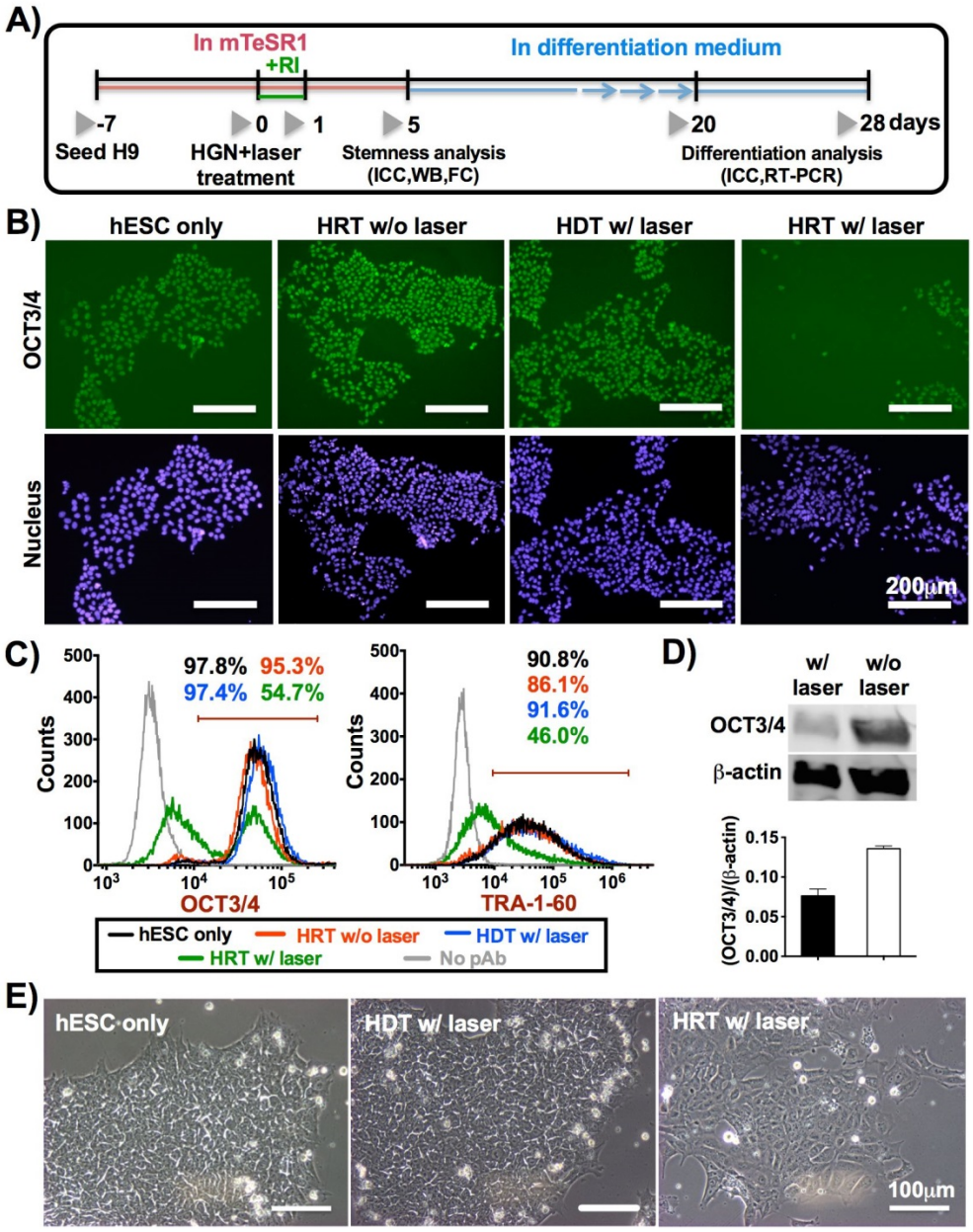

confirmed by immunocytochemistry (ICC) staining and Western blot assay (Figure III-15B-D). Flow cytometry quantification at day 5 (cells cultured in mTeSR1 medium) showed that ~50% of the cell population had decreased their expression of stem cell markers including OCT3/4 and TRA-1-60, as evidence of cell differentiation (Figure III-15C). Limited by cell number, our analysis of the

Figure III-16. H9 cell morphology in mTeSR1 medium 1, 3, 5 and 7 days after HRT (with *Oct4*-siRNA coating) and laser (2.4 W/cm^2, 15s) treatment, relative to negative control. Differentiation morphology with expanded cytosol and dissociated colonies is observed on day 5.

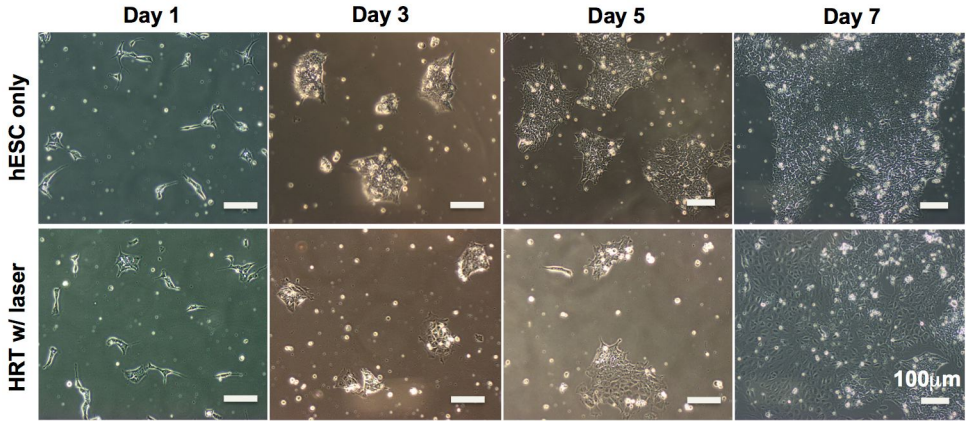

knockdown and differentiation assay carried on day 5 might be an underestimation of the true knockdown efficiency since we noticed that undifferentiated cells divide more quickly than differentiated cells in mTeSR1 medium.

Figure III-15E and Figure III-16 show that cells cultured with HRT and exposed to laser treatment exhibited differentiated cell characteristics: enlarged cell size, increased cytoplasmic area with decreased nuclear-to-cytoplasmic ratio. Consistent with the GFP knockdown experiments, laser exposure of HRT was required for the knockdown effect. Cells treated with HDT (HGN-dsDNA-TAT carrying non-sense dsDNA) did not show any apparent down-regulation of OCT4 protein, loss of stem cell markers or stem cell morphology change (Figure III-15C,E), supporting that the particle internalization and laser treatment themselves have no side effects on cell stemness. Together, the results confirm that the down-

regulation of *Oct4* gene in H9 cells by this strategy leads to stem cell differentiation in a NIR laser-dependent manner.

As laser-induced siRNA delivery in hESC has not been explored previously, we investigated whether this method might cause cell differentiation to be biased toward certain germ layers. Cells were siRNA-treated and then assayed from day 20-28 by ICC staining of three germ layer biomarkers including βIII-tubulin (TUBB3, for ectoderm), α-smooth muscle actin (α-SMA, for mesoderm) and α-fetoprotein (AFP, for endoderm), and reverse transcription PCR (RT-PCR) analysis of several biomarkers' mRNA expression (Figure III-17A). Note that after the particle and laser treatment, the cells were switched to the differentiation medium to avoid the overwhelming growth of undifferentiated cells in mTeSR1 medium, then further cultured and assayed. Consistent with our observation from lentiviral *Oct4* knockdown, HGN- and laser-dependent *Oct4* knockdown accelerated the differentiation process compared to untreated self-differentiation in differentiation medium, as indicated by biomarker ICC staining and RT-PCR analysis (Figure III-17B,C). H9 cells without particle and laser treatment (but with the same culture protocol) showed an apparently lower expression of TUBB3 and AFP at day 28, as compared to cells with particle and laser treatment (Figure III-17B). RT-PCR analysis of biomarkers for all three germ layers confirms the delay at the mRNA level of untreated cells (Figure III-17C). Importantly, both ICC and RT-PCR analysis

Figure III-17. The HGN and NIR laser-mediated *Oct4* gene knockdown accelerates the ability of hESC H9 cells to differentiate into all three germ layers in differentiation medium. A) Time schedule of cell differentiation test in differentiation medium post laser irradiation. B) ICC of βIII-tubulin (TUBB3, ectoderm marker), α-smooth muscle actin (α-SMA, mesoderm marker), and α-fetoprotein (AFP, endoderm marker) for cells 20 or 28 days (20 for α-SMA, 28 for TUBB3 and AFP) after particle and laser treatment. C) RT-PCR analysis of differentiation biomarkers in H9 cells 19 and 21 days after particle and laser treatment. MAP2: ectoderm; BRACHYURY: mesoderm; FOXA2, AFP, CDX2: endoderm.

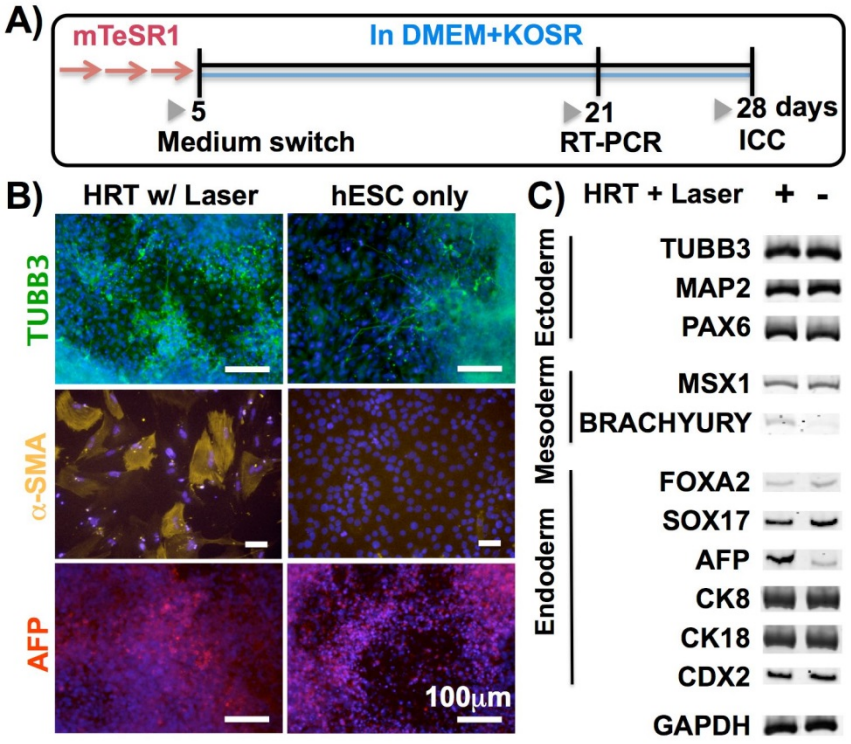

demonstrate that treatment using HRT and NIR laser does not change the ability of H9 cells to differentiate into all three germ layers (Figure III-17).

G. Summary

We have successfully developed a strategy to control RNAi in human embryonic stem cells using a near-infrared laser. To achieve efficient uptake we developed a new modular design for hollow gold nanoshells that couples a targeting peptide to the siRNA. The nanoparticles each carry thousands of siRNA molecules and a streptavidin capsid, which when combined with the TAT peptide, efficiently penetrated into a broad range of hESC including H1, H7, H9 and H14. Internalization of the constructs was tracked and quantified by flow cytometry. Exposure to femtosecond pulses of NIR light caused *GFP* and *Oct4* knockdown in hESC, and differentiation to all three germ layers, supporting the biocompatibility of this novel method. This strategy enables laser printing of siRNA in stem cells with cellular-level resolution at a desired time, and will hence offer new avenues in stem cell basic research and stem cell tissue engineering for regenerative medicine, for example as a tool to probe effects on tissue development.

H. Materials and methods

1. Cell culture

The human embryonic stem cells H1, H7, H9 and H14 (WiCell Research Institute) were maintained on Matrigel (BD Biosciences) coated 6-well plates (BD Falcon) with mTeSR1 medium (Stem Cell Technologies) at 37 ˚C in 5% CO_2. Cells were passaged by manual dissection without enzymatic dissociation every 5-7 days. For differentiation, H9 cells were cultured with differentiation medium (Dulbecco's

modified Eagle's medium (DMEM)/F12, 20% knockout serum replacement, 0.1 mM MEM nonessential amino acid solution, and 0.1 mM β-mercaptoethanol (all from Invitrogen)). HEK293T cells (CRL-11268) and HeLa cells (ATCC) were maintained in DMEM supplemented with 10% fetal bovine serum. 50 μg/mL Normocin (InvivoGen) was supplemented in cell culture media.

2. Lentiviral transfection of hESCs to transduce *GFP* gene and silence *Oct4* gene

Lentiviral vector pLVTHM-scramble (a gift from Dr. Zach Ma, UCSB) containing a eGFP tag was used to generate a transduced H9-GFP cell line. Lentiviral vectors LL-hOCT4i-1 and LL-hOCT4i-2 (Addgene #12197, #12198) were used for the expression of *Oct4*-shRNA in H9 cells. Lentiviral vector pLVTHM-scramble containing a non-targeting scrambled shRNA was also used as the negative control for *Oct4 gene* knockdown (shRNA: GCUUGUUCGUUGGUAACUACAUU). Lentiviral vector plasmids along with psPAX2 (Addgene #12260) and pMD2.G (Addgene #12259) were transfected into HEK293T cells to generate the viral particles. After 48 h and 72 h, supernatants were collected, filtered through a 0.22 μm filter, and concentrated by PEG-it (System Biosciences) precipitation and centrifugation at 1500×g for 30 minutes. A viral titer was performed by transducing Hela cells with several different dilutions of isolated virus. Passage 54-56 H9 cells were dissociated to cell aggregates (~20 cells per aggregate) using cell dissociation buffer (CDB, Invitrogen) and plated on Matrigel-coated 6-well plates, and after seeding for one day, cells were incubated

with concentrated virus for another 24 h in the presence of 0.6 μg/mL polybrene (Millipore). Seven days post transduction, cell colonies were assayed for GFP or OCT4 protein expression. For generating stable H9-GFP cells, colonies with high GFP expression were manually dissected and screened for 2-3 passages.

3. siRNA transfection of hESCs with commercial reagents

Testing of commercially available transfection reagents Lipofectamine 2000 (Invitrogen) and jetPRIME (Polyplus-transfection Inc.) in transduced H9-GFP cells was conducted by measuring GFP expression after GFP-siRNA (IDT EGFP-S1 DS Positive Control) transfection. Cells were dissociated using CDB buffer treatment and plated on a 24-well plate (5×10^4 cells per well) in the presence of ROCK Inhibitor (Y-27632, Millipore) at 10 μM. The following day the transfection was performed according to the manufacturer's protocol: 1 μL of Lipofectamine 2000 or jetPRIME with 15 nM siRNA was added to each well following medium exchange (mTeSR1 + 10% FBS, no Normocin). After 24 h, the medium was replaced with fresh mTeSR1 medium. Cells were imaged by fluorescence microscopy three days after the transfection to assay GFP expression.

4. siRNA coating on HGNs and TAT peptide functionalization

Thiolated sense RNA or DNA strands (Table III-1, Biosearch) were assembled on HGNs followed by the hybridization of complementary strands (Table III-1, Biosearch) to form siRNA or DNA duplexes and the backfilling steps, using the protocol described in Chapter II-H (1-3). The siRNA sequences for *GFP*

and *Oct4* gene knockdown are listed in Table III-1. Thereafter, a large excess (~1.5 mg/mL) of NHS-PEG_4-Biotin (Thermo SCIENTIFIC, #21362) dissolved in 50 μL DMSO was added to 1 mL ~0.1 nM HGN-dsDNA or siRNA to functionalize the 3' end of thiol-DNA or -RNA with biotin. The solution was sonicated briefly and incubated for 1 h at RT, followed by washing with conjugation wash buffer twice to remove excess functionalizing reagent. All the nanoparticle washing steps were performed by centrifuging at ~7000×g for 10 minutes and resuspending the pellet in the respective buffer outlined below through brief sonication.

Streptavidin (PROzyme) was then coated on biotinylated oligonucleotides on HGN to bridge between nucleic acid and biotinylated TAT peptide, by adding at 1 mg/mL to ~0.05 nM nanoparticle in the presense of 0.5× PBST (DPBS with 0.1% Tween-20) and incubating at RT for 1 h after brief sonication. To avoid the particle self-aggregation that may be caused by streptavidin bridging, the solution was vortexed and sonicated immediately upon the addition of streptavidin. The sequential washing of particles with two kinds of buffer (assembly washing buffer and conjugation washing buffer) enhanced the nanoparticle monodispersity. HGN-dsDNA or siRNA with streptavidin coating was finally coated with biotin-TAT (N-terminal biotin, YGRKKRRQRRR, GenScript) to form the multivalent TAT peptide layer on the outside, of which biotin-TAT was added to ~0.05 nM nanoparticle twice at 15 μM in the presence of 0.5× PBST followed by brief sonication and 30 minutes incubation at RT. The nanoparticles were then sequentially washed with assembly washing buffer and conjugation washing buffer

again, and concentrated to ~0.3 nM by centrifugation at ~7000×g for 10 minutes and the pellet was resuspended in conjugation wash buffer. Particles with nucleic acid and TAT peptide coating were stored at 4˚C prior to adding to cells.

5. Particle transfection and NIR laser irradiation to hESCs

hESC including H1 (passage 38-40), H7 (passage 40-42), H9 (passage 60-70), and H14 (passage 66-68) on 6-well plates were dissociated by rinsing and incubating with 500 μL PBS (Ca^{2+} and Mg^{2+} free, Invitrogen #10010-023) at 37 ˚C in 5% CO_2 atmosphere for 10 minutes followed by manual dissection to suspend the cells. The suspended cell aggregates solution was added with 1 mL mTeSR1+10%FBS and pipetted gently with P1000 pipette for 10-15 times to further decrease the size of the cell aggregates. Thereafter, cells in the format of single cell or small cell aggregates (5-10 cells per aggregate) were centrifuged at 145×g and resuspended in mTeSR1+10%FBS at ~2×10^6 cells/mL.

13 pM of coated particles (after brief sonication) were added to 200 μL of cell suspension and incubated in 1.5 mL Eppendorf tubes at 37 ˚C for 2 h, with the gently pipetting of the solution by P1000 pipette for 5 times every 30 minutes. Cells were washed by adding 1.2 mL cold PBS, centrifuging at 55×g for 3 minutes and resuspending in 45 μL cold PBS. Tubes with ~50 μL of cell suspension were irradiated with 2.4 W/cm^2 pulsed NIR laser for 15 s by the output of femtosecond Ti:sapphire regenerative amplifier (Spectraphysics Spitfire) with the same setup as described in Chapter II-H (8). The laser beam diameter was ~4 mm with the spectral range of 800 ± 6 nm, and the pulse duration was ~130 fs with the repetition

rate at 1 kHz. The cells were either used for fluorescence intensity measurements by flow cytometry or plated in Matrigel-coated 12-well plates (~2×10^5 cells per well) in the presence of 10 μM ROCK Inhibitor over the first 24 hours.

6. Imaging of particles in hESCs

hESCs were dissociated into single cells and small aggregates by PBS treatment as described above followed by seeding on a Matrigel-coated 4-well chamber Permanox slide (Lab-Tek #70400) (~4×10^4 cells per well) in the presence of 10 μM ROCK inhibitor. The next day, coated nanoparticles were added at 13 pM after the medium switch to mTeSR1+10%FBS, and the cells were incubated at 37˚C in 5% CO_2 atmosphere for 2 h. After that, cells were washed in PBS twice, fixed in 4% paraformaldehyde (PFA) (VWR International, LLC) in PBS, and washed in PBS again. Cell nuclei were stained using Hoechst 33342 (Sigma-Aldrich). Samples were mounted with Gel/Mount (Electron Microscopy Science) and visualized under light and fluorescence microscopy.

Dark-field scattering images were recorded using an Olympus BX51 upright microscope with a reflection-mode high numerical aperture darkfield condenser (U-DCW, 1.2-1.4). A 100×/1.30 oil Iris objective (UPLANFL) was used to collect only the scattered light from the samples. Images were recorded using a QImaging Retiga-2000R Fast 1394 camera with RGB color filter module, while fluorescence images were taken under the mono module.

Laser scanning confocal microscopy was performed using an Olympus Fluoview 1000, with 405 nm and 559 nm lasers under the presets of DAPI (blue)

and Quasar570 (red), in sequential linescan mode. 24 slices in Z-stack with 0.4 μm increments were obtained from a single cell scan, and images were then digitally assembled using Imaris software to generate the 3D construction image of cells.

7. Flow cytometry analysis

Fluorescence intensity of GFP expression, quantification of the particle internalization from the Quasar570 fluorescence label, and the immunocytochemistry staining levels of OCT4, SSEA and TRA-1-60 were measured using BD Accuri C6 flow cytometer with a flow rate of 14 μL/min. The gate was based on the lineage range of forward and side scattering plots, and 10,000 gated events were collected for each sample. To assay particle internalization from Quasar570 and GFP expression, cells were dissociated into single cells with Accutase (Life Technologies) and collected to directly inject into the flow cytometer for analysis.

OCT4, SSEA4 and TRA-1-60 protein quantification was performed by collecting cells in suspension and staining through immunocytochemistry as follows: cells were fixed in 4% PFA in PBS (4 ˚C, 20 minutes) after the dissociation of cells using Accutase. For OCT4 immunocytochemical staining, additional cell permeabilization was performed in 0.2% Triton-X-100 (Sigma-Aldrich) with 0.1% bovine serum albumin (BSA) (Sigma-Aldrich) for 3 min. After washing in PBS with 0.5% BSA, approximately 200 μL of cell suspension containing 2×10^5 cells were incubated with primary antibodies OCT4 (Santa Cruz Biotechnology #sc-5279), SSEA4 (Millipore #MAB4304), and TRA-1-60

(Millipore #MAB4360) for 30 minutes at RT. Cells were then collected by centrifugation, washed in 0.5% BSA and incubated with secondary antibody Alexa Fluor 488 Goat-anti-Mouse IgG, IgM (H+L) (Invitrogen A10680) for 30 minutes at RT. Finally, cells were washed, resuspended in 200 μL PBS, and injected in flow cytometer for analysis.

8. Immunocytochemistry of attached hESCs

Attached hESCs in culture were washed with PBS, fixed with 4% PFA in PBS (4 ˚C, 20 minutes) and washed with PBS again. Cells were then permeabilized by incubating with the blocking solution [1% Goat Serum (Invitrogen) + 1% BSA (Sigma-Aldrich) + 0.1% NP40 (Sigma-Aldrich)] for 1 h at RT. Thereafter, cells were incubated with primary antibodies OCT4, βIII-tubulin (Sigma #T8660), α-smooth muscle actin (Sigma #A5228) and α-fetoprotein (Santa Cruz Biotechnology #sc-166325) diluted in the blocking solution for 1 h at RT. After three PBS washes, all samples were incubated with secondary antibody Alexa Fluor 488 Goat-anti-Mouse IgG, IgM (H+L) diluted in the block solution for 1 h at RT. Following the nuclei staining using Hoechst 33342, cells were imaged with an Olympus IX70 inverted microscope.

9. hESC cell viability assay

The effect of particle internalization and NIR laser treatment to stem cell viability was assayed by cell coverage area analysis on plate after days. The treated or untreated control cells were seeded on Matrigel-coated 12-well plate at 2×10^5

cells per well and cultured using mTeSR1 medium for 5 days (in the presence of 10 μM ROCK inhibitor in the first 24 hours). After washing with cold PBS twice, cells were stained with crystal violet (Sigma-Aldrich) solution (1% in PBS) for 10 minutes, followed an additional four washes with PBS. Only the area covered by cells was stained. The wells were imaged by a digital camera and the images were analyzed the stained area using ImageJ software.

10. Western blotting

Cells in 6-well plate were lysed with RIPA lysis buffer (50 mM Tris, 150 mM NaCl, 1% Triton, 0.5% deoxycholate, and 2 mM EDTA) supplemented with Complete Protease Inhibitor Cocktail (Promega) and harvested by manual dissection to dislodge the cells from the plate. The cell extract was collected in 1.5 mL Eppendorf tube and incubated on ice for 30 minutes, followed by centrifugation at ~12400×g, 4 ˚C for 20 minutes. Loading buffer (6×, 300 mM Tris-HCl, 0.01% w/v bromophenol blue, 15% v/v glycerol, 6% w/v SDS and 1% v/v beta-mercaptoethanol) was added to the supernatant and boiled at 95 ˚C for 10 minutes. Samples were then run on a precast 10% SDS-PAGE gel (Bio-rad).

Proteins on the gel were electro-transferred onto a nitrocellulose membrane (Bio-rad). The membrane was blocked with 5% BSA in PBST at RT for 30 minutes followed by 4˚C overnight incubation with primary antibodies OCT4 (Santa Cruz Biotechnology #sc-5279) and β-actin (Abcam #ab8227) diluted in 5% BSA-PBST buffer. The membrane was subsequently washed three times for 15 minutes using PBST and then incubated for 3 h at RT in 5% BSA-PBST with secondary

antibodies including Alexa Fluor 488 labeled goat anti-mouse IgG (Invitrogen #A11001) and Alexa Fluor 647 labeled goat anti-rabbit IgG (Invitrogen #A21244), followed by washing three times for 15 minutes using PBST. Images were acquired using a GE Healthcare Typhoon 9400 scanner system and the bands were analyzed using the scanner control software.

11. Reverse transcription PCR

Total cell RNA was extracted using RNeasy Mini Kit (QIAGEN #74104) according to the manufacturer's instructions, and RNase-Free DNase Set (QIAGEN #79254) was used to remove genomic DNA contamination during the extraction. ~1 μg total RNA from each sample was subjected to reverse transcription (RT) reaction using High Capacity RNA-to-cDNA kit (Life Technologies #4387406) following the manufacturer's instructions. Final RT products were diluted 10 folds in water and PCR reactions were performed using GoTag Flexi DNA Polymerase (Promega #M8295). 1 μL of cDNA was added in a total volume of 25 μL containing 2 mM $MgCl_2$, 1× PCR buffer, 0.2 mM deoxyribonucleotide triphosphates (dNTPs), 0.5 μM each of the primers (Table III-2, Integrated DNA Technology) and 0.625 unit of Taq DNA polymerase. The PCR settings for all the genes were as follows: 95 ˚C for 2 minutes, 30 cycles through 95 ˚C for 30 s, 59 ˚C for 30 s, and 72 ˚C for 30s, then extension at 72 ˚C for 5 minutes. Reaction for housekeeping gene *GAPDH* was run as control. 2 μL of the PCR mixture was electrophoresed on 8% Native-PAGE gel at 300 V for 1.5 h, followed by CYBER

Gold (Life Technologies, #S-11494) staining and imaging with the GE Healthcare Typhoon 9400 scanner system.

I. Appendix

Table III-1. Oligonucleotides attached on HGNs.

Modified Oligos	5'	Sequence (5'→3')	3'
siGFP sense	Thiol-PEG18	ACCCUGAAGUUCAUCUGCACCACCG	NH_2
siGFP anti-sense	Quasar570	CGGUGGUGCAGAUGAACUUCAGGGUCA	-
siOCT4 sense	Thiol-PEG18	GGAUGUGGUCCGAGUGUGUGGUUCG	NH_2
siOCT4 anti-sense	Quasar570	UUAACCACACUCGGACCACAUCCUU	-
DNA-1	Thiol-PEG18	ACCCTGAAGTTCATCTGCACCACCG	NH_2
DNA-2	Quasar570	CGGTGGTGCAGATGAACTTCAGGGT	-

Table III-2. Primers used for RT-PCR.

Primers for RT-PCR		Sequence (5'→3')	Germ layer
TUBB3	Forward	GCGGATCAGCGTCTACTACAACGAG	Ectoderm
	Reverse	TCAGGCCTGAAGAGATGTCCAAAGG	
MAP2	Forward	GTGGCGGACGTGTGAAAATTGAGAG	
	Reverse	ACGCTGGATCTGCCTGGGGACTGTG	
PAX6	Forward	CATTATCCAGATGTGTTTGCCCGAG	
	Reverse	TGGTGAAGCTGGGCATAGGCGGCAG	
MSX1	Forward	CGAGAGGACCCCGTGGATGCAGAG	Mesoderm
	Reverse	GGCGGCCATCTTCAGCTTCTCCAG	
BRACHYURY	Forward	CCCTCTCCCTCCCCTCCACGCACAG	
	Reverse	GGCGCCGTTGCTCACAGACCACAGG	
FOXA2	Forward	TGGGAGCGGTGAAGATGGAAGGGCAC	Endoderm
	Reverse	TCATGCCAGCGCCCACGTACGACGAC	
SOX17	Forward	CGCTTTCATGGTGTGGGCTAAGGACG	
	Reverse	TAGTTGGGGTGGTCCTGCATGTGCTG	
AFP	Forward	GAATGCTGCAAACTGACCACGCTGGAAC	
	Reverse	TGGCATTCAAGAGGGTTTTCAGTCTGGA	
CK8	Forward	CCTGGAAGGGCTGACCGACGAGATCAA	
	Reverse	CTTCCCAGCCAGGCTCTGCAGCTCC	
CK18	Forward	AGCTCAACGGGATCCTGCTGCACCTTG	
	Reverse	CACTATCCGGCGGGTGGTGGTCTTTTG	
CDX2	Forward	GCAGAGCAAAGGAGAGGAAA	
	Reverse	CAGGGACAGAGCCAGACACT	
GAPDH	Forward	GTGGACCTGACCTGCCGTCT	House-keeping
	Reverse	GGAGGAGTGGGTGTCGCTGT	

J. References

1. Thomson, J.A., et al., *Embryonic stem cell lines derived from human blastocysts.* Science, 1998. **282**(5391): p. 1145-7.
2. Smith, A.G., *Embryo-derived stem cells: Of mice and men.* Annual Review of Cell and Developmental Biology, 2001. **17**: p. 435-462.
3. Enver, T., et al., *Cellular differentiation hierarchies in normal and culture-adapted human embryonic stem cells.* Human Molecular Genetics, 2005. **14**(21): p. 3129-3140.
4. Eguchi, A., et al., *Efficient siRNA delivery into primary cells by a peptide transduction domain–dsRNA binding domain fusion protein.* Nature biotechnology, 2009. **27**(6): p. 567-571.
5. Yau, W.W.Y., et al., *Directing stem cell fate by controlled RNA interference.* Biomaterials, 2012. **33**(9): p. 2608-2628.
6. Heidersbach, A., et al., *RNA interference in embryonic stem cells and the prospects for future therapies.* Gene Therapy, 2006. **13**(6): p. 478-486.
7. Ding, L. and F. Buchholz, *RNAi in embryonic stem cells.* Stem Cell Reviews, 2006. **2**(1): p. 11-18.
8. Park, H.-J., et al., *Nonviral delivery for reprogramming to pluripotency and differentiation.* Archives of pharmacal research, 2014. **37**(1): p. 107-119.
9. Rassouli, F.B. and M.M. Matin, *Gene silencing in human embryonic stem cells by RNA interference.* Biochemical and Biophysical Research Communications, 2009. **390**(4): p. 1106-1110.
10. Shah, B., et al., *Multimodal Magnetic Core–Shell Nanoparticles for Effective Stem-Cell Differentiation and Imaging.* Angewandte Chemie, 2013. **125**(24): p. 6310-6315.
11. Solanki, A., et al., *Nanotopography-mediated reverse uptake for siRNA delivery into neural stem cells to enhance neuronal differentiation.* Scientific reports, 2013. **3**: p. 1553.
12. Ferreira, L., et al., *New opportunities: The use of Nanotechnologies to manipulate and track stem cells.* Cell Stem Cell, 2008. **3**(2): p. 136-146.
13. Ma, Y., et al., *High-level sustained transgene expression in human embryonic stem cells using lentiviral vectors.* Stem Cells, 2003. **21**(1): p. 111-117.
14. Zhang, X.Y., et al., *Lentiviral vectors for sustained transgene expression in human bone marrow-derived stromal cells.* Molecular Therapy, 2002. **5**(5): p. 555-565.
15. Thomas, C.E., A. Ehrhardt, and M.A. Kay, *Progress and problems with the use of viral vectors for gene therapy.* Nature Reviews Genetics, 2003. **4**(5): p. 346-358.
16. Seth, P., *Vector-mediated cancer gene therapy - An overview.* Cancer Biology & Therapy, 2005. **4**(5): p. 512-517.
17. Pack, D.W., et al., *Design and development of polymers for gene delivery.* Nature Reviews Drug Discovery, 2005. **4**(7): p. 581-593.

18. Zhao, M., et al., *Lipofectamine RNAiMAX: An efficient siRNA transfection reagent in human embryonic stem cells.* Molecular Biotechnology, 2008. **40**(1): p. 19-26.
19. Ma, Y., et al., *High-efficiency siRNA-based gene knockdown in human embryonic stem cells.* RNA, 2010. **16**(12): p. 2564-9.
20. Omidi, Y., J. Barar, and S. Akhtar, *Toxicogenomics of cationic lipid-based vectors for gene therapy: impact of microarray technology.* Curr Drug Deliv, 2005. **2**(4): p. 429-41.
21. Omidi, Y., et al., *Microarray analysis of the toxicogenomics and the genotoxic potential of a cationic lipid-based gene delivery nanosystem in human alveolar epithelial a549 cells.* Toxicol Mech Methods, 2008. **18**(4): p. 369-78.
22. Qutachi, O., K.M. Shakesheff, and L.D. Buttery, *Delivery of definable number of drug or growth factor loaded poly (dl-lactic acid-co-glycolic acid) microparticles within human embryonic stem cell derived aggregates.* Journal of Controlled Release, 2013. **168**(1): p. 18-27.
23. Hsu, S.-h., et al., *Efficient Gene Silencing in Mesenchymal Stem Cells by Substrate-Mediated RNA Interference.* Tissue Engineering Part C: Methods, 2014.
24. Shah, S., et al., *Guiding Stem Cell Differentiation into Oligodendrocytes Using Graphene-Nanofiber Hybrid Scaffolds.* Advanced Materials, 2014.
25. Nguyen, M.K., et al., *Sustained localized presentation of RNA interfering molecules from< i> in situ</i> forming hydrogels to guide stem cell osteogenic differentiation.* Biomaterials, 2014. **35**(24): p. 6278-6286.
26. Peng, L.H., et al., *TAT conjugated cationic noble metal nanoparticles for gene delivery to epidermal stem cells.* Biomaterials, 2014. **35**(21): p. 5605-18.
27. Zoldan, J., et al., *Directing human embryonic stem cell differentiation by non-viral delivery of siRNA in 3D culture.* Biomaterials, 2011. **32**(31): p. 7793-7800.
28. Badylak, S.F., D. Taylor, and K. Uygun, *Whole-Organ Tissue Engineering: Decellularization and Recellularization of Three-Dimensional Matrix Scaffolds.* Annual Review of Biomedical Engineering, Vol 13, 2011. **13**: p. 27-53.
29. Gjorevski, N., A. Ranga, and M.P. Lutolf, *Bioengineering approaches to guide stem cell-based organogenesis.* Development, 2014. **141**(9): p. 1794-1804.
30. Prevo, B.G., et al., *Scalable routes to gold nanoshells with tunable sizes and response to near-infrared pulsed-laser irradiation.* Small, 2008. **4**(8): p. 1183-1195.
31. Nakano, T., et al., *Self-Formation of Optic Cups and Storable Stratified Neural Retina from Human ESCs.* Cell Stem Cell, 2012. **10**(6): p. 771-785.
32. Sasai, Y., *Cytosystems dynamics in self-organization of tissue architecture.* Nature, 2013. **493**(7432): p. 318-326.

33. Suga, H., et al., *Self-formation of functional adenohypophysis in three-dimensional culture.* Nature, 2011. **480**(7375): p. 57-U215.
34. Ikeda, E., et al., *Fully functional bioengineered tooth replacement as an organ replacement therapy.* Proceedings of the National Academy of Sciences of the United States of America, 2009. **106**(32): p. 13475-13480.
35. Braun, G.B., et al., *Laser-Activated Gene Silencing via Gold Nanoshell-siRNA Conjugates.* Acs Nano, 2009. **3**(7): p. 2007-2015.
36. Huang, X., et al., *Modular Plasmonic Nanocarriers for Efficient and Targeted Delivery of Cancer-Therapeutic siRNA.* Nano Lett, 2014. **14**(4): p. 2046-51.
37. Lukianova-Hleb, E.Y., et al., *Plasmonic nanobubble-enhanced endosomal escape processes for selective and guided intracellular delivery of chemotherapy to drug-resistant cancer cells.* Biomaterials, 2012. **33**(6): p. 1821-1826.
38. Meade, B.R. and S.F. Dowdy, *Enhancing the cellular uptake of siRNA duplexes following noncovalent packaging with protein transduction domain peptides.* Adv Drug Deliv Rev, 2008. **60**(4-5): p. 530-6.
39. Turner, J.J., et al., *RNA targeting with peptide conjugates of oligonucleotides, siRNA and PNA.* Blood Cells Mol Dis, 2007. **38**(1): p. 1-7.
40. Win, K.Y. and S.S. Feng, *Effects of particle size and surface coating on cellular uptake of polymeric nanoparticles for oral delivery of anticancer drugs.* Biomaterials, 2005. **26**(15): p. 2713-2722.
41. Ray, P.C., A. Fortner, and G.K. Darbha, *Gold nanoparticle based FRET asssay for the detection of DNA cleavage.* Journal of Physical Chemistry B, 2006. **110**(42): p. 20745-20748.
42. He, Y., et al., *Comparison of proliferation and differentiation potential between mouse primary hepatocytes and embryonic hepatic progenitor cells in vitro.* International Journal of Molecular Medicine, 2013. **32**(2): p. 476-484.
43. Huang, E.Y., et al., *Conditionally Immortalized Mouse Embryonic Fibroblasts Retain Proliferative Activity without Compromising Multipotent Differentiation Potential.* Plos One, 2012. **7**(2).
44. Sathananthan, H., M. Pera, and A. Trounson, *The fine structure of human embryonic stem cells.* Reprod Biomed Online, 2002. **4**(1): p. 56-61.
45. Pan, G.J., et al., *Stem cell pluripotency and transcription factor Oct4.* Cell Research, 2002. **12**(5-6): p. 321-329.

IV. Cell-resolution RNA interference of 3D-cultured hESCs

A. Abstract

We describe the first method to regulate gene expression in human embryonic stem cells cultured in three-dimensional (3D) matrix with cell level resolution. Targeted cell(s) are discriminated from neighboring cell(s) by simply focusing the biologically benign near infrared light irradiated from a commonly available two-photon microscope. Irradiation of cells that have internalized hollow gold nanoshells releases surface attached small interfering RNA molecules and leads to concomitant downregulation of gene expression. The ability to induce light-mediated gene knockdown persists for at least two days, offering a time window for temporal control. We anticipate that this level of gene control within a subpopulation of cells in 3D culture will significantly improve the ability to direct *in vitro* organogenesis using pluripotent stem cells, and provide a powerful technique for various *in vivo* biological studies.

B. Introduction

Biological processes are stimulated by various molecular and physical signals orchestrated in space and time [1-4]. Tissue and organ generation *in vitro* for transplant therapy and disease modeling for drug screening [5] are especially demanding for precise control over 3D patterning of different cell types [2, 4, 6, 7]. Advances in this area include the controlled differentiation of pluripotent or multipotent stem cells cultured in 3D matrices followed by self-organization into

tissues *in vitro* [1, 8-11]. However, current methods for organoid formation have insufficient control over the course of the morphogenetic processes and the resulting structures inadequately replicate native tissues [2, 4]. Microfluidic approaches establish organ-level functions *ex vivo* by directly assembling different cell types, but lacks the dimensionality to approximate the developing tissues [2]. Nanotopographic patterning provides spatial control of stem cell differentiation, but is mostly restricted to a two-dimensional plane, limiting the repertoire of cell types generated [12-14].

Light is an ideal stimulus for perturbing the spatiotemporal dynamics of signals in living cells and organisms with high resolution [15-17]. The light-based optogenetic field has moved from proof of concept to answering real biological questions [16], as well as developed tools for light-controlled genome editing and gene transfection [18-22]. However, current optogenetic gene regulation methods rely largely on the visible light excitation sources and the construction of complex protein fusions via viral transfection. Other alternatives use photocaged small molecules and biopolymers like DNA and RNA for light-dependent gene regulation [4, 15, 23-26], which are limited by cellular delivery hurdles and the use of low tissue-penetrating UV-Vis light [15-17].

Herein, we develop a novel pulsed NIR light based technique for the spatio-temporal control of gene regulation in 3D-cultured hESCs. NIR light can be tightly focused three-dimensionally (down to ~1 femtoliter) [27] and can reach deep through tissues [28, 29]. In this method, siRNAs are covalently attached to HGNs

[30-32] presenting a cell-penetrating TAT peptide [33]. Biocompatible NIR light irradiation of the nanoparticles in intended cells releases the RNAs from the nanoparticle surface and from endosomes into the cytosol to selectively regulate gene expression. In this work, we use a commonly available two-photon microscope to focus the NIR laser three-dimensions as a means to carry out cell level RNA interference within 3D hESC "spheroids" cultured in a synthetic thermoreversible hydrogel [34]. We demonstrate selective, cell level resolution *GFP*-siRNA release in 3D-cultured hESCs patterned by NIR light irradiation, with no detrimental effects on cell viability or developmental potential. This light-controlled gene silencing lasts for up to 2 days, providing a time window for spatio-temporal control. This cell resolution RNAi technique provides a novel, powerful means for investigating stem cell differentiation and organogenesis *in vitro* and *in vivo* in model organisms.

C. Nanoparticle transfection of hESC spheroids in a 3D matrix

In order to regulate gene expression in specific hESC spheroids or a subpopulation of cells in 3D culture, we utilized a two-photon microscope (Olympus Fluoview 1000 MPE) to achieve cell level resolution control of NIR light in combination with the technique we pioneered on NIR-light activated siRNA delivery in hESCs [33]. Many copies of siRNA molecules were assembled on HGNs and taken up efficiently by hESCs through TAT peptide mediated endocytosis. Cell clusters formed during particle incubation in the presence of ROCK inhibitor and were switched into a thermoreversible hydrogel (Mebiol® Gel,

Figure IV-1. Spatio-temporally controlled cell resolution gene silencing in 3D-cultured hESCs using HGNs and two-photon microscopy. GFP-expressing hESCs internalized with siRNA-coated HGNs are switched to a medium containing the thermoreversible Mebiol gel in the liquid phase. The mixture is cast as a thin layer (~100-150 µm) of solid-phase gel on a petri dish with a grid on the bottom to allow tracking of individual clusters over time. Cellular clusters or regions within clusters are irradiated with 800 nm laser emitted by a two-photon microscope at selected x, y and z positions. Cells treated with laser are re-located and imaged 3 days after laser irradiation to assess the light-released siRNA activity.

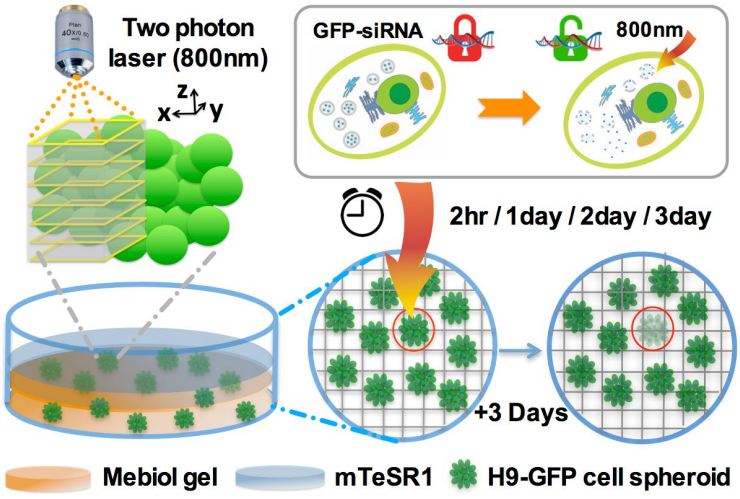

Cosmo Bio Co.), which was then solidified at 37°C. 800 nm femtosecond pulsed laser from the two-photon microscope was then focused at selected x, y and z regions of cell clusters to bring local release of siRNA to the cytosol for gene silencing (Figure IV-1). This strategy allows selective gene regulation within 3D cell assemblies, at cell level resolution.

Figure IV-2. The addition of ROCK inhibitor during particle incubation significantly increases stem cell viability in the 3D matrix and prompts cell aggregation, with no inhibition on particle internalization. A) Schematic of the protocol for casting traceable 3D-cultured stem cell steroids before two-photon microscope imaging and 800 nm laser irradiation. B) Flow cytometry analysis of nanoparticle internalization efficiency with the addition of RI during the nanoparticle incubation process. C) Cell viability test of H9 cells cultured in the 3D matrix for 3 days post particle incubation. Cells from 3D culture are collected and seeded on Matrigel-coated 6-well plate for additional 2 days, followed by the cell viability staining using violet blue.

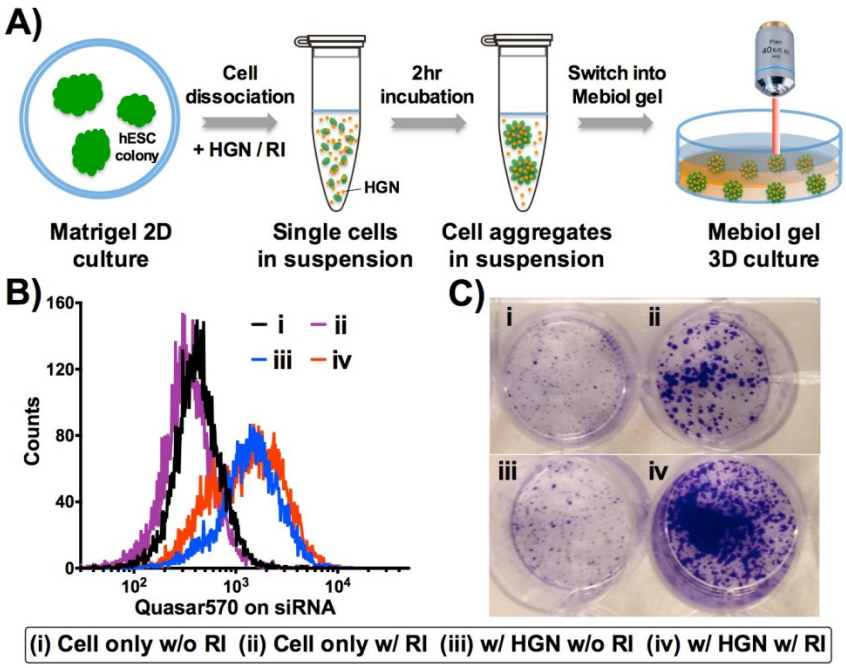

In prior work we showed that a wide variety of hESC lines can be efficiently transfected with HGNs coated with TAT peptide. However, only a small fraction of these single cells survived when switched into the Mebiol gel for 3D culture, which

may be caused by unfavorable culture conditions during HGN transfection steps. Shortening the HGN incubation time resulted in decreased internalization. Because ROCK inhibitor rescues stem cell viability of single cell formats in a 3D matrix [34], we tested the addition of this during HGN incubation (Figure IV-2A). Notably, ROCK inhibitor significantly increased the amount of viable cells in 3D matrix without detectable inhibition of HGN internalization (Figure IV-2B,C). We also observed that dissociated single cells aggregate into cell clusters with ROCK inhibitor treatment (Figure IV-2C), forming cellular spheroids within 3 days. Cells irradiated with NIR light were analyzed for gene expression after 3 days, and the cell-containing hydrogel was casted into a thin layer (100-150 μm thick) on grid-bottomed culture dishes (Ibidi Co.) to track the cells.

We also tested an alternative HGN transfection approach in which particles were supplemented while the developing of hESCs from single cells to spheroids in 3D culture. Fresh medium containing HGNs were fed to gel-encapsulated cells every day to overcome any inefficiency of HGN penetration to inner cells of spheroids [35]. As a result, HGNs distributed equally across the whole body of cellular spheroids generated in the thin hydrogel layer (Figure IV-3). Although we relied largely on transfecting HGNs prior to 3D casting, the alternative method clearly has the advantage in particular circumstances.

Figure IV-3. Efficient nanoparticle transfection can also be achieved by casting stem cells in a thin Mebiol gel layer with nanoparticles supplemented daily in the medium on top. A) Schematic for two strategies of nanoparticle transfection for 3D-hydrogel supported stem cells. Cells are cast either in the thick "Dome" shape or "Thin layer" shape gel with nanoparticles-containing medium replenished every day during the culture. B) Flow cytometry assay of cells 1 day after nanoparticle transfection shown in scheme (A). C) 3D image of stem cells obtained by confocal fluorescence microscopy 3 days after nanoparticle transfection via the "Thin layer" strategy. Red puncta: Quasar570 on siRNA; grey: cell outline.

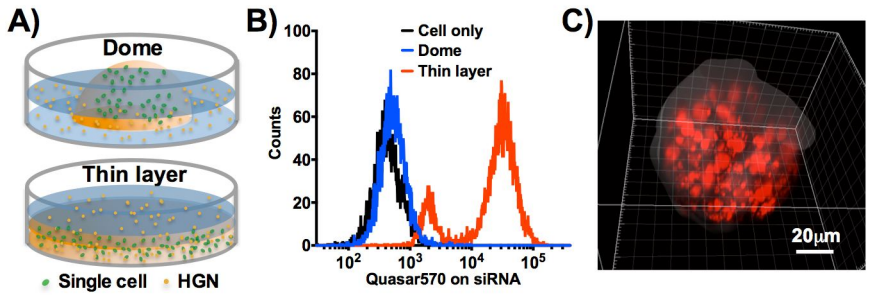

D. Light-activated GFP knockdown in transduced hESC spheroids

hESC H9 cells were transduced with the *GFP* gene to test the light-controlled GFP-siRNA delivery using the two-photon microscope equipped with both single-photon confocal mode and two-photon mode. Following optimization using 2D-cultured HeLa cells (Figure IV-4), NIR laser irradiation was performed using the two-photon mode through z-stacks of the cell cluster with 1.4 μm intervals, and each z-stack (512 × 512 pixels) was scanned line-by-line (2 μsec per

Figure IV-4. NIR laser power optimization for maximum gene silencing effect in *GFP* gene transduced HeLa cells. The femtosecond pulsed laser emitted by the two-photon microscopy is optimized the irradiation intensity at 3%, 5% or 8% of the maximum power with 2 or 4 µsec/pixel. Laser power at 3% with 4 µsec/pixel does not release enough siRNA, whereas 8% with 4 µsec/pixel causes some cell morphology change immediately (red arrow) as a sign of cell damage. 5% (~2 mW) with 2 µsec/pixel is the optimized laser treatment condition with the best knockdown effect but the least cell damage.

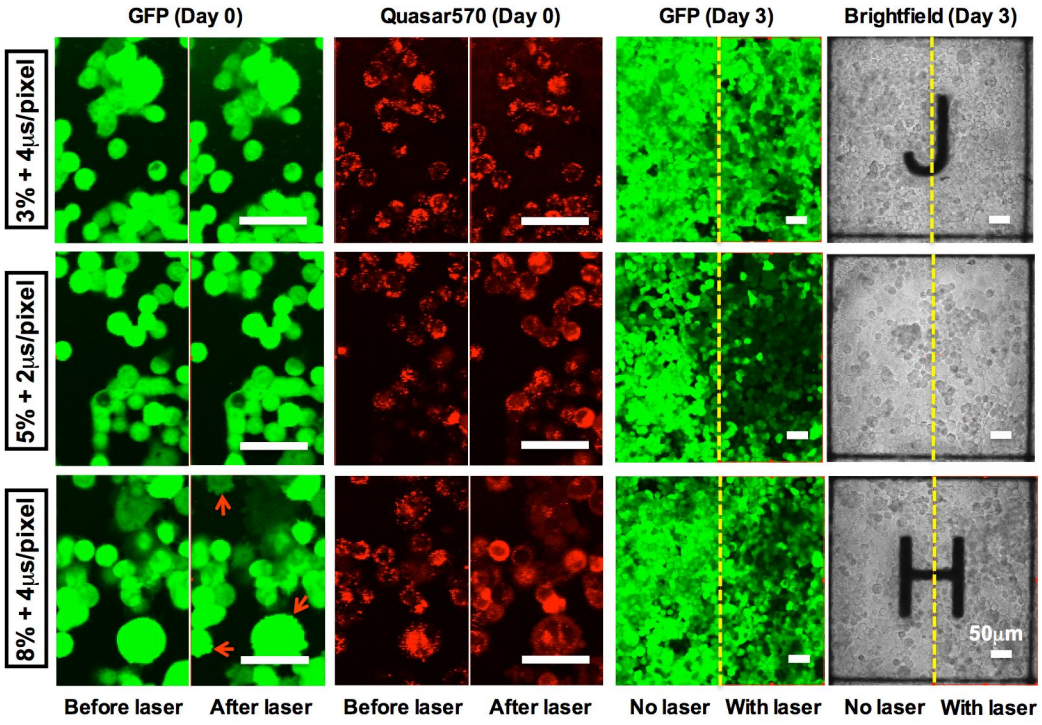

selected pixel, 5% of the maximum power), a total of 5 times. Single-photon confocal imaging was used to reference siRNA release and immediate cellular effect before and after the 3D-selected irradiation in the two-photon mode. Laser

Figure IV-5. *GFP* gene knockdown of 3D-cultured hESC H9 cell clusters by NIR light irradiation. A) Confocal fluorescence microscopy (in single-photon mode) of H9-GFP clusters before and after 800 nm laser irradiation (in two-photon mode) compared to non-irradiated control cluster. B) Fluorescence imaging of the same H9-GFP spheroids shown in (a) 3 days post laser irradiation. C) Averaged GFP intensity of spheroids (3D pixel intensity analysis) 3 days post laser treatment.

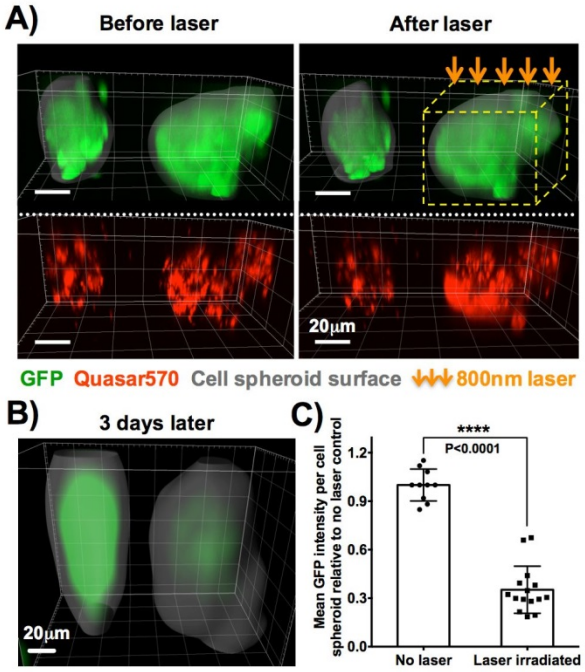

irradiation of hESC H9 cell clusters in the 3D hydrogel stimulated the release of siRNA from internalized HGNs to cytosol, indicated by the brighter and diffused red puncta of Quasar570 (labeled on siRNA) fluorescence after laser irradiation (Figure IV-5A). siRNAs activated by laser treatment successfully down regulated GFP expression (Figure IV-5B,C).

Figure IV-6. NIR laser irradiation to HGNs-internalized H9 clusters in 3D hydrogel at optimized condition has no inhibition to cell growth, compared to no laser control. Assessed by 3D volume analysis, cell clusters treated with HGNs and laser have the same magnitude of size increase as no laser control after 3D culture for 3 days. NS: not significant by student t-test.

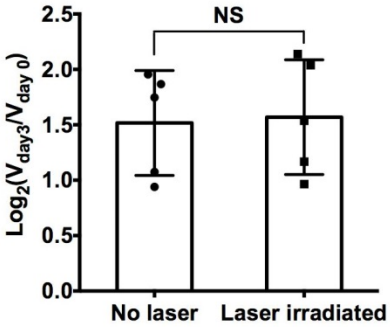

Cells irradiated with the NIR laser grew at the same rate of cells without laser treatment and showed no difference in viability (Figure IV-6). HGN mediated GFP-siRNA delivery to mCherry co-transduced H9 cells resulted in selective GFP knockdown without any detectable changes in mCherry expression, further confirming the specificity of GFP knockdown (Figure IV-7). Markers for cell pluripotency were also probed by immunocytochemistry of cells treated with HGNs and an equivalent NIR laser (femtosecond Ti:sapphire regenerative amplifier, 130 fs pulse duration, 1 KHz repetition rate) with ~4 mm beam diameter covering the whole 3D hydrogel. Similar levels of OCT3/4 and TRA-1-60 were observed in cells treated with HGNs and laser compared to the cell only control and cells treated with HGNs but not laser (Figure IV-8). Thus, this approach is highly biocompatible.

Figure IV-7. Selective GFP knockdown of H9 spheroid co-transduced with *GFP* and *mCherry* genes in a 3D matrix. Fluorescence microscopy of A) GFP and B) mCherry expression in H9 spheroids 3 days after the laser treatment. C) Merged image of (A) and (B). D) Mean GFP and mCherry fluorescence intensity of spheroids 3 days post laser treatment, assayed from the 3D pixel intensity analysis of the cell body region in A) and B).

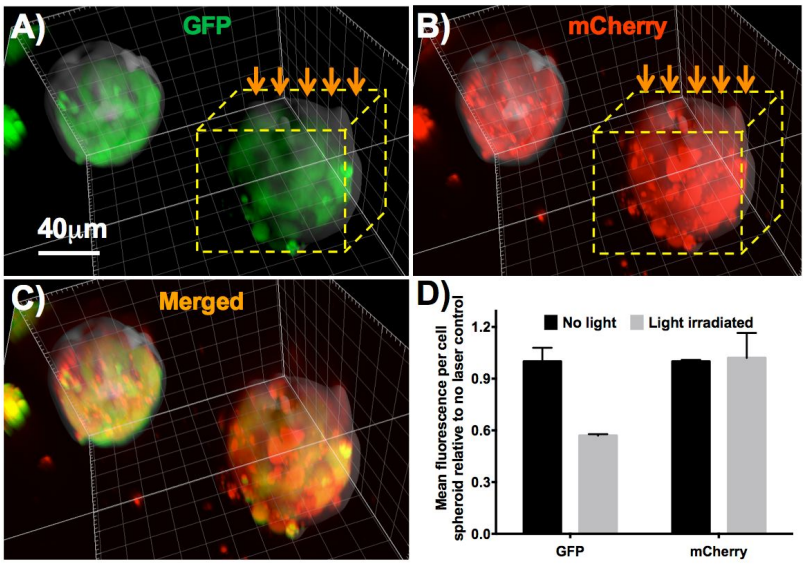

Figure IV-8. NIR laser irradiation of H9 cells in 3D matrix does not affect cell stemness. Flow cytometry of H9 cells stained with OCT3/4 (A) and TRA-1-60 (B) antibodies 3 days post NIR laser treatment in 3D hydrogel followed by 1 day culture on Matrigel plate. Cells treated with HGNs and an equivalent pulsed NIR laser (~130 fs pulse duration, repetition rate at 1 KHz) with 4 mm beam have similar levels of OCT3/4 and TRA-1-60 surface marker expression as those of cell only control and cells treated with HGNs but not laser.

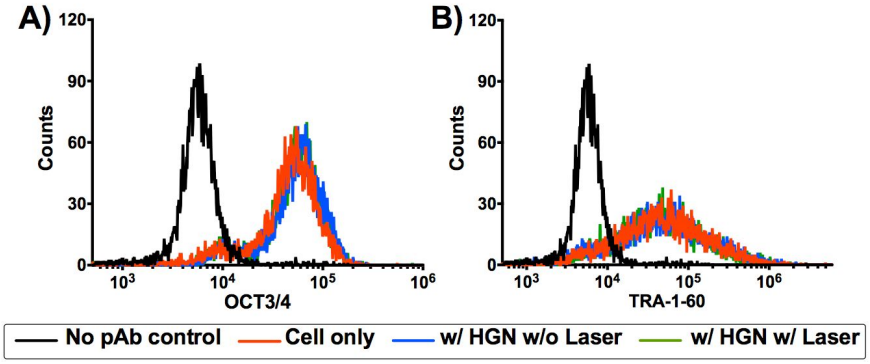

E. Spatially controlled gene silencing

NIR laser activation of a subpopulation of cells within one cell cluster provides unprecedented spatial control. In Figure IV-9, red puncta (Quasar570 fluorescence labeled on siRNA) in the irradiated areas are brighter and more diffuse than surrounding areas, indicating high resolution control of siRNA release guided by the x, y and z laser scanning from the two-photon microscope. Interestingly, although the spheroid retained a similar shape three days after laser treatment, GFP fluorescence of the whole cellular spheroid showed different downregulation patterns: edged, mosaic, and retrograde (Figure IV-10A). In contrast, GFP-

Figure IV-9. Spatially controlled siRNA delivery in hESC spheroids with cell level resolution. A) NIR laser patterned siRNA release (in frames) on a cell free glass slide. B) Laser controlled cell resolution siRNA release (in yellow frame) within one cell cluster in a 3D matrix.

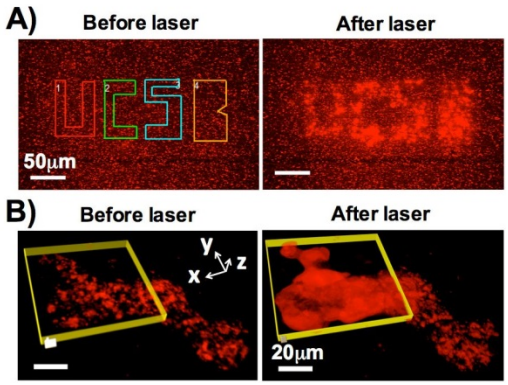

transduced HeLa cells loaded with HGNs and irradiated on a 2D culture dish showed down-regulated GFP expression, but stayed in the original region outlined by the laser (Figure IV-10B). This suggests that undifferentiated H9 cells migrate [36] within the spheroid, and laser irradiation and siRNA release does not inhibit migration (Figure IV-10). We anticipate that as selected cells differentiate, migration may be restricted to allow for the formation of certain spatial patterns and morphologies [1, 10].

Figure IV-10. Spatially controlled gene silencing in hESC spheroids and 2D-cultured HeLa cells with cell level resolution. A) 3D-cultured H9 spheroids with a subpopulation of cells treated with GFP-siRNA show different GFP down-regulation patterns 3 days later: edged, mosaic and retrograde. Top panel: Cells within the yellow dashed line cubes are irradiated with laser; Middle and Bottom panel: GFP fluorescence images of cellular spheroids before and after laser treatment for 3 days. B) 2D-cultured HeLa cells show similar patterns of GFP down-regulation 3 days later as outlined by the laser irradiation. siRNA molecules are labeled with Quasar570 dye (red); GFP fluorescence (Green); Cell outline (grey).

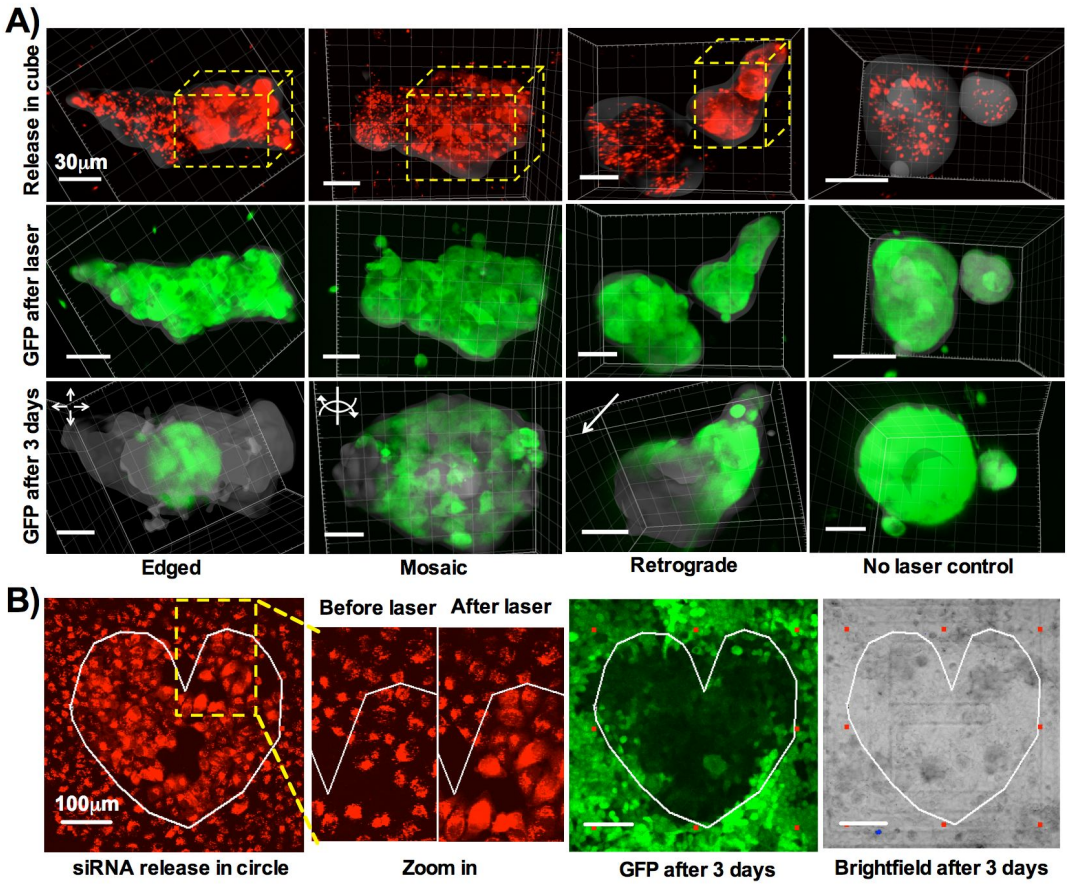

F. Temporally controlled gene silencing

The timing of siRNA activation can also be tuned by laser irradiation. Cellular spheroids were irradiated with NIR laser 2 hours (Day 0), 1 day, 2 days and 3 days post HGN incubation and 3D hydrogel placement. Functionalized HGNs exhibited laser-dependent release of functional siRNA up to 2 days after cellular uptake, while no siRNA activity was observed when the time lag extended to 3 days (Figure IV-11A,B). Consistently, the siRNA signal (by Quasar570 fluorescence) in the 3D-cultured H9 cells dramatically drops 2 days after particle incubation (Figure IV-12). We carried out similar experiments with HeLa cells transduced with *GFP* (~24 hour doubling time [37]) to explore why gene silencing is lost after three days. However, laser irradiation 3 days post HGN internalization still showed effective gene silencing (Figure IV-11C and Figure IV-13), indicating loss in siRNA knockdown is likely due to rapid siRNA degradation in hESCs rather than dilution by cell division.

We found that the siRNA on the HGNs remain intact in buffer at neutral pH for at least a month, whereas overnight exposure to glutathione (GSH) at 0.01 mM releases half of the siRNA (Figure IV-14). Thus, siRNA may be displaced by cellular GSH evidenced by brighter and diffused signals from siRNA label one day after HGN internalization (Figure IV-12). However, considering that the endosome is another barrier to be ruptured by the thermal response of HGNs to laser, irradiation is still the “power on button” for siRNA activity (Figure IV-11). This provides the basis for the spatial control of siRNA release over time.

Figure IV-11. Temporally controlled gene silencing in 3D-cultured H9 cells and 2D-cultured HeLa cells. A) Fluorescence imaging of GFP (green) in 3D-cultured H9 spheroids (grey for cell outline) 3 days post laser irradiation. Cellular spheroids were irradiated with 800 nm laser using the two-photon microscope 2 hours (Day 0), 1 day, 2 days and 3 days after HGN incubation. B) Averaged GFP fluorescence intensity of H9 spheroids in (A) from the 3D green pixel intensity analysis within the cell outline. C) Averaged GFP fluorescence intensity (pixel intensity analysis) of 2D-cultured HeLa cells 3 days post laser irradiation exposed to cells 2 hours (Day 0), 1 day, 2 days and 3 days after particle incubation. *, $p < 0.5$; **, $p < 0.01$; ***, $p < 0.001$; ****, $p < 0.0001$.

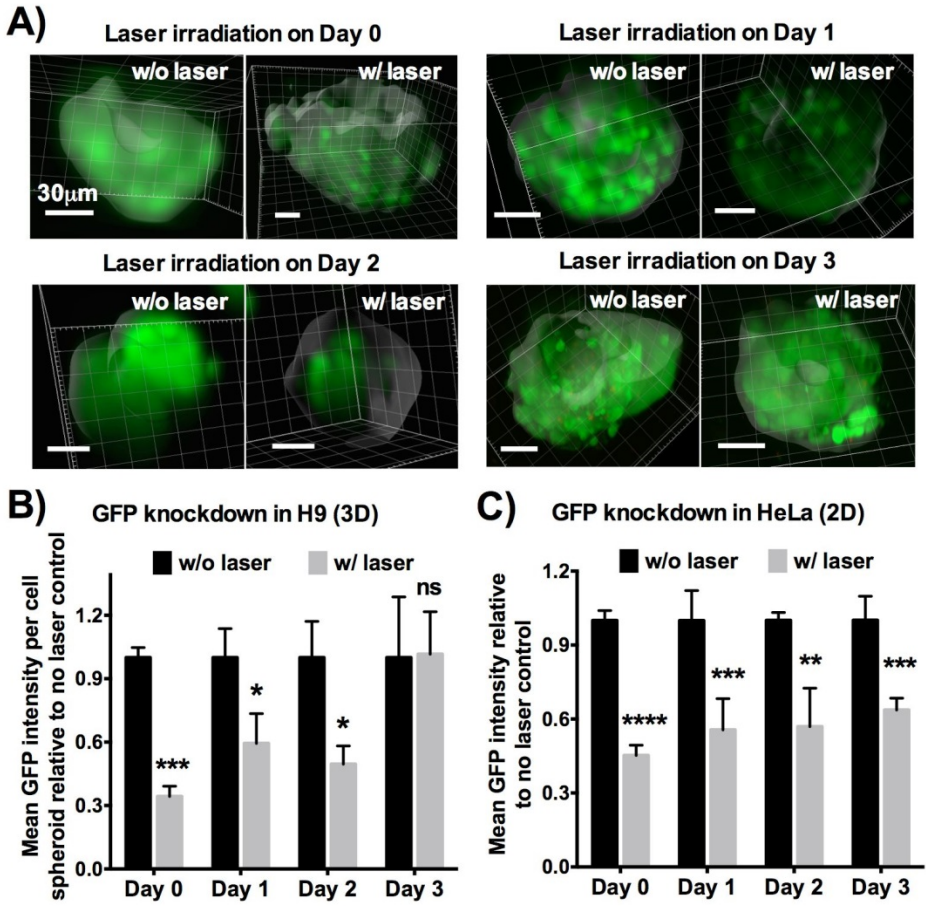

Figure IV-12. siRNA-loaded nanoparticles show longer lifetimes in HeLa cells than hESC H9 cells after the cellular uptake. Fluorescence imaging of Quasar570 (red, labeled on HGN-siRNA) in A) 3D-cultured H9 spheroids (grey for cell outline) and B) 2D-cultured HeLa cells 2 hours (Day 0), 1 day, 2 days and 3 days post nanoparticles incubation. siRNA signal in 3D-cultured H9 cells drops dramatically 2 days after particle incubation, while the drop in HeLa cells is comparatively less. The increase of fluorescent signal (brighter and diffuse) in both H9 cells and HeLa cells 1 day post HGNs internalization could be due to the displacement of thiolated siRNA on gold surface by reducers in cells like glutathione (GSH).

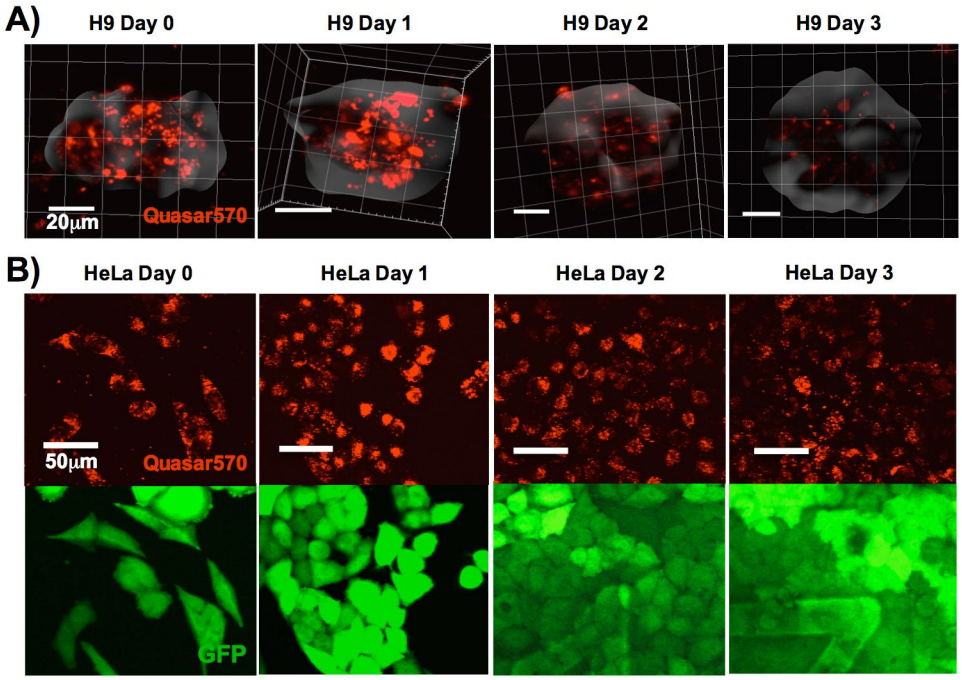

Figure IV-13. siRNA molecules carried by HGNs in HeLa cells for 3 days retain the gene silencing activity upon laser-induced release. siRNA release and GFP knockdown in HeLa cells irradiated with 800 nm laser 2 hours (day 0), 1 day, 2 days and 3 days post nanoparticle incubation. Area in white line: laser irradiated area, Q: Quasar570, BF: Brightfield.

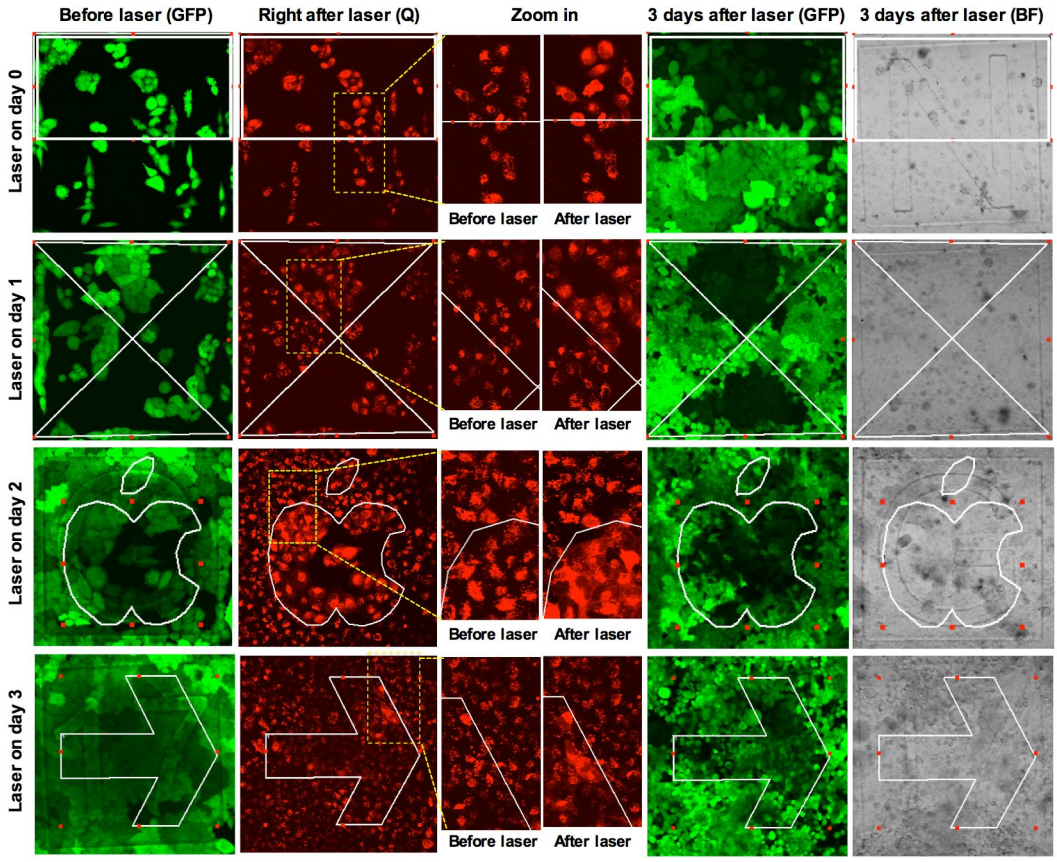

Figure IV-14. siRNA molecules remain intact on HGNs in HEPES buffer at neutral pH and for 3 hours with 1 mM glutathione, whereas longer exposure times and higher glutathione concentrations result in siRNA release at 37°C. The total loading of Quasar570-labeled siRNA on HGNs was determined by a fluorescence-based method after the complete release of the oligonucleotides through KCN etching. The dissociated population of siRNA from HGNs A) over time in HEPES buffer (10 mM HEPES, 1 mM Mg^{2+}, 0.01% Tween-20) at 4°C and B) in HEPES buffer with varying concentrations of GSH for 3 hours or overnight at 37°C.

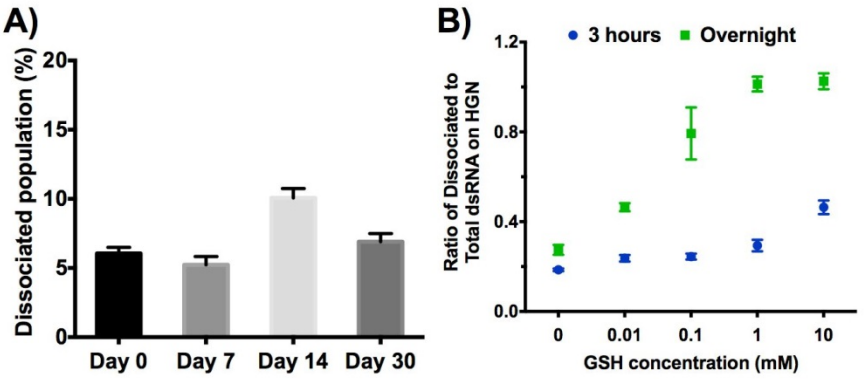

G. Summary

In summary, we have developed a novel approach to control gene regulation in human embryonic stem cells in a 3D matrix with unprecedented spatio-temporal control. The protocol results in efficient siRNA-carrying HGN transfection in three-dimensional multicellular clusters with high viability. A thermoreversible synthetic hydrogel was used as the matrix for hESC 3D culture and NIR light 3D-patterned irradiation operated by a two-photon microscope. We demonstrated three-

dimensional cell resolution siRNA release in selected cells upon laser irradiation, and observed GFP-siRNA activity by tracking the irradiated cells for GFP fluorescence analysis after further culture for 3 days. The *GFP* gene silencing of a subpopulation cells showed distinct patterns of downregulation, suggesting significant cell migration of undifferentiated hESCs within 3D spheroids. This approach is viable for at least two days after HGN treatment, providing a basis for spatio-temporal control. The cargo spectrum of this method can easily be expanded to microRNA and gRNA (for CRISPR/Cas9 mediated gene editing) for both downregulation and up regulation of genes. Thus, the method provides a novel basis for spatio-temporally controlled gene regulation in pluripotent stem cells for *in vitro* organogenesis. Moreover, the two photon excitation approach can also be combined with *in vivo* imaging [38] to become a promising means for investigation of developmental processes *in vivo*.

H. Materials and methods

1. Cell culture on 2D petri dish

hESCs including H9 (passage 60-70, WiCell Research Institute), transduced H9-GFP (passage 65-75) and H9-GFP/mCherry (passage 75-85) were maintained on Matrigel (BD Biosciences) coated plates (BD Falcon) in mTeSR1 medium (Stem Cell Technologies) at 37˚C in 5% CO_2 atmosphere. Cells were passaged by a non-enzymatic manual dissection every 5-7 days. HeLa (ATCC) and HEK293T cells were cultured in DMEM (Hyclone) supplemented with 10% fetal bovine

serum (FBS, Hyclone). 50 μg/mL Normocin (InvivoGen) was supplemented in cell culture media.

2. Generation of stably transfected hESCs and HeLa cells

In order to generate transduced H9-GFP and H9-GFP/mCherry and HeLa-GFP cell lines, lentiviral vectors pLVTHM-scramble (containing an eGFP tag, a gift from Dr. Zach Ma, UCSB) and pLV-mCherry (Addgene #36084) were used. Viral particles were generated using the protocol described in Chapter III-H (2). A viral titer was performed by transducing HeLa cells with several different dilutions of isolated virus. HeLa cells with the best transfection efficiency from virus containing pLVTHM-scramble vectors were passaged for 3 times and freeze-stocked as stable HeLa-GFP cell line.

Passage 54-56 H9 cells (for pLVTHM-scramble vector transfection) or Passage 64-66 H9-GFP cells (for pLV-mcherry vector transfection) were dissociated to cell aggregates (~20 cells per aggregate) using cell dissociation buffer (CDB, Invitrogen) and cultured on Matrigel-coated 6-well plates for 24 hours. The next day fresh medium containing concentrated virus titrated from 1:1 to 10:1 (virus to cell ratio) and 0.6 μg/mL polybrene (Millipore) was added and incubated for another 24 hours. Seven days post transduction, cell colonies were fluorescence-imaged for GFP and mCherry expression. For generating stable H9-GFP and H9-GFP/mCherry cells with high and homogeneous fluorescent protein expression, colonies were manually screened for continuous 3 passages according to the fluorescence imaging.

3. hESC culture in a 3D thermoreversible hydrogel

Each well of 2D-cultured hESCs on 6-well plates were dissociated by incubating with 500 μL PBS (Ca^{2+} and Mg^{2+} free, Invitrogen #10010-023) at 37˚C in a 5% CO_2 atmosphere for 10 minutes followed by manual dissection to suspend the cells. The suspended cell aggregate solution was added to 1 mL mTeSR1 and pipetted gently 10-15 times with a P1000 pipette to further decrease the size of the cell aggregates (~most optimal with 5-10 cells per aggregate). Thereafter, ~4×10^5 cells in single cell or small cell aggregates were mixed with 200 μL PNIPAAm-PEG (Mebiol Thermoreversible Hydrogel, Cosmo Bio) dissolved in E8 medium (Stem Cell Technologies) at 4˚C using a positive-displacement pipette (Microman M250, Gilson).

100 μL of homogenized cell solution was then transferred onto the grid area of an ice-chilled petri dish (μ-$Dish^{35mm}$ Grid-500, Ibidi) to cover the whole surface as a thin layer of liquid (~100-150 μm), followed by the incubation at 37˚C for 5 minutes to solidify the hydrogel. 3 mL of warm E8 medium containing 10 μM ROCK inhibitor was then added on top of the hydrogel and refreshed every day during the subsequent 3D culture. To collect cells from 3D hydrogel after a period of culture, 1 mL ice-cold PBS was replaced on the hydrogel layer and incubated at 4˚C for 5 minutes to dissolve the hydrogel, followed by the centrifugation at 145 × g for 3 minutes.

4. Nanoparticle transfection protocol

Nanoparticle preparation protocols including HGN synthesis, siRNA loading and TAT peptide functionalization are described in Chapter II-H (1-3) and Chapter III-H (4). The siRNA sequences (siGFP and siRFP) for *GFP* and *mCherry* gene knockdown are listed in Table IV-1. Cells were transfected with coated particles in suspension prior to hydrogel embedment to achieve efficient internalization of nanoparticles throughout the cell clusters in 3D culture. Cells on 6-well plates were suspended and dissociated into single cells or small cell aggregates using the treatment of Ca^{2+} and Mg^{2+} free PBS as described above. Cells were centrifuged at 145 × g and resuspended in 200 μL particle containing transfection medium (mTeSR1 + 10% FBS + 10 μM ROCK inhibitor + 13 pM HGNs) at ~2×10^6 cells/mL, followed by 37˚C and 5% CO_2 incubation for 2 hours with gentle pipetting of the solution by P1000 pipette for 5 times every 30 minutes. Thereafter, cells were washed by adding 1.2 mL cold PBS and centrifuging at 55 × g for 3 minutes, followed by the resuspension in 200 μL ice-cold PNIPAAm-E8 solution. 100 μL of the cell mixture was transferred to the grid petri dish and solidified at 37˚C for 5 min before the addition of ROCK inhibitor containing medium, as described above.

As an alternative way of particle transfection, dissociated and suspended hESCs from 2D culture were cast in a thin layer of 3D Mebiol gel on grid petri dish as described above, followed by the daily feeding of fresh HGN-containing medium (E8 + 10% FBS + 10 μM ROCK inhibitor + 13 pM HGNs) for 5 days.

For the transfection of 2D-cultured HeLa-GFP cells, ~1 × 10^5 cells were plated on grid petri dish one day in ahead, and the next day fresh medium (DMEM + 10% FBS) containing 6.5 pM HGNs were replaced and incubated at 37˚C in 5% CO_2 for 2 hours. After that, cells were washed twice with fresh medium.

5. Two-photon microscope excitation and imaging

To activate the siRNA function, 2D-cultured HeLa cells and 3D-cultured H9 cells on grid petri dish post HGN transfection were irradiated with a pulsed NIR laser generated by a two-photon microscope (Olympus Fluoview 1000 MPE) with environmental chamber adjusted at 30˚C and 5% CO_2 atmosphere. The two-photon microscope is equipped with a 25 × water immersion objective (numerical aperture 1.05), a mode-locked titanium-sapphire femtosecond (fs) tunable (690-1020 nm) pulsed laser (100 fs pulse duration, 80 MHz repetition rate, MaiTai HP, Newport-Spectra physics), 473 nm / 559 nm / 633 nm laser diodes, a transmitted light detection system, and a scan head controlled by the Fluoview software. The MaiTai laser was tuned to 800 nm at 5% of the maximum power (~2 mW) and exposed to z-stacks (1.4 μm interval) of intended cell(s) through line-by-line scanning (125 KHz) of selected pixels in each z-stack (512 × 512 pixels, 0.331 μm per pixel) at 2 μsec per pixel for 5 repetitions. The specimen was imaged in a single-photon confocal mode with the blue (for GFP) and green (for Quasar570 or mCherry) laser diodes at a scan speed of 80 KHz before and after the exposure to the MaiTai fs laser to compare the fluorescence signal difference caused by the laser treatment.

Cell(s) treated with laser or without laser were relocated after 3 days according to the grid information on the bottom of the petri dish, and imaged in the single-photon confocal mode for GFP, mCherry or Quasar570 fluorescence, as well as brightfield images from the transmitted channel.

6. Image quantification and statistical analysis

3D images obtained from the single-photon confocal mode of the two-photon microscope were analyzed the GFP, mCherry and Quasar570 fluorescence intensity of cellular spheroids using Imaris 8.1 software (Bitplane). The 3D surface of spheroid was modeled according to the brightfield images and the volume was measured as an indication of cell growth. GFP and mCherry fluorescence intensity were averaged by the volume for the comparison of gene silencing effect with and without laser. Images of HeLa cells from 2D culture on petri dish were analyzed the GFP fluorescence intensity using ImageJ software and averaged by the area.

Data with error bars are from at least three replicate experiments and are presented as the mean ± standard deviation (SD). Statistical analyses were done using the statistical package Instat (GraphPad Software), and the means of replicates were evaluated using t-tests.

7. Flow cytometry analysis

Particle internalization efficiency was assayed the fluorescence intensity from the Quasar570 label, using a BD Accuri C6 flow cytometer. The protocol and parameter setup are the same as described in Chapter III-H (7).

To assay for H9 cell stemness features upon laser irradiation in 3D hydrogel, OCT4 and TRA-1-60 protein levels were determined by immunocytochemical (ICC) staining. HGN internalized H9 cells in 3D Mebiol gel were irradiated with 2.4 W/cm^2 pulsed laser for 15 s by the output of a femtosecond Ti:sapphire regenerative amplifier (Spectraphysics Spitfire) with the same set up described in Chapter II-H (7). The laser beam diameter was ~4 mm with the spectral range of 800 ± 6 nm, and the pulse duration was ~130 fs with the repetition rate at 1 KHz. Thereafter, cells were 3D cultured for 3 days, released from the hydrogel to mTeSR1 medium, and seeded on Matrigel-coated 6-well plate. The next day expanded cell colonies on 2D plate were dissociated into single cells using Accutase and fixed using 4% PFA in PBS (4˚C, 20 minutes). OCT4 and TRA-1-60 ICC staining protocols are described in Chapter III-H (7). Stained cells in 200 μL PBS were injected into flow cytometer for analysis.

8. hESC cell viability assay

H9 cells on 2D plate were washed twice with cold PBS, incubated with 1% crystal violet (Sigma-Aldrich) solution in PBS for 10 minutes, and washed four times with PBS. The wells were imaged by a digital camera (Samsung Galaxy S4).

9. Fluorescence-based siRNA coating assay

Quassar570-labeled siRNA on HGNs were quantified by a fluorescence-based assay. The siRNA-coated HGNs were etched by KCN to totally release the oligonucleotides (*Caution: KCN should not be exposed to acidic conditions due to*

cyanide gas evolution; prepare all solutions in 0.1 M NaOH). The standard linear calibration curve was made between Quasar570-labeled RNA concentration and fluorescence intensity in solution detected from a Tecan infinite 200 plate reader. The fluorescence signal in solution released from HGNs over time or by KCN etching was converted to RNA concentration using the calibration curve.

I. Appendix

Table IV-1. Oligonucleotides used.

Modified Oligos	5'	Sequence (5' to 3')	3'
siGFP sense	Thiol-PEG18	ACCCUGAAGUUCAUCUGCACCACdCdG	NH_2
siRFP sense	Thiol-PEG18	AGUGGGAGCGCGUGAUGAAUU	NH_2
siGFP anti-sense	Quasar570	CGGUGGUGCAGAUGAACUUCAGGGUCA	-
siRFP anti-sense	-	U-MeOU-CAUCACGCGCUCCCACUUU	-

J. References

1. Sasai, Y., *Cytosystems dynamics in self-organization of tissue architecture.* Nature, 2013. **493**(7432): p. 318-26.
2. Gjorevski, N., A. Ranga, and M.P. Lutolf, *Bioengineering approaches to guide stem cell-based organogenesis.* Development, 2014. **141**(9): p. 1794-804.
3. Carvalho-de-Souza, J.L., et al., *Photosensitivity of Neurons Enabled by Cell-Targeted Gold Nanoparticles.* Neuron, 2015. **86**(1): p. 207-217.
4. McGuigan, A.P. and S. Javaherian, *Tissue Patterning: Translating Design Principles from In Vivo to In Vitro.* Annu Rev Biomed Eng, 2016. **18**: p. 1-24.
5. Aday, S., et al., *Stem Cell-Based Human Blood-Brain Barrier Models for Drug Discovery and Delivery.* Trends Biotechnol, 2016.
6. Sasai, Y., *Next-Generation Regenerative Medicine: Organogenesis from Stem Cells in 3D Culture.* Cell Stem Cell, 2013. **12**(5): p. 520-530.
7. Nakao, K., et al., *The development of a bioengineered organ germ method.* Nature Methods, 2007. **4**(3): p. 227-230.
8. Spence, J.R., et al., *Directed differentiation of human pluripotent stem cells into intestinal tissue in vitro.* Nature, 2011. **470**(7332): p. 105-U120.
9. Eiraku, M., et al., *Self-organizing optic-cup morphogenesis in three-dimensional culture.* Nature, 2011. **472**(7341): p. 51-6.
10. Suga, H., et al., *Self-formation of functional adenohypophysis in three-dimensional culture.* Nature, 2011. **480**(7375): p. 57-62.
11. Nakano, T., et al., *Self-Formation of Optic Cups and Storable Stratified Neural Retina from Human ESCs.* Cell Stem Cell, 2012. **10**(6): p. 771-785.
12. Kolind, K., et al., *Guidance of stem cell fate on 2D patterned surfaces.* Biomaterials, 2012. **33**(28): p. 6626-6633.
13. Fujie, T., et al., *Spatial coordination of cell orientation directed by nanoribbon sheets.* Biomaterials, 2015. **53**: p. 86-94.
14. Ahn, E.H., et al., *Spatial control of adult stem cell fate using nanotopographic cues.* Biomaterials, 2014. **35**(8): p. 2401-2410.
15. Brieke, C., et al., *Light-controlled tools.* Angew Chem Int Ed Engl, 2012. **51**(34): p. 8446-76.
16. Tischer, D. and O.D. Weiner, *Illuminating cell signalling with optogenetic tools.* Nat Rev Mol Cell Biol, 2014. **15**(8): p. 551-8.
17. Deiters, A., *Light activation as a method of regulating and studying gene expression.* Current Opinion in Chemical Biology, 2009. **13**(5-6): p. 678-686.
18. Hemphill, J., et al., *Optical Control of CRISPR/Cas9 Gene Editing.* Journal of the American Chemical Society, 2015. **137**(17): p. 5642-5645.
19. Polstein, L.R. and C.A. Gersbach, *A light-inducible CRISPR-Cas9 system for control of endogenous gene activation.* Nature Chemical Biology, 2015. **11**(3): p. 198-U179.

20. Nihongaki, Y., et al., *Photoactivatable CRISPR-Cas9 for optogenetic genome editing.* Nature Biotechnology, 2015. **33**(7): p. 755-760.
21. Polstein, L.R. and C.A. Gersbach, *Light-inducible spatiotemporal control of gene activation by customizable zinc finger transcription factors.* J Am Chem Soc, 2012. **134**(40): p. 16480-3.
22. Gomez, E.J., et al., *Light-Activated Nuclear Translocation of Adeno-Associated Virus Nanoparticles Using Phytochrome B for Enhanced, Tunable, and Spatially Programmable Gene Delivery.* Acs Nano, 2016. **10**(1): p. 225-237.
23. Hemphill, J., et al., *Conditional Control of Alternative Splicing through Light-Triggered Splice-Switching Oligonucleotides.* Journal of the American Chemical Society, 2015. **137**(10): p. 3656-3662.
24. Mikat, V. and A. Heckel, *Light-dependent RNA interference with nucleobase-caged siRNAs.* Rna-a Publication of the Rna Society, 2007. **13**(12): p. 2341-2347.
25. Huynh, C.T., et al., *Photocleavable Hydrogels for Light-Triggered siRNA Release.* Adv Healthc Mater, 2016. **5**(3): p. 305-10.
26. Kohman, R.E., et al., *Light-Triggered Release of Bioactive Molecules from DNA Nanostructures.* Nano Letters, 2016.
27. Lee, S.Y., et al., *In vivo sub-femtoliter resolution photoacoustic microscopy with higher frame rates.* Scientific Reports, 2015. **5**: p. 15421.
28. Weissleder, R., *A clearer vision for in vivo imaging.* Nat Biotechnol, 2001. **19**(4): p. 316-7.
29. Timko, B.P. and D.S. Kohane, *Prospects for near-infrared technology in remotely triggered drug delivery.* Expert Opinion on Drug Delivery, 2014. **11**(11): p. 1681-1685.
30. Huang, X., et al., *Modular Plasmonic Nanocarriers for Efficient and Targeted Delivery of Cancer-Therapeutic siRNA.* Nano Lett, 2014. **14**(4): p. 2046-51.
31. Braun, G.B., et al., *Laser-Activated Gene Silencing via Gold Nanoshell-siRNA Conjugates.* ACS Nano, 2009. **3**(7): p. 2007-15.
32. Morales, D.P., et al., *Targeted intracellular delivery of proteins with spatial and temporal control.* Mol Pharm, 2015. **12**(2): p. 600-9.
33. Huang, X., et al., *Light-activated RNA interference in human embryonic stem cells.* Biomaterials, 2015. **63**: p. 70-79.
34. Lei, Y. and D.V. Schaffer, *A fully defined and scalable 3D culture system for human pluripotent stem cell expansion and differentiation.* Proc Natl Acad Sci U S A, 2013. **110**(52): p. E5039-48.
35. Huang, K.Y., et al., *Size-Dependent Localization and Penetration of Ultrasmall Gold Nanoparticles in Cancer Cells, Multicellular Spheroids, and Tumors in Vivo.* Acs Nano, 2012. **6**(5): p. 4483-4493.
36. Javaherian, S., et al., *Design principles for generating robust gene expression patterns in dynamic engineered tissues.* Integr Biol (Camb), 2013. **5**(3): p. 578-89.

37. De Ugarte, D.A., et al., *Comparison of multi-lineage cells from human adipose tissue and bone marrow.* Cells Tissues Organs, 2003. **174**(3): p. 101-109.
38. Pineda, C.M., et al., *Intravital imaging of hair follicle regeneration in the mouse.* Nature Protocols, 2015. **10**(7): p. 1116-1130.

V. Modular surface functionalization for maximized siRNA delivery

A. Abstract

We describe a universal surface module and several functionalization rules for the maximized delivery of short nucleic acids (herein siRNA) in diverse human cells using gold nanocarriers. Streptavidin is devised as a handle to assemble biotinylated cell penetrating peptides (e.g., TAT) as well as an insulator from the dense negative charge of RNA. However, direct linking of streptavidin to functional siRNA inhibits its bioactivity. Our approach then evolves to the orthogonal assembly of two RNA strands: one with biotin modification for cell targeting and penetration (scaffold RNA); the other without biotin as functional RNA (siRNA). Single-stranded RNA is advantageous for densely surface-packing due to their high flexibility, but later a double-stranded format is preferred to best assemble the targeting peptide for cellular uptake and siRNA delivery. This orthogonal approach on the delivery of short oligonucleotides, together with novel surface functionalization rules discovered here, should be suggestive for nano-medicinal research and applications.

B. Introduction

Short oligonucleotides with ~20-60 nucleotides including siRNA, miRNA, antisense DNA and gRNA (for CRISPR) are powerful tools for gene regulation in many applications such as basic cell research, cancer therapy and regenerative

medicine [1-6]. The cellular delivery of these biologically unstable, high molecular weight, and negative-charged molecules remains a significant challenge [7, 8]. Diverse nanoparticles, including gold nanoparticles, have been used to assemble and stabilize siRNA from degradation and enhance cellular delivery [9-14]. Thiolated oligonucleotides have been self-assembled on the nanoparticle surface through the formation of quasi-covalent gold-thiol bonds [15-18]. The introduction of plasmonic gold nanoparticles with strong near-infrared light absorption, like nanorods, nanostars, and nanoshells, facilitates the release of siRNA after cellular uptake with high efficiency and remote light control [17, 19-24]. Importantly, the delivery of RNA cargoes can be easily attained at single cell-level resolution using a two-photon microscope without any detectable impact on cellular viability.

Critical obstacles to the use of siRNA in a variety of human cells, including primary cells and embryonic stem cells, through nanoparticle platforms include efficient uptake as well as endosomal release [25]. The trans-activating transcriptional activator (TAT) peptide is highly efficient at guiding extracellular molecules to many cell lines [23, 26-28], but it is rarely used on nucleic acid coated nanoparticles [29] due to aggregation issues related to the polyelectrolyte charge interactions. In prior work with HGNs, we introduced streptavidin [30-33] as a relatively large and more neutrally charged spacer between the nucleic acid layer and TAT peptide outer layer [19]. The resulting nanoparticles formed a stable colloid and showed high penetration efficiency in a wide range of human

Figure V-1. Modular design of hollow gold nanoshells (HGN) for siRNA delivery.

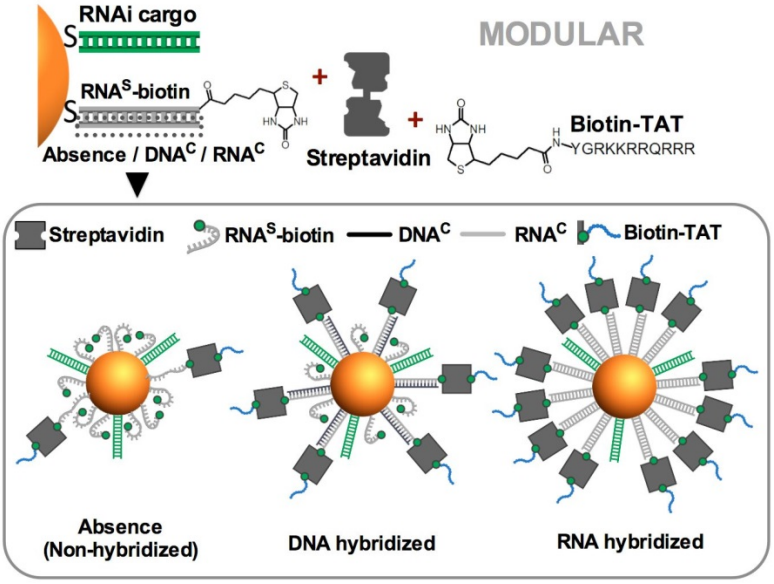

embryonic stem cells [19]. Herein, we devised a strategy to separately control the streptavidin coverage for efficient cell penetration while retaining a robust method to down regulate target genes, based on the mixed-assembly of a biotinylated thiol-RNA and a non-biotinylated thiol-RNA on HGNs (Figure V-1). Importantly, the biotin-modified RNA assembles streptavidin noticeably better in the duplex form, leading to dramatically higher cell penetration efficiencies. Furthermore, using RNA for surface hybridization leads to improved efficiencies when compared to DNA (Figure V-1). The relationships between surface modifications and cellular performance of the materials described here may be important for the use of nanoparticles for the cellular delivery of nucleic acids.

C. Streptavidin coverage determines particle internalization efficiency

We previously developed a strategy to deliver RNA-coated HGNs [17] into cells, by incorporating a streptavidin layer attached with the cell penetrating peptide TAT (YGRKKRRQRRR). TAT is well known for its efficient internalization into a broad range of mammalian cells, including cancer cells and stem cells [19]. Streptavidin acts as a charge insulator between the RNA and TAT peptide layer, reducing potential aggregation while serving as a convenient attachment site for a biotinylated peptide. This strategy generated HGNs in a stable colloid format with efficient cell penetration properties and laser-induced release of RNA caused knockdown of a reporter gene in the cells [19].

Here we find that using a biotin pre-modified RNA strand leads to higher loading of streptavidin (Figure V-2A), while bypassing the surface biotin functionalization step; this improves the cell internalization in both cancer (HeLa) and stem (hESC H9) cells (Figure V-2B). The relative streptavidin coverage level was estimated by a fluorescence-based assay of Oregon Green 488-labeled neutravidin due to their similar isoelectric point and binding affinity [34]. Varying the fraction of biotin-modified anchoring RNA (RNA^S-biotin) versus biotin-free RNA (RNA^S) (Table V-1) during the assembly step linearly determined the streptavidin coverage level (Figure V-2A), indicating that biotin modification is important for optimizing streptavidin loading. Dark field imaging of HRSTs in both HeLa and H9 cells showed that the amount of HRSTs in each cell improved with

Figure V-2. Increasing level of streptavidin coverage yields enhancing efficiency of cellular internalization of TAT peptide-coated HGN-siRNA (HRST). A) Levels of streptavidin coverage (I - IV) on HGNs obtained by varying input ratios RNA^S to RNA^S-biotin at the anchoring RNA assembly step. B) Dark-field images of HeLa cells (top panel, cell confluence ~100%) and hESC H9 cells (bottom panel) internalized with HRSTs of different levels of streptavidin coverage. Golden puncta: HRST; Purple: nuclei by Hoechst staining.

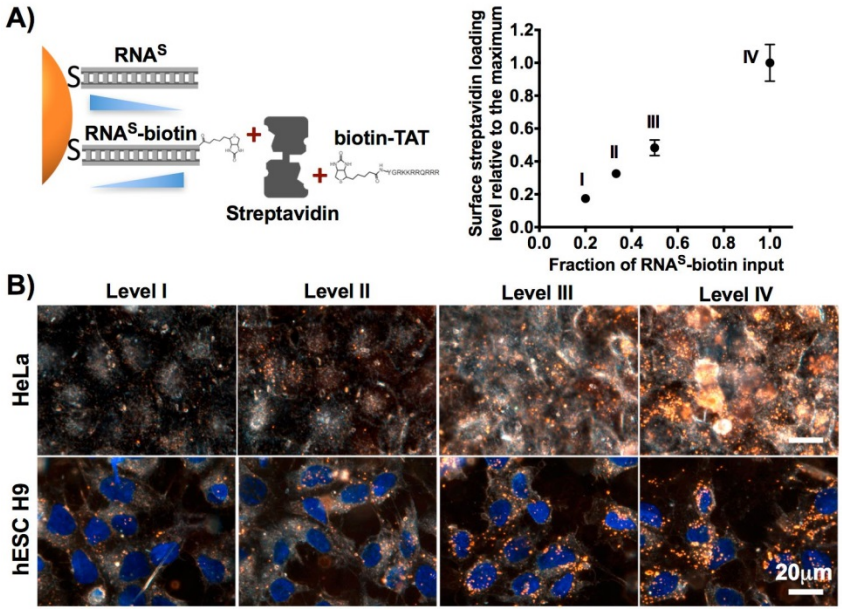

the increase of streptavidin coverage (Figure V-2B). This supports the use of streptavidin as a modular connector for TAT peptides that can be optimized to deliver functional RNA into cells.

D. Direct linkage of streptavidin blocks siRNA function

Figure V-3. The fraction of biotinylated siRFP versus unmodified siRFP on HRSTs is optimized for the best gene silencing effect. Fluorescence images are taken for RFP-expressing HeLa cells three days after HRSTs internalization and NIR laser irradiation. HRSTs are treated with different input ratios of RFP sense strand (RFP^S) to biotinylated RFP sense strand (RFP^S-biotin) (1:0, 2:1, 1:1 and 0:1) for anchoring strand assembly. Cell confluence in images are ~100%.

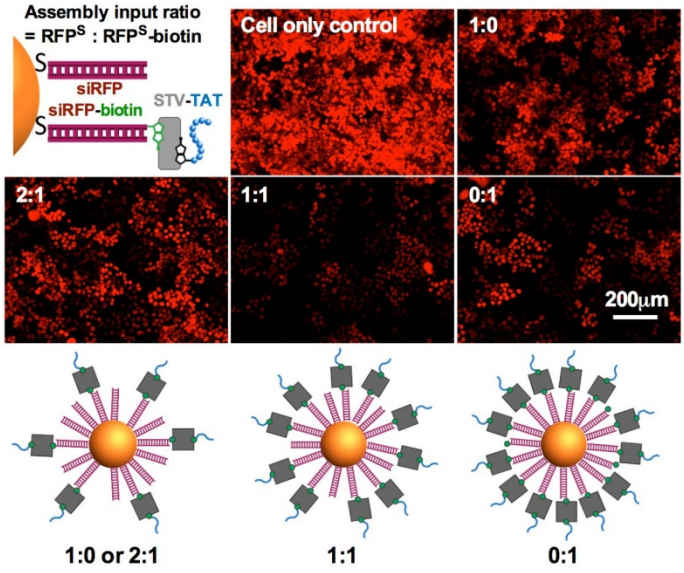

Different ratios of the biotinylated sense strand (RFP^S-biotin, Table V-1) to biotin-free sense strand (RFP^S) for RFP-siRNA (siRFP) were assembled on HGNs followed by the hybridization of the anti-sense strand (RFP^{AS}) to form siRNA duplexes (Figure V-3). HRSTs thus generated with varying levels of streptavidin coverage were tested for *RFP (mCherry)* gene silencing in transduced HeLa cells from light-activated siRNA delivery (Figure V-3). Interestingly, the best *RFP* gene

knockdown did not occur for the condition of HRSTs with the highest streptavidin coverage (non-biotin : biotin, 0:1) (Figure V-3). Instead, at a fixed amount of RFP-siRNA loading, the condition with moderate coverage of streptavidin on HRSTs (1:1) yielded the best gene knockdown (Figure V-3). We hypothesized that streptavidin may block the RNAi machinery from accessing the siRNA duplexes which are directly connected to streptavidin, even after the release from the HGN surface. However, we still observed gene knockdown activity using HRSTs with the maximum streptavidin coverage (Figure V-3, 0:1), suggesting either steric effects are incomplete or not all siRNA-biotin carry streptavidin.

Figure V-4. siRNA sequences (siGFP and siRFP) designed for GFP and RFP silencing specifically target respective gene without interfering each other in GFP and RFP co-transduced HeLa cells. Thus, siGFP sequence is also used as non-sense oligonucleotide strand for RFP.

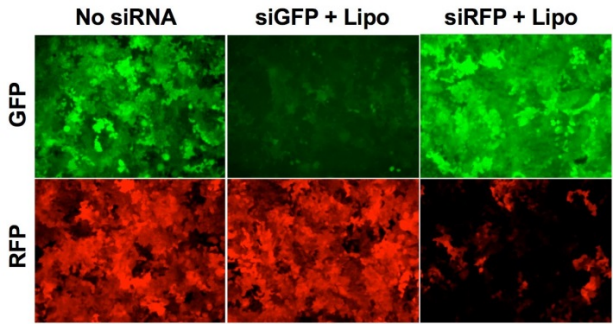

To investigate this further, we mixed biotin-free non-sense double strand RNA (non-sense dsRNA to the *RFP* gene, Figure V-4) with biotin-modified siRFP, so that most or all of the siRFP on surface would carry streptavidin (Figure V-5, 1:1 and 1:5). As expected, we did not observe any silencing activity from this treatment

Figure V-5. The direct linking of streptavidin and TAT peptide to siRNA prevents RNAi knockdown. Fluorescence imaging of RFP-expressing HeLa cells three days after the internalization of HRSTs and NIR laser irradiation. HRSTs are treated with different input ratios of from different input ratios of nsRNA^{S} to RFP^{S}-biotin strand (1:1 and 1:5) during the assembly step. Cell confluence in images are all ~100%.

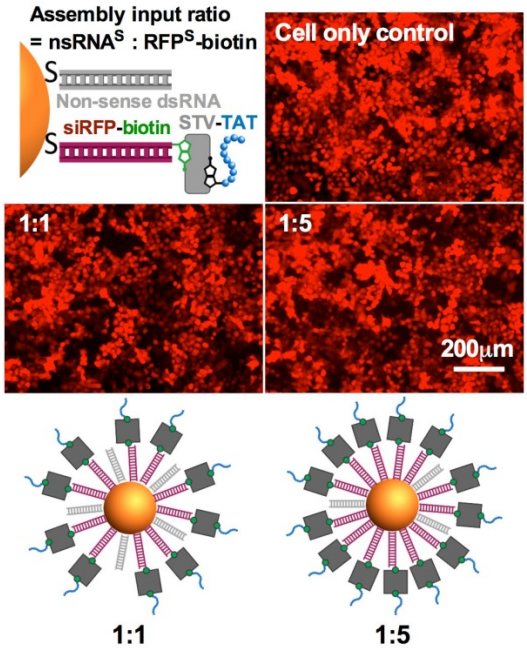

(Figure V-5). This result demonstrates that the siRNA activity is blocked by direct conjugation to streptavidin. Thus, we conclude that the best siRNA delivery strategy is the collective effect from both unmodified siRNA loading and biotinylated RNA for streptavidin attachment which can be easily optimized for a specific target gene and cell line.

E. Optimal cell internalization requires a hybridized RNA-biotin handle

Figure V-6. The modular handle for streptavidin attaching requires to be hybridized for maximum cell penetration and siRNA activity. A) Schematic of the modular-designed HRSTs with the non-hybridized (NH, left) and RNA^C-hybridized (right) cell internalization moiety (RNA^S-biotin). RNA^S-biotin and sense strand for GFP-siRNA (siGFP) are assembled on HGNs with the input ratio of 5:1. B) Dark-field images of HeLa cells (top panel) and hESC H9 cells (bottom panel) internalized with the two types of HRSTs (Golden puncta: HRSTs, Blue: Nuclei by Hoechst staining). C) Flow cytometry quantification of GFP level in GFP-expressing HeLa cells three days after the internalization of the two types of HRSTs and laser irradiation. **, $p < 0.01$; NS, not significant.

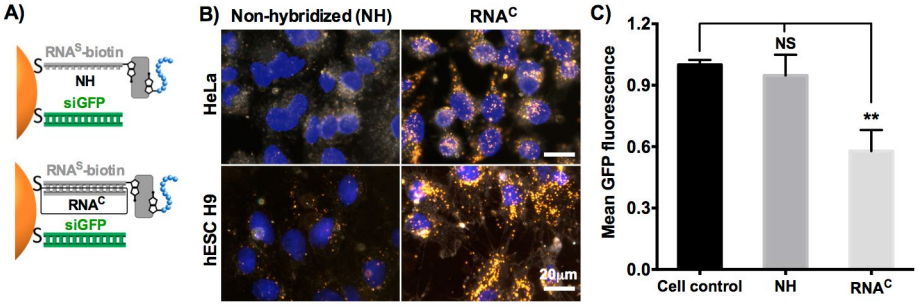

To increase the ease and versatility of the delivery to other sequences of siRNA or functional small nucleic acids, we designed a modular surface arrangement (Figure V-6A). A universal nucleic acid handle with biotin modification for streptavidin and peptide attachment (RNA^S-biotin) shares the nanoparticle surface with a functional RNA (siGFP) without biotin modification. The sequence of each is unique to allow separate examination of each part with

regard to cell internalization and gene regulation efficiency. Importantly, HRSTs with non-hybridized RNA^S-biotin strand showed much lower penetration in both HeLa cells and hESC H9 cells (Figure V-6B). Because the gene (*GFP*) knockdown effect was increased in line with the degree of cell internalization (Figure V-6C), there is a modular independence between the biotin module for cellular uptake and the siGFP module that dictates gene regulation.

Figure V-7. Relative streptavidin coverage level of HRSTs with the modular handle hybridized by RNA^C, compared to non-hybridized (NH). Relative streptavidin coverage level is estimated by a fluorescence-based quantification of Oregon Green 488-labeled neutravidin.

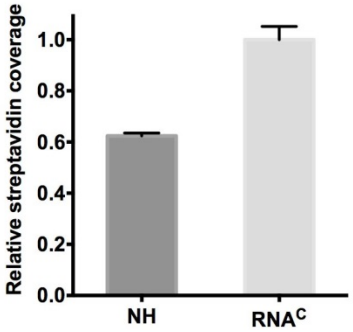

HRSTs with non-hybridized RNA^S-biotin show only 60% of the streptavidin levels compared to those particles which have been hybridized with RNA (Figure V-7), suggesting inefficient presentation of biotin by the streptavidin binding RNA module. This is likely due to the high flexibility of single strand RNA, which can even cause cross-linking between RNA^S-biotin strands by streptavidin. However, directly coating HGNs with nucleic acid duplexes results in instability and loading difficulties [35]. Notably, our modular assembly involves the

deposition of single stranded RNA to maximize attachment density on the surface, followed by hybridization, yielding rigid double strands that presented biotin more efficiently for streptavidin and TAT peptide coating (see Figure V-6).

F. RNA hybridizes more efficiently than DNA on HGN surfaces

Figure V-8. RNA more than doubles the efficiency of DNA hybridization to the modular handle for effective cellular uptake. A), B) Dark field image quantification of HeLa and H9 cell internalization of HRSTs with the modular handle hybridized by DNA^C or RNA^C. C) Flow cytometry quantification of GFP expression level in GFP-expressing HeLa cells three days after the internalization of HRSTs (DNA^C and RNA^C) and laser irradiation. **, $p < 0.01$; ***, $p < 0.001$; NS, not significant.

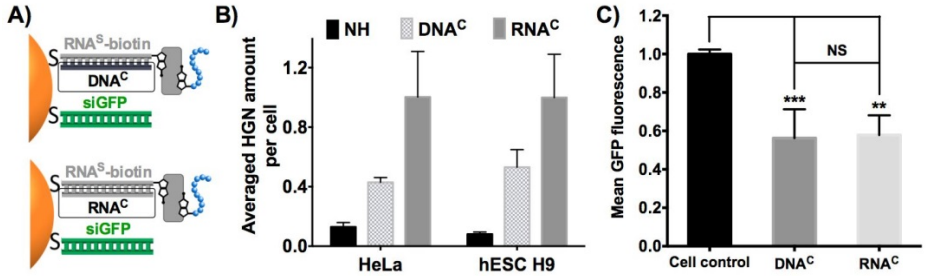

The replacement of complementary DNA for hybridizing to the scaffold RNA handle (RNA^S-biotin) would reduce costs of this approach. However, we noticed that the hybridization with complementary DNA (DNA^C) yielded only half of the cell penetration efficiency compared to those hybridized with RNA^C at the same concentration, observed for both HeLa and H9 cells (Figure V-8A,B). Interestingly, RNA^C did not show more *GFP* gene knockdown effects than with

DNA^C (Figure V-8C), presumably, due to the saturated silencing of *GFP* gene in HeLa cells at the siRNA dosage. The improved cellular delivery of functional RNA we explored here, using double stranded RNA as a scaffold for the streptavidin targeting moiety, would nevertheless aid future gene regulation applications that require high doses of functional RNA.

Figure V-9. Comparison of duplex number per particle for HGNs assembled and hybridized by oligonucleotides of different types (DNA or RNA) with identical sequences for 0.5 hour or 3 hours.

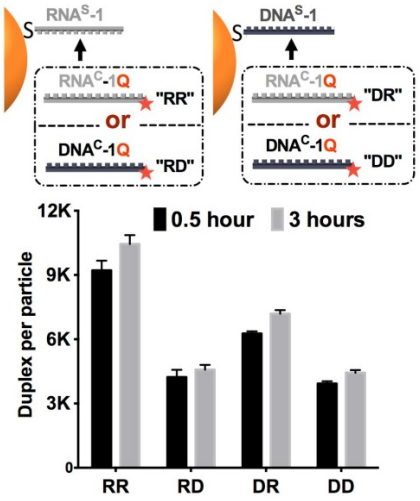

To explore the difference in the hybridization efficiency between DNA and RNA on the gold nanoparticle surface, we assembled thiolated DNA and RNA of identical sequence (T to U) (Table V-1), then hybridized with DNA and RNA of complementary sequence (Figure V-9). Fluorescence-based quantification after KCN etching showed that the amount of RNA-RNA (RR) duplex was more than double that of the DNA-DNA (DD) duplex and RNA-DNA duplex (thiolated RNA and complementary DNA, RD) (Figure V-9). We observed the same trend as we

extended the hybridization incubation time from 30 minutes to 3 hours (Figure V-9), indicating that this discrepancy was not due to differing hybridization kinetics. Computational algorithms (DINAMelt Web Server) show that RR has a delta G of -67.0 kcal/mol and T_m of 89.6^{o}C, wheras for DD are -49.6 kcal/mol and 81.0^{o}C. Previous experimental studies also report that RR is thermodynamically more stable than DD or RD in bulk solution [36-39], as the A-form conformation of RR and RD have modestly better base-stacking energy than the B-form DD. However, given that HGN surface is densely decorated with oligonucleotides [17], these differences are affected by steric, electrostatic hindrance and conformational restriction of the surface-tethered strands [40]. The greater flexibility of RNA relative to DNA may also contribute to the higher efficiency of RNA hybridization and assembly on surface.

The modular design utilized two types of RNA strands of different sequence: one must be hybridized with complementary RNA to form the functional siRNA, while the other strand, carrying biotin, can be hybridized by complementary DNA or RNA to control the attachment of streptavidin. Using the mixed modular RNA surface, we found that the amount of complementary DNA that hybridized to one sequence was less when the other sequence had formed RNA/RNA duplexes (Figure V-10). The opposite condition, when DNA was added at high concentration (up to 150 μM) did not decrease the hybridization efficiency of complementary RNA (Figure V-10). This suggests that RNA strands are better hybridized on highly compact HGN surfaces.

Figure V-10. RNA strands have advantageous hybridization in highly compact HGN surface compared to a relatively low affinity of the DNA strands. A), B) Amount of Q-labeled duplex number per particle from different hybridization strategies shown in the cartoon when RNA^S-1 and RNA^S-2 are co-assembled on HGNs with the input at 2.25 μM and 0.75 μM, respectively. **, p < 0.01; ***, p < 0.001; ns, not significant.

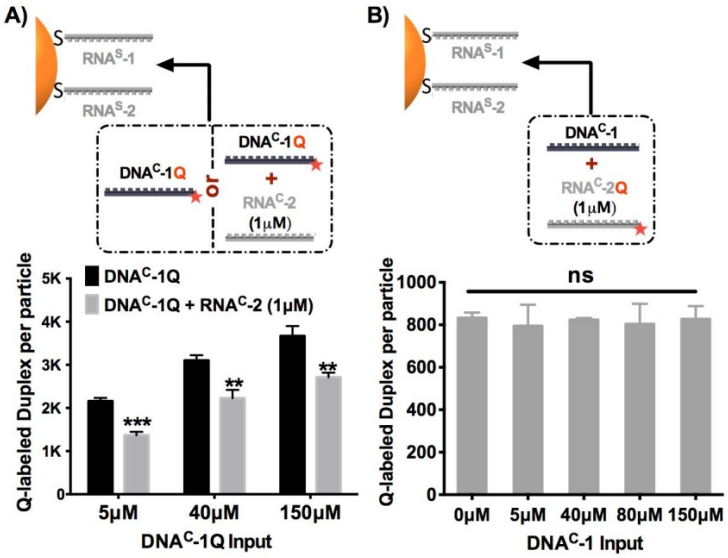

G. Summary

We have developed a modular surface design using gold nanocarriers for the efficient delivery of functional short oligonucleotides (here siRNA) applicable to a broad spectrum of cell lines (from cancer to stem cells). Streptavidin is introduced as a universal handle for cell penetrating peptide coating and the insulator between negative-charged oligonucleotides and positive-charged TAT to avoid nanoparticle aggregation. To avoid the steric inhibition of direct-linked streptavidin to RNA interfering process, HGN surface loaded RNAs are designed into two categories:

one for functional small interfering RNAs or other short nucleic acids; the other as scaffolds for presenting the biotin to capture streptavidin and the TAT peptide. RNA is an ideal choice as surface scaffold, since single strand RNA with high flexibility can be densely packed on gold surface through a low-pH induced self-assembly method and later be hybridized as high affinity duplexes for more efficient biotin modification presentation than for single stranded RNA. The effective presentation of biotin followed by adequate streptavidin loading yielded particles with an optimal level of cell penetration. Furthermore, we found that RNA hybridization capacity on HGNs was approximately double of that for DNA hybridization, attributed to greater stability of the RNA/RNA duplex. Altogether, this work successfully builds a coherent framework between modular nucleic acid and targeting peptide surface chemistries. Optimized assemblies can provide important insights, applicable to future high-density structures built from functional short oligonucleotides, for example, to deliver gRNA for CRISPR, miRNA, anti-sense DNA, important to emerging areas in genetic control and bioengineering.

H. Materials and methods

1. Cell culture

HeLa and HEK293T cells (ATCC) were cultured in DMEM (Hyclone) supplemented with 10% fetal bovine serum (FBS, Hyclone) at 37 ˚C in 5% CO2 atmosphere. hESC H9 (passage 60-70, WiCell Research Institute) were maintained on Matrigel (BD Biosciences) coated plates (BD Falcon) in mTeSR1 medium

(Stem Cell Technologies). 50 μg/mL Normocin (InvivoGen) was supplemented in cell culture medium.

2. Generation of stably transduced HeLa cells

Stably transduced HeLa cells were generated through the lentiviral transfection method. Vectors including pLVTHM-scramble (containing an eGFP tag, a gift from Dr. Zach Ma, UCSB) and pLV-mCherry (Addgene #36084) were used to transduce *GFP* and *RFP* gene to HeLa cells respectively. Viral particles were generated using the protocol described in Chapter III-H (2). HeLa cells with the best transfection efficiency were passaged for 3 times and sorted through FACS (BD FACS Aria 2 with a 100 μm nozzle) to collect cells with high and homogenous expression of GFP or RFP protein. Stably transduced cells were freeze-stocked and used for HGN-mediated siRNA delivery tests.

3. Nanoparticle preparation, transfection and laser irradiation

Nanoparticle preparation protocols including HGN synthesis, siRNA loading and TAT peptide functionalization are described in Chapter II-H (1-3) and Chapter III-H (4). The siRNA sequences (siGFP and siRFP) for *GFP* and *mCherry* gene knockdown are listed in Table V-1. For HGNs assembled with biotin pre-modified oligonucleotides, the step of amine group functionalization using NHS-PEG_4-Biotin described in Chapter III-H (4) was skipped.

HeLa cells on a 6-well plate were harvested by the incubation with 500 μL non-enzymatic cell dissociation buffer (CDB, Invitrogen) at 37˚C in 5% CO_2

atmosphere for 10-15 minutes. Cells were centrifuged at 1000×g for 10 min and re-suspended in DMEM medium (with 10% FBS supplemented) to a final concentration of 1×10^6 cells/mL. 6.5 pM of coated HGN were added to 200 μL of cell suspension and incubated in 1.5 mL Eppendorf tubes at RT for 2 hours on a rotator. Free nanoparticles were washed out by adding 1.2 mL DPBS (Invitrogen) and centrifuging at 55×g for 5 minutes. 45 μL DPBS was mixed with the cell pellet and irradiated for 15 s under pulsed NIR laser (2.4 W/cm^2) output from the femtosecond (fs) Ti:sapphire regenerative amplifier (Spectraphysics Spitfire) with the setup described in Chapter II-H (8). Cells were then further cultured for 3 days in 12-well plates at 37^oC in 5% CO_2 atmosphere, and assessed the fluorescence protein expression (GFP and RFP) through microscope imaging (Olympus IX70 inverted microscope equipped with a QImaging Retiga-2000R Fast 1394 camera) and flow cytometry (BD Accuri C6).

4. Flow cytometry analysis

Cells on 12-well plates were suspended by incubating with 0.25% trypsin-EDTA (Thermo SCIENTIFIC, #25200) at 37˚C in a 5% CO_2 atmosphere for 5 minutes, and resuspended in cold DPBS at 1×10^6 cells/mL. Cells were then injected into a BD Accuri C6 flow cytometer with a flow rate of 14 μL/min. A gate area was selected from the forward versus side scatter plots, and 10,000 events were collected for each sample.

5. Dark field imaging

HeLa cells on an 8-well chamber glass slide (Lab-Tek II), or hESC H9 cells on a Matrigel-coated 4-well chamber Permanox slide (Lab-Tek #70400), were incubated with 6.5 pM HGNs in DMEM or mTeSR1 medium (with 10% FBS supplemented) at 37 ˚C in 5% CO_2 atmosphere for 2 hours. Following the twice washing by PBS, cells were fixed using 4% paraformaldehyde (VWR International, LLC), and washed again in PBS. Cells were then stained the nuclei by Hoechst 33342 (Sigma-Aldrich) and mounted with Gel/Mount (Electron Microscopy Science). Dark-field scattering images were taken using an Olympus BX51 upright microscope with the protocol described in Chapter III-H (6). Dark field images were quantified the average HGN signals in cells by pixel analysis using ImageJ software.

6. Fluorescence-based quantification of attached molecules

Through a fluorescence-based assay, Quassar570-labeled oligonucleotides (Table V-1) were used to quantify the amount of assembled duplexes on HGNs, and Oregon Green 488-labeled neutravidin was used to estimate the relative level of streptavidin due to the high biochemical similarity between the two. Oregon Green 488-labeled neutravidin was prepared by incubating 5 mg/mL neutravidin (Pierce #31050) with 0.75 mM Oregon Green 488 NHS ester (10 mM in DMSO, Pierce #O6147) in the reaction buffer (1× PBS, 0.75% sodium bicarbonate, 10% glycerol) for 3 hours at RT, followed by the twice dialysis (20 KDa Slide-A-Lyzer, Pierce) in

1× PBS supplemented with 2 mM NaN_3 and filtration (Millipore 0.22 μm #SLGV013SL).

HGNs with fluorescence labels were etched by KCN solution (0.1 M KCN, 1mM $K_3Fe(CN)_6$) to completely release the coated molecules. The standard linear calibration curves were generated between the concentrations of fluorescence-labeled molecules and the corresponding fluorescence intensity detected from a Tecan infinite 200 plate reader. The fluorescence signal in solution released from HGNs by KCN etching was converted to oligonucleotide duplex unit and neutravidin number using the calibration curve.

I. Appendix

Table V-1. Oligonucleotides used.

Oligos	Use	5'	3'	Sequence (5' → 3')
RNA^S	Anchoring strand (Fig. 1)	Thiol-PEG18	NH_2	AGUGGGAGCGCGUGAUGAAUU
RNA^S-biotin	Anchoring strand (Fig. 1,3)		Biotin	
RFP^S	siRFP sense (Fig. 2)		NH_2	
RFP^S-biotin	siRFP-biotin sense (Fig. 2)		Biotin	
RNA^S-2	Anchoring strand (Fig. S8)		NH_2	
RFP^{AS}	siRFP anti-sense (Fig. 2)	-	-	U-MeOU-CAUCACGCGCUCCCACUUU
RNA^C	Complementary to RNA^S-biotin (Fig. 1,3)	-	-	
RNA^C-2	Complementary to RNA^S-2 (Fig. S8)	-	-	
RNA^C-2Q	Complementary to RNA^S-2 (Fig. S8)	Quasar 570	-	
GFP^S	siGFP sense (Fig. 3)	Thiol-PEG18	NH_2	ACCCUGAAGUUCAUCUGCACCACdC dG
$nsRNA^S$	Non-sense to RFP (anchoring) (Fig. 2)			
RNA^S-1	Anchoring strand (Fig. 4, S8)			
GFP^{AS}	siGFP anti-sense (Fig. 3)	-	-	CGGUGGUGCAGAUGAACUUCAGGG UCA
$nsRNA^C$	Non-sense to RFP (complementary) (Fig. 2)	-	-	
RNA^C-1	Complementary to RNA^S-1 (Fig. 4, S8)	-	-	
RNA^C-1Q	Complementary to RNA^S-1 & DNA^S-1 (Fig. 4, S8)	Quasar 570	-	
DNA^S-1	DNA counterpart of RNA^S-1 (Fig. 4, S8)	Thiol-PEG18	NH_2	CGGTGGTGCAGATGAACTTCAGGGT
DNA^C	Complementary to RNA^S-biotin (Fig. 3)	Quasar 570	-	AATTCATCACGCGCTCCCACT
DNA^C-1Q	Complementary to RNA^S-1 & DNA^S-1 (Fig. 4, S8)	Quasar 570	-	CGGTGGTGCAGATGAACTTCAGGGT
DNA^C-1		-	-	

J. References

1. Hemphill, J., et al., *Optical Control of CRISPR/Cas9 Gene Editing.* Journal of the American Chemical Society, 2015. **137**(17): p. 5642-5645.
2. Riboldi, G., et al., *Antisense Oligonucleotide Therapy for the Treatment of C9ORF72 ALS/FTD Diseases.* Molecular Neurobiology, 2014. **50**(3): p. 721-732.
3. Kole, R., A.R. Krainer, and S. Altman, *RNA therapeutics: beyond RNA interference and antisense oligonucleotides.* Nature Reviews Drug Discovery, 2012. **11**(2): p. 125-140.
4. Forbes, D.C. and N.A. Peppas, *Oral delivery of small RNA and DNA.* Journal of Controlled Release, 2012. **162**(2): p. 438-445.
5. Esteller, M., *Non-coding RNAs in human disease.* Nature Reviews Genetics, 2011. **12**(12): p. 861-874.
6. Finnegan, E.J. and M.A. Matzke, *The small RNA world.* Journal of Cell Science, 2003. **116**(23): p. 4689-4693.
7. Bumcrot, D., et al., *RNAi therapeutics: a potential new class of pharmaceutical drugs.* Nature Chemical Biology, 2006. **2**(12): p. 711-719.
8. Whitehead, K.A., R. Langer, and D.G. Anderson, *Knocking down barriers: advances in siRNA delivery (vol 8, pg 129, 2009).* Nature Reviews Drug Discovery, 2009. **8**(6): p. 516-516.
9. Yin, H., et al., *Non-viral vectors for gene-based therapy.* Nature Reviews Genetics, 2014. **15**(8): p. 541-555.
10. Kumari, A., V. Kumar, and S.K. Yadav, *Nanocarriers: a tool to overcome biological barriers in siRNA delivery.* Expert Opinion on Biological Therapy, 2011. **11**(10): p. 1327-1339.
11. Williford, J.M., et al., *Recent Advances in Nanoparticle-Mediated siRNA Delivery.* Annual Review of Biomedical Engineering, Vol 16, 2014. **16**: p. 347-370.
12. Aigner, A. and D. Fischer, *Nanoparticle-mediated delivery of small RNA molecules in tumor therapy.* Pharmazie, 2016. **71**(1): p. 27-34.
13. Conde, J. and N. Artzi, *Are RNAi and miRNA therapeutics truly dead?* Trends in Biotechnology, 2015. **33**(3): p. 141-144.
14. Raju, G.S.R., et al., *Multifunctional nanoparticles: recent progress in cancer therapeutics.* Chemical Communications, 2015. **51**(68): p. 13248-13259.
15. Barnaby, S.N., et al., *Therapeutic applications of spherical nucleic acids.* Cancer Treat Res, 2015. **166**: p. 23-50.
16. Giljohann, D.A., et al., *Gold Nanoparticles for Biology and Medicine.* Angewandte Chemie-International Edition, 2010. **49**(19): p. 3280-3294.
17. Huang, X., et al., *Modular Plasmonic Nanocarriers for Efficient and Targeted Delivery of Cancer-Therapeutic siRNA.* Nano Lett, 2014. **14**(4): p. 2046-51.

18. Ding, Y., et al., *Gold Nanoparticles for Nucleic Acid Delivery.* Molecular Therapy, 2014. **22**(6): p. 1075-1083.
19. Huang, X., et al., *Light-activated RNA interference in human embryonic stem cells.* Biomaterials, 2015. **63**: p. 70-79.
20. Yin, F., et al., *A Light-Driven Therapy of Pancreatic Adenocarcinoma Using Gold Nanorods-Based Nanocarriers for Co-Delivery of Doxorubicin and siRNA.* Theranostics, 2015. **5**(8): p. 818-833.
21. Huschka, R., et al., *Light-Induced Release of DNA from Gold Nanoparticles: Nanoshells and Nanorods.* Journal of the American Chemical Society, 2011. **133**(31): p. 12247-12255.
22. Chang, Y.T., et al., *Near-Infrared Light-Responsive Intracellular Drug and siRNA Release Using Au Nanoensembles with Oligonucleotide-Capped Silica Shell.* Advanced Materials, 2012. **24**(25): p. 3309-3314.
23. Yuan, H., A.M. Fales, and T. Vo-Dinh, *TAT Peptide-Functionalized Gold Nanostars: Enhanced Intracellular Delivery and Efficient NIR Photothermal Therapy Using Ultralow Irradiance.* Journal of the American Chemical Society, 2012. **134**(28): p. 11358-11361.
24. Lu, W., et al., *Tumor site-specific silencing of NF-kappaB p65 by targeted hollow gold nanosphere-mediated photothermal transfection.* Cancer Res, 2010. **70**(8): p. 3177-88.
25. Park, H.J., et al., *Nonviral delivery for reprogramming to pluripotency and differentiation.* Archives of Pharmacal Research, 2014. **37**(1): p. 107-119.
26. Ramsey, J.D. and N.H. Flynn, *Cell-penetrating peptides transport therapeutics into cells.* Pharmacology & Therapeutics, 2015. **154**: p. 78-86.
27. Rizzuti, M., et al., *Therapeutic applications of the cell-penetrating HIV-1 Tat peptide.* Drug Discovery Today, 2015. **20**(1): p. 76-85.
28. Lee, J.H., et al., *Spontaneous Internalization of Cell Penetrating Peptide-Modified Nanowires into Primary Neurons.* Nano Letters, 2016. **16**(2): p. 1509-1513.
29. Sosibo, N.M., et al., *Facile Attachment of TAT Peptide on Gold Monolayer Protected Clusters: Synthesis and Characterization.* Nanomaterials, 2015. **5**(3): p. 1211-1222.
30. Minamihata, K., et al., *Photosensitizer and polycationic peptide-labeled streptavidin as a nano-carrier for light-controlled protein transduction.* Journal of Bioscience and Bioengineering, 2015. **120**(6): p. 630-636.
31. Gasparini, G. and S. Matile, *Protein delivery with cell-penetrating poly(disulfide)s.* Chemical Communications, 2015. **51**(96): p. 17160-17162.
32. Wang, Y., et al., *Tumor delivery of antisense oligomer using trastuzumab within a streptavidin nanoparticle.* European Journal of Nuclear Medicine and Molecular Imaging, 2009. **36**(12): p. 1977-1986.
33. Sapsford, K.E., et al., *Functionalizing Nanoparticles with Biological Molecules: Developing Chemistries that Facilitate Nanotechnology.* Chemical Reviews, 2013. **113**(3): p. 1904-2074.

34. Nguyen, T.T., C.L. Sly, and J.C. Conboy, *Comparison of the Energetics of Avidin, Streptavidin, NeutrAvidin, and Anti-Biotin Antibody Binding to Biotinylated Lipid Bilayer Examined by Second-Harmonic Generation.* Analytical Chemistry, 2012. **84**(1): p. 201-208.
35. Demers, L.M., et al., *A fluorescence-based method for determining the surface coverage and hybridization efficiency of thiol-capped oligonucleotides bound to gold thin films and nanoparticles.* Analytical Chemistry, 2000. **72**(22): p. 5535-5541.
36. Sugimoto, N., et al., *Thermodynamic Parameters to Predict Stability of Rna/DNA Hybrid Duplexes.* Biochemistry, 1995. **34**(35): p. 11211-11216.
37. Freier, S.M., et al., *Improved Free-Energy Parameters for Predictions of Rna Duplex Stability.* Proceedings of the National Academy of Sciences of the United States of America, 1986. **83**(24): p. 9373-9377.
38. Lesnik, E.A. and S.M. Freier, *Relative Thermodynamic Stability of DNA, Rna, and DNA-Rna Hybrid Duplexes - Relationship with Base Composition and Structure.* Biochemistry, 1995. **34**(34): p. 10807-10815.
39. Breslauer, K.J., et al., *Predicting DNA Duplex Stability from the Base Sequence.* Proceedings of the National Academy of Sciences of the United States of America, 1986. **83**(11): p. 3746-3750.
40. Gao, Y., L.K. Wolf, and R.M. Georgiadis, *Secondary structure effects on DNA hybridization kinetics: a solution versus surface comparison.* Nucleic Acids Research, 2006. **34**(11): p. 3370-3377.